

Machine-Type Communications over the Internet of Things: Energy Efficiency, Connectivity, and Reliability

by
Xiao Lu

A thesis submitted in partial fulfillment of the requirements for the degree of
Doctor of Philosophy
in
Communications

Department of Electrical and Computer Engineering
University of Alberta

© Xiao Lu, 2020

Abstract

Over the years, the Internet-of-things (IoT) have evolved towards the vision that everyday physical objects are endowed with network connectivities, facilitating the interactions between the physical world and the cyber world. One of the enabling techniques of IoT to provide ubiquitous connectivities is machine-type communications (MTC), which has been identified as one of few top use cases for the fifth-generation (5G) network development. It is expected that developing quality-of-service (QoS) for MTC would portray an essential role in future-generation communications. To accommodate ever-increasing IoT applications, MTC networks are required to carry low-power communications among a massive number of ubiquitously-deployed and energy-constrained electronics over heavily-used frequency resource. This poses severe challenges in energy provisioning for sustainable operation, connectivity over long transmission range, and reliability for massive access.

This dissertation aims to make contributions towards addressing the mentioned challenges. First, to solve the energy bottleneck of IoT devices, we propose a self-sustainable communication paradigm and design operational protocols to adapt to the network environment. The performance of the proposed paradigm in large-scale system has been analytical studied. Second, to improve the connectivity of IoT networks, we introduce an energy-efficient cooperative relaying scheme and design different operational protocols based on the availability of channel state information. We

also characterize the performance of the cooperative relaying in tractable expressions which directly reveal the effects of different parameters. Third, we investigate the performance of various 3rd Generation Partnership Project (3GPP)-approved reliability schemes for uplink IoT. Specifically, under these reliability schemes, the uplink coverage probability has been characterized in large-scale IoT networks with massive access. The analytical results reveal the scaling properties of some parameters and demonstrate the effect of the temporally-correlated/independent interference. Finally, we also shed light on promising future research directions.

Acknowledgement

This thesis has been carried out at the University of Alberta, Edmonton, in the Department of Electrical and Computer Engineering under the supervision of Dr. Hai Jiang. I would like to first express my most sincere appreciation to Dr. Hai Jiang, who has the attitude and the substance of a genius, for his continuous support and encouragement to research and scholarship. His generosity helped make my time at Edmonton enjoyable.

I am also very grateful to Dr. Chintla Tellambura and Dr. Majid Khabbazian for serving as the committee members of my thesis. Their valuable comments have considerably improved the quality of my thesis.

My appreciation also extends to my research advisors and colleague including Dr. Dusit Niyato, Dr. Ping Wang, Dr. Ekram Hossan, Dr. Dong In Kim, Dr. Martin Haenggi, Dr. Vincent H. Poor, Dr. Guangxia Li, Dr. Baiquan Li, and Mr Salehi Mohammad and many others for the fruitful discussions and support.

Contents

1	Introduction	1
1.1	Internet-of-Things and Machine-Type Communications	1
1.1.1	Internet-of-Things	1
1.1.2	Machine-Type Communications	4
1.2	Challenges and Research Motivations	7
1.3	Contributions and Organizations	10
1.4	Notations	13
2	Fundamentals	15
2.1	Spatial Point Processes	15
2.2	Wireless-Powered Communications	19
2.2.1	Basic Principles	19
2.2.2	Advantages and Limitations	21
2.3	Ambient Backscatter Communications	22
2.3.1	Basic Principles	22
2.3.2	Advantages and Limitations	23
2.4	Hybrid-Automatic Repeat Request	24

3	Wireless-Powered D2D Communications with Ambient Backscattering	26
3.1	Related Work	26
3.2	Network Model and Stochastic Geometry Characterization	28
3.2.1	Network Model	28
3.2.2	Geometric Modeling of the Systems	36
3.2.3	Performance Metrics	37
3.3	Analytical Results	38
3.3.1	Energy Outage Probability	38
3.3.2	Coverage Probability	41
3.3.3	Throughput	42
3.4	Performance Evaluation and Analysis	44
3.5	Conclusion and Future Work	57
3.6	Appendix	58
3.6.1	Proof of Theorem 3.3.1	58
3.6.2	Proof of Theorem 3.3.2	61
3.6.3	Proof of Corollary 3	62
3.6.4	Proof of Theorem 3.3.3	63
3.6.5	Proof of Theorem 3.3.5	64
4	Ambient Backscatter-Assisted Wireless-Powered Relaying	66
4.1	Related Works	66
4.2	System Model and Stochastic Geometry Characterization	67
4.2.1	System and Relaying Protocol	68
4.2.2	Channel Model	72

4.2.3	Operation Model Selection Protocols	75
4.2.4	Geometric Modeling of the System	79
4.2.5	Preliminaries	79
4.3	Operational Model Selection Protocols	80
4.4	Analysis of Success Probability	82
4.4.1	General-Case Result for ESAP	83
4.4.2	Special-Case Results	85
4.4.3	General-Case Results for ETCP	90
4.5	Analysis of Ergodic Capacity	91
4.5.1	General-Case Results for ESAP	92
4.5.2	Special-Case results	93
4.5.3	General-Case Results for ETCP	94
4.6	Numerical Results	95
4.6.1	SINR Threshold on Success Probability	96
4.6.2	Impact of System Environment (i.e., repulsion factors $\tilde{\alpha}$ and α and densities $\tilde{\zeta}$ and ζ of Ψ and Φ) on Success Probability . . .	99
4.6.3	Impact of Normalized Capacitor Capacity ρ_C on Success Prob- ability	100
4.6.4	Effect of Energy Harvesting Time Fraction ω on Success Prob- ability and Ergodic Capacity	102
4.6.5	Impact of Transmit Power P_S on Energy Efficiency	104
4.6.6	Applications of Analytical Framework	105
4.6.7	Numerical Solutions of Optimization Problems	106
4.7	Conclusion	109
4.8	Appendix	109

4.8.1	Proof of Theorem 1	109
4.8.2	Proof of Corollary 2	112
4.8.3	Proof of Theorem 2	114
4.8.4	Proof of Theorem 3	115
5	On Coverage Probability With Type-II HARQ in Large-Scale Uplink IoT Networks	117
5.1	Related Works	117
5.2	System Model and Assumptions	118
5.3	Analysis of Uplink Coverage Probability	121
5.4	Numerical Results	125
5.4.1	Impact of power control parameters ϵ , \hat{P} and \bar{P}	125
5.4.2	SIR gain of MRC	128
5.4.3	Extensions	130
5.5	Conclusion	132
5.6	Appendix	132
5.6.1	Proof of Theorem 5.3.1	132
6	Conclusions and Future Research	135
6.1	Conclusion	135
6.2	Future Direction	137
6.2.1	Hybrid M2M communications	137
6.2.2	Hybrid relaying systems	138
6.2.3	Cellular IoT networks with retransmissions	139
	Bibliography	141

List of Tables

3.1	NOTATIONs.	35
3.2	Parameter Setting.	44
4.1	NOTATIONs.	76
4.2	Parameter Setting.	96
5.1	NOTATIONs.	121

List of Figures

1.1	Topology of MTC communications over cellular networks.	6
2.1	Paradigms for backscatter communications.	23
3.1	The structure of the hybrid transmitter and hybrid receiver.	29
3.2	Illustration of the hybrid M2M communication.	30
3.3	\mathcal{O}_{PTP} as a function of ζ_A	46
3.4	\mathcal{O}_{STP} as a function of ζ_A	46
3.5	Comparison of energy outage probabilities. ($\alpha = -1$)	47
3.6	\mathcal{C}_{PTP} as a function of ζ_A	49
3.7	\mathcal{C}_{STP} as a function of ζ_A	49
3.8	Comparison of coverage probabilities as a function of ζ_A . ((a) $\xi = 0.2$, (b) $\xi = 0.8$)	50
3.9	Coverage probability as a function of backscattering efficiency.	53
3.10	Coverage probability as a function of RF-to-DC conversion efficiency.	53
3.11	Comparison of coverage probabilities as a function of d . ((a) $\zeta_A =$ 0.02 , $\xi = 0.1$, (b) $\zeta_A = 0.04$, $\xi = 0.6$)	54
3.12	Comparison of average throughput as a function of ζ_A . ((a) $d = 5$, $\xi = 0.2$, (b) $d = 5$, $\xi = 0.8$)	55

3.13	Comparison of average throughput as a function of d . ((a) $\xi = 0.2$, $\zeta_A = 0.02$, (b) $\xi = 0.8$, $\zeta_A = 0.01$)	56
4.1	A dual-hop relaying system in an α -GPP field of ambient emitters and interferers.	68
4.2	A time-slot based relaying protocol.	72
4.3	Success probability as a function of τ_W	97
4.4	Success probability as a function of α	98
4.5	Success probability as a function of ζ . ($\tilde{\zeta} = 2000/\text{km}^2$)	98
4.6	Success probability as a function of $\tilde{\zeta}$	101
4.7	Success probability as a function of ρ_C	101
4.8	Success probability as a function of the energy harvesting time fraction ω	103
4.9	Ergodic capacity as a function of the energy harvesting time fraction ω	103
4.10	Energy efficiency as a function of P_S ($\tau_W = 10\tau_W$).	104
4.11	Minimum transmit power and optimal energy harvesting time fraction with reliability constraints. ($\rho_Q = 2000/\text{km}^2$, $\bar{P} = 30$ dBm)	107
4.12	Maximum energy efficiency and optimal energy harvesting time frac- tion and with reliability constraints. ($\rho_Q = 2000/\text{km}^2$, $\bar{P} = 30$ dBm) .	108
5.1	Coverage probability with different values of ϵ ($\hat{P} = \infty$).	126
5.2	Coverage probability with different values of \hat{P} (for $\bar{P} = \hat{P} = P$). . .	128
5.3	Coverage probability with different values of \bar{P} (for $\epsilon = 0.5$).	128
5.4	SIR gain of MRC with different values of ϵ (for $\tau = 0$ dB, $\hat{P} = \infty$). .	129

5.5	SIR gain of MRC with different base station density ($\epsilon = 1, \hat{P} = \bar{P} = 0$ dBm).	130
5.6	Coverage probability with different N ($\tau = 0$ dB).	131
5.7	Coverage probability with different number of antennas ($\tau = 0$ dB).	131

List of Abbreviations

Acronyms	Definition
AWGN	additive white Gaussian noise
ABR	ambient backscatter relaying
BS	base station
CDF	cumulative distribution function
CSI	channel state information
D2D	device-to-device
ESAP	energy and SINR-aware Protocol
ETCP	explore-then-commit protocol
FCIPC	full channel inversion power control
FPC	fractional power control
FVI	fast-varying interference
GFPC	generalized fractional power control
GPP	Ginibre point process
HARQ	hybrid automatic repeat request
HTT	harvest-then-transmit
H2H	human-to-human
IoT	Internet-of-things
MRC	maximal-ratio combining
MTC	machine-type communications

M2M	machine-to-machine
NOMA	non-orthogonal multiple access
NPC	no power control
PCE	path-loss control exponent
PDF	probability density function
PPP	Poisson point process
QoS	quality-of-service
QSI	quasi-static interference
RF	radio frequency
SINR	signal-to-interference-plus-noise ratio
SIR	signal-to-interference ratio
SNR	signal-to-noise ratio
TFPC	truncated fractional power control
UE	user equipment
URLLC	ultra-reliable low-latency communications
WPR	wireless-powered relaying
WSN	wireless sensor networks
3GPP	3rd Generation Partnership Project

Chapter 1

Introduction

1.1 Internet-of-Things and Machine-Type Communications

1.1.1 Internet-of-Things

One of the ultimate goals of information and communications technology (ICT) is to evolve towards the concept of “anytime, anywhere, anyone, connected to anything,” [1]. The Internet-of-things (IoT), under development and still in nascent stages, is making this vision possible, by establishing connections between the real world and the virtual Internet. Physically, IoT merges our environment (e.g., homes, vehicles, workplaces) through smart gadgets, such as RFID, sensors, actuators, mobiles phones, and wearables, to extract useful information from the collected data for responsiveness, adaptiveness, automation, and intelligence [2]. Furthermore, the giant IoT infrastructure is envisioned to be the main hub between various technologies, e.g., edge computing [3,4], virtual reality [5], blockchains [6]. This allows the physical objects of pervasive presence to extend all the internet services to accommodate our ever-increasing demand.

The IoT revolution is shaping our ways of living, working and even thinking with its vast amount of applications surrounding us in many fields such as [7–10]

- Home applications which people use for their daily lives. Network-interfaced electric toothbrushes, exercise facilities, washing machines, temperature and moisture control systems are some of the examples. Google Nest and Apple HomeKit are commercial platforms already available to host IoT-based home applications.
- Transportation applications which regulate, monitor, and secure the traffic. Different types of sensors, aggregators, coordinators, and classifiers are involved to collect instant information and make the right decisions to facilitate efficient and reliable transportation systems. Some examples include: parking management, electronic tolling, unmanned driving and navigation, accident avoidance, and speed enforcement.
- Healthcare applications which identify (e.g., through anomaly discovery and behavioral pattern recognition), inform, and prevent people from health issues. Body sensors and wearables, such as Apple Watch, are typical applications for health monitoring, e.g., heart rate, blood pressure, and depressive disorder.
- Industry applications for product manufacturing and management. Such examples include merchandise tracking, quality inspection, warehouse management, and automatic vending.

IoT applications commonly feature with a four-phase of life cycle as follows: First, *data collection phase*, where IoT devices collect target information by monitoring the physical environment; Second, *communication phase*, where the collected data are

sent through the Internet infrastructure to the desired destinations, such as data processors and servers; Third, *data analysis phase*, where the aggregated data is analyzed to extract useful information; Four, *decision-making phase*, where the extracted information is used to make intelligent decisions based on some optimization processes. Thus, IoT is an evolved system based on the Internet. Compared to the Internet, a distinguishing feature of IoT is autonomous decision making based on artificial intelligence enabled by self-recognizable smart things.

The IoT is a complex system the characteristics of which vary from one application to another. Some of the general and fundamental characteristics of the IoT are identified follows [11, 12].

- *Intelligence*: Enabled by a combination of algorithms and computation, the IoT is intelligent in the sense that it facilitates a massive number of smart things to respond properly to serve decision making purposes.
- *Connectivity*: Connectivity empowers the interaction between every part of the real world with the virtual Internet.
- *Sensing*: Sensing technologies serve as the means to create awareness of the physical environment to the cyber world.
- *Heterogeneity*: The IoT applications are heterogeneous as they are based on different software and hardware platforms and have interactions with other platforms through different interfaces.
- *Enormousness*: The number of end devices to be connected with each other are expected to be much greater than the end devices connected to the existing Internet.

1.1.2 Machine-Type Communications

IoT networks need to be engineered to carry a massive volume of data generated by the growing IoT applications. Over the past decade, a new class of machine-type communications (MTC), also referred to as machine-to-machine (M2M) communications, have emerged to accommodate the IoT traffic with diverse quality-of-service (QoS) requirements.

The key features that differentiate MTC from conventional human-to-human (H2H) communications are listed as follows [13, 14].

- MTC lacks human intervention in the communication process.
- MTC mainly occurs in the uplink as a majority of IoT applications require upload of collected data to the servers.
- MTC traffic involves varying loads and varying QoS requirements (e.g., delay and throughput).
- MTC traffic are usually bursty due to its event-driven nature.

MTC has been identified as one of few top use cases for the fifth-generation (5G) network development [15]. In Release 12 [16], the 3rd Generation Partnership Project (3GPP) standardization defined the low-cost MTC operation as category 0 (or CAT-0). In particular, CAT-0 specifies a transmission rate of up to 1 Mbps for M2M communications. CAT-0 devices should enjoy a simplified hardware complexity by at least 50% compared to CAT-1 which is defined for LTE cellular devices. To realize this objective CAT-0 indicates the application of only one antenna at an M2M receiver with a maximum bandwidth of 20 MHz. Besides, M2M devices should support Frequency-Division Duplexing (FDD) half-duplex operation

to eliminates the need for advanced duplex filters. Later on, in Release 13 [17], the 3GPP incorporated two special categories, namely, CAT-M and CAT-N, for MTC and Narrowband-IoT, respectively, to LTE specifications which includes fully-defined MTC and IOT features. Specifically, CAT-M aims to launch commercial solutions of low-power wide-area IoT. CAT-M requires a further reduced hardware complexity of M2M devices which should be below 25% of that of the CAT-1 devices. Moreover, the maximum channel bandwidth allocated to a CAT-M device should be limited to 1.4 MHz. To enable M2M communication through thick walls, the CAT-M target is to reach 15 dB of coverage gain for M2M devices with the power class of 23 dBm. On the other hand, the goal of CAT-N is to promote battery longevity, reduced complexity and improved coverage. The link budget of NB-IoT is up to 20 dBm with a maximum bandwidth of 0.2 MHz. Moreover, peak rates of 0.144 Mbps and 0.2 Mbps are specified for the uplink and downlink, respectively.

Furthermore, the merging between MTC and cellular networks are predicted as the off-the-shelf cellular infrastructure of wide geographical coverage serve as a natural choice to handle a majority of MTC traffic. MTC subscriptions are already available at cellular service providers. For example, KORE Telematics provides services over cellular connections for billing, remote support, logistics, and relationship management [18]. Moreover, standardizations by 3rd Generation Partnership Project (3GPP) to promote the MTC and cellular integration are currently under progress [19, 20].

Fig. 1.1 shows the typology of MTC envisioned by 3GPP [21], which consists of three main parts, i.e., MTC networks, cellular networks, and the core network. In MTC networks, the majority of MTC occurs among M2M devices and between M2M devices and MTC gateways. The former is enabled by the local inter-device commu-

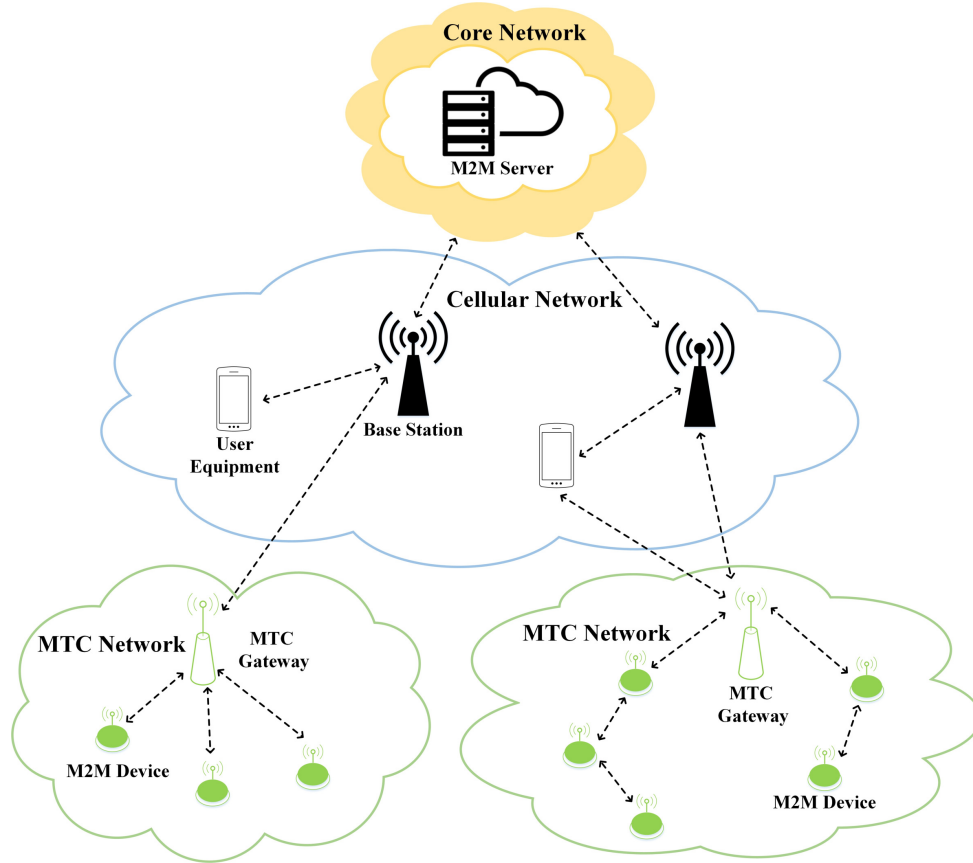


Figure 1.1: Topology of MTC communications over cellular networks.

nication so that the information does not need to be interchanged by the gateways. The latter targets for remote information interchange with M2M servers. Both types of communications can be realized through direct transmission or multihop transmission. In cellular networks, legacy H2H communication between user equipment (UE) coexists with MTC between MTC gateways and cellular base stations (BSs). It is also possible to establish device-to-device (D2D) connections between UEs and MTC gateways [22]. This not only enables the interactions between UEs and M2M devices but also allows UEs to assist MTC, e.g., through cooperative relaying.

1.2 Challenges and Research Motivations

The diversity of emerging MTC applications presents assorted challenges in developing MTC. Inspecting the common use cases and features of MTC, we can identify that MTC has challenges in the following aspects.

- Energy-related challenges in supporting a long life cycle of MTC devices. Replenishing batteries is costly and inconvenient for remote areas and even impossible for toxic environments. The exponentially growing number of IoT devices is aggravating this problem.
- Connectivity-related challenges in supporting long transmission range. In last-mile IoT networks, MTC devices may need to communicate with a gateway far away. It is a challenging task to achieve long transmission range with energy-constrained MTC devices and heavily-used frequency resources to accommodate enormous transmission demand.
- Reliability-related challenges in supporting massive access, message timeliness and high throughput for data-intensive applications. Ultra-reliable low-latency communications (URLLC) is one of the three classes of use cases in 5G. Meeting MTC with URLLC has not been addressed by the latest 3GPP Release 15 and is the main focus of the ongoing 3GPP Release 16.

To solve the energy scarcity and sustain the operation of massive IoT devices, radio frequency (RF) energy harvesting, which converts the received RF signals into electricity, emerges as a solution. The broadcast characteristic and pervasiveness of RF signals nowadays (e.g., from TV towers [23] or Wi-Fi access points [24]) make this solution a nature and practical choice for wireless IoT devices. The advance of

RF energy harvesting technology gives birth to two emerging self-sustainable communication technologies, namely, wireless-powered communications [25] and ambient backscatter communications [26]. Wireless-powered communication utilizes the harvested energy to generate RF signals for information transmission. While ambient backscattering utilizes the harvested energy to passively reflect the existing RF signals in the air.

Though wireless-powered communication and ambient backscatter communications somehow mitigate the energy scarcity, both of them face their own challenges. Specifically, a wireless-powered device involves power-consuming active transmission. Consequently, the device may need to spend a long time to harvest and accumulate energy for the circuit operation. To address such challenges, some existing literature mainly focuses on designing network protocols for wireless-powered devices [27–31] to utilize network resources more efficiently. For example, the authors in [29] introduce a harvest-then-transmit protocol for the relay to optimize the time allocation for energy harvesting in the downlink and information transmission in the uplink to maximize throughput. These network protocols manage to enhance the performance of wireless-powered devices under different system configurations. However, the performance is still limited by the high circuit power consumption because of the active transmission nature. On the other hand, ambient backscatter communication suffers from low bit rate because an ambient backscatter transmitter adopts simple modulation schemes with small constellations, such as amplitude shift keying and binary phase shift keying. As an ambient backscatter transmitter just passively reflects the incident signals, it has a low degree of freedom for transmit power control. Moreover, due to the dual-hop path loss of ambient carrier signals [32], ambient backscattering is only feasible for short-range communication. Existing approaches to optimize am-

bient backscatter communications mainly focus on tuning the reflection coefficient of the backscatter transmitter to adapt to varying network environments [33–36]. However, the performance of ambient backscatter communications still suffers from the dual-hop path loss and low transmission rate due to the hardware limitation. The above-mentioned challenges largely limit the applications of wireless-powered communications and ambient backscatter communications in practice. This motivates us to design new solutions to enhance the applicability of these self-sustainable communications paradigms.

To improve connectivity, cooperative relaying has served as an effective approach especially for extending the transmission range. The key benefit of cooperative relaying is to achieve enhanced signals strength without increasing the transmit power [37]. This concept is particularly attractive for MTC, due to the resource limitation of the MTC devices. Moreover, as MTC devices are usually deployed in large size and with high density, multiple relaying devices and paths might be available to increase the connectivity. In this regard, cooperative relaying with RF energy harvesting has attracted a great deal of recent research attention. Both (active) wireless-powered relaying and (passive) ambient backscatter relaying have been proposed and studied in the recent literature [28, 38–42] and shown to provide more robust connectivity as well as improved energy efficiency and spatial efficiency. However, wireless-powered relaying and ambient backscatter relaying faces the same challenges imposed by wireless-powered communication and ambient backscatter communications which have been discussed above. This motivates us to design energy-efficient solutions to improve end-to-end connectivity with extended transmission range.

Toward reliability of MTC, the 3GPP consortium has worked out a series of solutions. For example, Fractional Power Control (FPC) which partially compensates

for the uplink path loss is included as an essential scheme for uplink transmission to mitigate interference [43]. Essentially, FPC manages to save the transmit power of center users and avoids the edge users to cause excessive interference [44]. A recent study [45] reports that FPC provides significant performance gains, especially for the edge users compared to the scheme that each user adopts its maximum transmit power. Another promising technique that plays an important role in robust uplink communication is the hybrid Automatic Repeat Request (HARQ). Type-I HARQ and Type-II HARQ with chase combining (HARQ-CC) [46] are two most widely adopted HARQ techniques due to their practicability. The former decodes the received signal of each transmission independently while the latter combines the received signals of different transmissions with maximum-ratio combining (MRC) for decoding. As MTC is uplink intensive, we are motivated to study the uplink performance of practical IoT scenarios with 3GPP-approved solutions and characterize the performance in tractable expressions.

1.3 Contributions and Organizations

To fill the research gaps reviewed above, we propose solutions and investigate the performance of different schemes for energy efficiency or reliability of MTC in large-scale IoT networks. The main contributions of this dissertation are summarized as follows.

- **New hybrid M2M communications paradigm and its performance analysis.** Chapter 3 investigates the performance of a hybrid M2M communication paradigm with ambient backscattering and wireless-powered communication functions. Since the radio signals for energy harvesting and for

backscattering only come from the ambient, the performance of the hybrid M2M communications depends largely on the environment factors, e.g., distribution, spatial density, and transmission load of ambient energy sources. Two mode selection protocols have been designed for the hybrid transmitter, allowing a more flexible adaptation to the environment. Then, analytical models have been developed to characterize the impacts of the environment factors on the hybrid M2M communication performance. Together with extensive simulations, the analysis shows that the communication performance benefits from larger repulsion, transmission load and density of ambient energy sources. Furthermore, how different mode selection mechanisms affect the communication performance has been investigated.

- **Design of operational protocols and performance analysis for a novel self-sustainable relaying scheme.** Chapter 4 proposes a novel hybrid relaying strategy by combining wireless-powered communication and ambient backscattering functions to improve the applicability and performance of data transfer. In particular, the hybrid relay can harvest energy from radio frequency (RF) signals and use the energy for active transmission. Alternatively, the hybrid relay can choose to perform ambient backscattering of incident RF signals for passive transmission. For the operation of the hybrid relaying, selecting a proper mode based on the network environment is the key to better relaying performance. Two mode selection protocols have been devised to coordinate between the active and passive relaying in the cases with and without instantaneous channel state information (CSI) of active transmission, respectively. In the former case, since the hybrid relay is aware of whether the two

relaying modes are applicable for the current time slot based on the CSI, it selects active relaying if applicable due to higher capacity and selects passive relaying otherwise. In the latter case, the hybrid relay first explores the two relaying modes and commits to the mode that achieves more successful transmissions during the exploration period. With different mode selection protocols, the success probability and ergodic capacity of a dual-hop hybrid relaying system have been characterized considering the field of randomly located ambient transmitters. The analytical and the numerical results demonstrate the effectiveness of the mode selection protocols in adapting the hybrid relaying into the network environment and reveal the impacts of system parameters on the performance of the hybrid relaying. As applications of the analytical framework which is computationally tractable, optimization problems based on the derived expressions have been formulated to optimize the system parameters with different objectives. The optimal solutions exhibit a tradeoff between the maximum energy efficiency and target success probability.

- **Coverage probability analysis of IoT networks with massive uplink access under Hybrid automatic repeat request (HARQ).** Chapter 5 analyzes the effects of power control on the transmission SIR loss and the signal-to-interference ratio (SIR) gain of MRC under HARQ in large-scale IoT networks with massive uplink access. In the context of temporally-correlated quasi-static interference (QSI) and temporally-independent fast-varying interference (FVI), the uplink coverage probabilities of the large-scale IoT networks have been characterized under various power control schemes. The developed analytical framework reveals some scaling properties and provides insights into

the effects of network parameters (e.g., power control parameters) on the uplink coverage performance. It is demonstrated that the SIR gain of MRC is more remarkable in the scenario with QSI compared to that with FVI. Moreover, the SIR gain of MRC increases with path-loss compensation exponent.

The fundamentals of the investigated topics and the applied analytical frameworks are described in Chapter 2. The technical contributions of this dissertation are presented in Chapter 3 through 5. Chapter 3 proposes a novel hybrid communication paradigm for M2M communications and characterizes its performance in terms of energy outage probability, coverage probability and throughput under different mode selection mechanisms. Chapter 4 extends the hybrid communication to cooperative relaying for energy-efficient transmission with extended range. Chapter 5 investigates performance analysis of large-scale IoT networks with massive uplink access under HARQ. Each technical chapter has the related works presented at the beginning and adopts different notations for the symbols. Finally, Chapter 6 concludes this dissertation with the summations of the main contributions and discusses the promising future directions for each individual technical chapters.

1.4 Notations

In this dissertation, we use $\mathbb{E}[\cdot]$ to denote the average over all random variables in $[\cdot]$, $\mathbb{E}_X[\cdot]$ to denote the expectation over the random variable X , and $\mathbb{P}(E)$ to denote the probability that an event E occurs. Besides, $\|\mathbf{x}\|$ is used to represent the Euclidean norm between the coordinate \mathbf{x} and the origin of the Euclidean space. \bar{z} and $|z|$ denote the complex conjugate and modulus of the complex number z , respectively. i is the imaginary unit, i.e., $i = \sqrt{-1}$. The notations $f_X(\cdot)$, $F_X(\cdot)$, $M_X(\cdot)$

and $\mathcal{L}_X(\cdot)$ are used to denote, respectively, the probability density function (PDF), cumulative distribution function (CDF), moment generating function (MGF), and Laplace transform of a random variable X . $\operatorname{erfc}(\cdot)$ is the complementary error function defined as $\operatorname{erfc}(x) = \frac{2}{\sqrt{\pi}} \int_x^\infty \exp(-t^2) dt$. Besides, let $\binom{n}{i} = \frac{n(n-1)\cdots(n-i+1)}{i(i-1)\cdots 1}$ denote the binomial coefficient and $[a, b]^+ \triangleq \max(a, b)$. Let $\mathcal{G}(x, y)$ represent the gamma distribution with shape parameter x and scale parameter y , and $\mathcal{E}(x)$ represent the exponential distribution with rate parameter x .

Chapter 2

Fundamentals

This section introduces the fundamentals of the concepts and properties of the mathematical tools applied in the analysis of the thesis.

2.1 Spatial Point Processes

Stochastic geometry serves as a powerful statistical framework for the analysis of large-scale wireless networks with different sources of uncertainties, such as spatial randomness, power control, fading, and shadowing. Over recent years, stochastic geometry models have been extensively developed for interference and signal-to-interference-plus-noise (SINR) characterizations in different types of large-scale networks such as cellular networks, ad hoc networks, and cognitive radio networks [49, 50]. Existing literature has demonstrated the tractability and yet high accuracy in the performance characterizations and bounds derived from stochastic geometry analysis. These the analytical characterizations reveal the effects of network parameters and provide design insights on the network deployment and operation, which

are usually not easy to be obtained from computationally intensive simulations.

Stochastic geometry is widely adopted for large-scale analysis as it provides the analytical framework that characterizes the average behaviour of the entire system over all the possible realizations instead of a specific device at a certain geographical location. To model the randomness of system typologies, stochastic geometry abstract the considered system to a certain stochastic point process [51]. In other words, based on the network type and properties (e.g., MAC protocols), a matching point process is adopted to model the spatial locations of the system devices. Then, based on the probability distribution of the matching point process, stochastic geometry analysis measures the system performance by taking the spatial average.

In the following, we define the stochastic point processes used for the performance modeling in this thesis.

Definition 1 (*Poisson point process*): *A point process $\Phi = \{x_j\}_{j \in \mathbb{N}} \subset \mathbb{R}^d$ is a Poisson point process PPP if and only if the number of points inside any compact set $\mathcal{B} \subset \mathbb{R}^d$ is a Poisson random variable, and the numbers of points in disjoint sets are independent.*

The probability generating functional for the PPP is given by

$$\mathbb{E} \left[\prod_{x \in \Phi} v(x) \right] = \exp \left(- \lambda \int_{\mathbb{R}^d} (1 - v(x)) dx \right). \quad (2.1)$$

Because of the independence property, the PPP offers a simple and tractable modeling framework which may lead to simple and even closed-form expressions in some special cases. Despite its analytical tractability, the PPP fails to model the correlation among the locations of the system entities. The weakness of PPP modeling is that the spatial points may locate too close to each other due to their

independence [52]. Nevertheless, in real-world systems, the RF transmitters, such as cellular base stations and access points, are deployed with reference to the locations of each other [53, 54]. In other words, the distribution of network components may exhibit repulsion behaviors, which is a common phenomenon in wireless systems, e.g., sensor networks [55]. An instance in real network design is that RF transmitters, such as access points, relay nodes, and data sinks, are not deployed too close to each other, which is an obvious evidence of repulsive behavior. This calls for the need of more sophisticated and general geometric approaches to model the correlation phenomena in the real-world systems.

To cope with this issue, the α -Ginibre point process (GPP) [56] has been developed. α -GPP is a repulsive point process which allows to characterize the repulsion among randomly located points and covers the PPP as a special case (i.e., when $\alpha \rightarrow 0$). The coefficient α ($\alpha = -1/\kappa$ for a positive integer κ) indicates the repulsion degree of the spatial points. Specifically, the repulsion is the strongest in case $\alpha = -1$ and disappears when α approaches 0. The α -GPP can be formally defined as follows.

Definition 2 (*α -Ginibre point process*): A α -GPP is a determinantal point processes with the kernel given by

$$K(\mathbf{x}, \mathbf{y}) = \zeta e^{\pi\zeta\mathbf{x}\bar{\mathbf{y}}} e^{-\frac{\pi\zeta}{2}(|\mathbf{x}|^2+|\mathbf{y}|^2)}, \quad \mathbf{x}, \mathbf{y} \in O = \mathcal{B}(0, R), \quad (2.2)$$

with respect to the Lebesgue measure on \mathbb{C} .

For any α -GPP Ω , let ζ denote the spatial density of the points of Ω , and \mathcal{K} represent an almost surely finite collection of Ω located inside an observation window $\mathbb{O}_{\mathbf{x}}$, denoted as a circular Euclidean plane with positive radius R . Without loss of

generality, in this paper, we restrict the analysis on a generic point located at \mathbf{x} within $\mathbb{O}_{\mathbf{x}}$. We begin with the Laplace transform of α -GPP characterized by means of Fredholm determinants [57]. The Fredholm determinant is generally expressed in the form of a complex-valued function, which contains the coordinates of the spatial points represented by complex numbers as the variables. For $|\alpha| \leq 1$, the Fredholm determinant of an arbitrary function F is expressed as $\text{Det}(\text{Id} + \alpha F)$. More properties of the Fredholm determinant can be found in [57].

Proposition 1 [56, Theorem 2.3] *Let φ represent an arbitrary real-valued function. For an α -GPP, the Laplace transform of $\sum_{k \in \mathcal{K}} \varphi(\mathbf{x}_k)$ can be expressed as*

$$\mathbb{E} \left[\exp \left(-s \sum_{k \in \mathcal{K}} \varphi(\mathbf{x}_k) \right) \right] = \text{Det}(\text{Id} + \alpha \mathbb{K}_{\varphi}(s))^{-\frac{1}{\alpha}}, \quad (2.3)$$

where $\mathbb{K}_{\varphi}(s)$ is given by

$$\mathbb{K}_{\varphi}(s) = \sqrt{1 - \exp(-s\varphi(\mathbf{x}))} G_{\Omega}(\mathbf{x}, \mathbf{y}) \sqrt{1 - \exp(-s\varphi(\mathbf{y}))}, \quad \mathbf{x}, \mathbf{y} \in \mathcal{K}, \quad (2.4)$$

wherein G_{Ω} is the Ginibre kernel which represents the correlation force among different spatial points in Ω defined as

$$G_{\Omega}(\mathbf{x}, \mathbf{y}) = \zeta e^{\pi\zeta\mathbf{x}\bar{\mathbf{y}}} e^{-\frac{\pi\zeta}{2}(|\mathbf{x}|^2 + |\mathbf{y}|^2)}, \quad \mathbf{x}, \mathbf{y} \in \mathcal{K}. \quad (2.5)$$

As the Laplace transform in (2.3) is given in the form of Fredholm determinant, the evaluation of it may involve high computation complexity. For example, the conventional approach in [58] approximates the Fredholm determinant by the determinant of an $N \times N$ matrix, resulting in a complexity of $O(N^3)$. The recent results

in [59] allow a more efficient computation of the Fredholm determinant with significantly reduced complexity. A simplified expression for evaluating the Fredholm determinant is presented in the following Proposition.

Proposition 2 [59, Lemma 3] *With $\mathbb{K}_\varphi(s)$ defined in (2.4) and $G_\Omega(\mathbf{x}, \mathbf{y})$ defined in (2.5), the Fredholm determinant on the right-hand side of (2.3) can be evaluated as*

$$\begin{aligned} & \text{Det}(\text{Id} + \alpha \mathbb{K}_\varphi(s))^{-\frac{1}{\alpha}} \\ &= \prod_{n=0}^{N_{\text{closed}}} \left(1 + \frac{2\alpha(\pi\zeta)^{n+1}}{n!} \int_0^R \exp(-\pi\zeta r^2) r^{2n+1} (1 - \exp(-s\varphi(r))) dr \right)^{-\frac{1}{\alpha}}. \end{aligned} \quad (2.6)$$

The complexity in calculating (2.6) is $O(N_{\text{closed}})$. As N_{closed} goes to infinity, the exponential convergence rate of (2.6) follows from the smoothness of the Ginibre kernel [56].

2.2 Wireless-Powered Communications

2.2.1 Basic Principles

Wireless powered communication is a sustainable networking paradigm with power supply from the radio environment. Specifically, equipped with RF energy harvesting capability, the wireless-powered devices are enabled to harvest energy from RF signals in the air and store the harvested energy for future use. Different from conventional battery-powered devices which are replenished by connecting an external power cord or by changing batteries, a wireless-powered device replenishes its energy storage, e.g., battery or capacitor, only based on RF energy harvesting. Therefore,

the main difference from a battery-powered device is that a wireless-powered device needs to be additionally equipped with an RF energy harvester.

The main components of an RF energy harvester are as follows.

- The impedance matching is a resonator circuit operating at the designed frequency to maximize the power transfer between the antenna and the multiplier. The efficiency of the impedance matching is high at the designed frequency.
- The main component of the voltage multiplier is diodes of the rectifying circuit which converts RF signals (AC signals in nature) into DC voltage.
- The capacitor regulates the DC outage and ensures to deliver power smoothly to the load.

The efficiency of the RF energy harvester depends on the efficiency of the antenna, the accuracy of the impedance matching between the antenna and the voltage multiplier, and the power efficiency of the voltage multiplier that converts the received RF signals to DC voltage. Generally, higher RF energy harvesting efficiency can be achieved with higher incident RF power density [60].

The RF signals can come from either dedicated RF sources or ambient RF sources. The former and the latter refer to the RF transmitters that are intended and unintended for the purpose of RF energy transfer, respectively. Dedicated RF sources (e.g., power beacons) can be deployed to provide energy to wireless-powered devices when a more reliable energy supply is needed. By contrast, the harvested energy from ambient RF sources (e.g., TV towers and WiFi access points) can be dynamic and opportunistic as the ambient RF sources are uncontrollable to the energy harvester.

2.2.2 Advantages and Limitations

Compared to conventional battery-powered devices, wireless-powered devices eliminate the need for battery recharging and replacement, and thus reduce the operational cost. However, wireless-powered devices have to accumulate sufficient energy first before performing other operations, such as signal processing and transmission. This incurs a time delay and makes wireless-powered communication hard to satisfy instant communication demand.

For wireless-powered communication with dedicated RF sources, the transmit power, frequency and time can be fully controlled to provide reliable energy supply for different quality-of-service (QoS) requirements. This is in contrast to renewable energy-powered communications, the renewable sources (e.g., solar and wind) of which are time-varying and uncontrollable. However, deploying dedicated RF sources incur an infrastructure cost. Another disadvantage is that wireless-powered devices are only functional within the energy provisioning zone of the dedicated RF sources.

For wireless-powered communication with ambient RF sources, the RF energy is essentially free and pervasive, which exempts the deployment and operational cost for dedicated RF sources. Moreover, without the restriction of energy provisioning from dedicated RF sources, wireless-powered devices have better mobility. However, the performance of wireless-powered devices is subject to the strength of ambient RF energy. Usually, the communication links can only be established on a best-effort basis.

2.3 Ambient Backscatter Communications

2.3.1 Basic Principles

Different from other conventional wireless communications, backscatter communication does not involve active generation of RF signals for transmission. Instead, the backscatter transmitter modulates a sequence of digital symbols onto the RF backscattered waveforms at the antenna. The waveform adaptation is made by adjusting the load impedance, i.e., reflection coefficient, of the antenna to generate different waveforms from that of the original signal. This is known as load modulation. Figure 2.1 shows the diagram of a backscatter transmitter with binary load modulation. It has two loads with the impedances intentionally matching and mismatching with the antenna impedance, respectively. The antenna reflection coefficient, and thus the amount of the reflected signal from the antenna, can be tuned by switching between the two impedance loads. Specifically, when the load with the matched impedance is chosen, most of the incident signal is harvested, i.e., an absorbing state. Conversely, if the antenna switches to the other load, a large amount of the signal is reflected, i.e., a reflecting state. A backscatter transmitter can utilize an absorbing state and a reflecting state to indicate a bit “0” and a bit “1”, respectively, to its intended receiver. It follows that, in the reflecting state, the receiver will observe a superposition of the original wave from the signal source (e.g., the interrogator) and the backscatter transmitter’s reflected wave. In the absorbing state, the receiver will only see the original wave. The states are then interpreted as information bits. The information rate can be adapted by varying the bit duration.

Figure 2.1 again shows the diagram of binary amplitude demodulation based on envelope detection at the receiver. The circuit has four components: an antenna, an

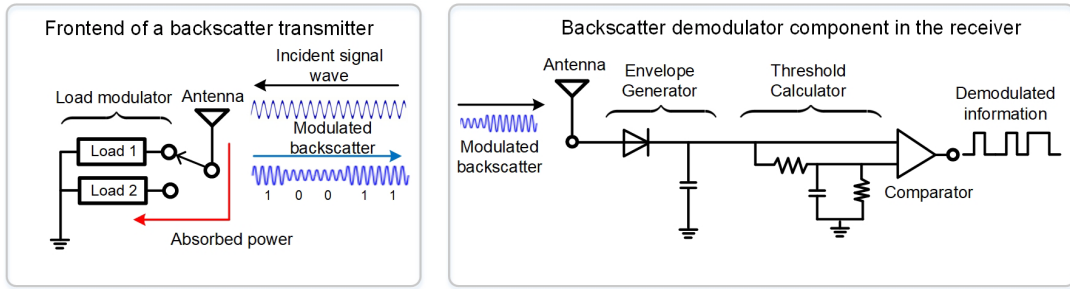


Figure 2.1: Paradigms for backscatter communications.

envelope averager, a threshold calculator, and a comparator. The instantaneously incoming waves at the antenna are smoothed at the envelope averager, which gives an envelope of the instantaneous signals. The threshold calculator generates a threshold value by taking the mean of the long-term averaged envelope. Then, the comparator makes a comparison between the smoothed instantaneous envelope of the received modulated backscatter and the threshold to decide the value of the information bits.

2.3.2 Advantages and Limitations

As the backscatter transmitter only works as a passive transponder that reflects part of the incident signals during modulation, the hardware circuit requires no conventional communication components such as oscillator, amplifier, filter, and mixer. Thus, ambient backscattering features with ultra-low power consumption. For example, the experiment in [61] demonstrates that a batteryless backscatter sensor can function continuously with an input RF power of 18 dBm (equivalently, $0.1103 \mu\text{W}/\text{cm}^2$ power density) for energy harvesting. Typically, the backscatter transmitter only consists of a digital logic integrated circuit, an antenna, and optional power storage, making it cheap, small, and easy to deploy. Another obvious advantage is that, by utilizing existing RF signals in the air, an ambient backscatter system

virtually incurs no cost for deploying and maintaining carrier emitters. Furthermore, without the reliance on the dedicated carrier emitters, multiple ambient backscatter transmitters can initiate transmissions independently and simultaneously, thus making multi-hop communications possible [62].

Despite the above advantages, ambient backscatter communications have the following limitations. As the ambient carrier emitters are not controllable by the backscatter transmitter, it is difficult to guarantee the QoS for ambient backscatter communications. Moreover, as both the harvested energy and reflected signals based on the ambient RF signals are typically small, the effective transmission range and achievable bitrate are very limited compared to the conventional backscatter systems, such as passive sensors [63] and RFID tags [64].

2.4 Hybrid-Automatic Repeat Request

Hybrid automatic repeat request (HARQ) is a retransmission mechanism that combines forward error correction (FEC) at the physical layer with the standard automatic repeat request (ARQ) at the MAC layer [65]. Specifically, The FEC coding is utilized to correct the erroneous message by encoding the message with redundancy, while the ARQ is adopted to recover the uncorrectable errors through retransmission. Due to the hybrid operation, HARQ achieves a better performance than the standard ARQ in poor channel conditions at the expense of lower throughput in good channel conditions.

Type-I HARQ and Type-II HARQ with chase combining (HARQ-CC) [9] are two most widely adopted HARQ techniques due to their practicability.

- Type-I HARQ: Both error detection, e.g., cyclic redundancy check, and FEC

parity bits are added to the data prior to each transmission. If the received data cannot be decoded correctly, a negative acknowledgement from the receiver or timeout is used to indicate a retransmission request. Upon the request, the sender retransmits the same data packets. The receiver abandons the received signals from the previous transmission and attempts to decode from the current transmission.

- Type-II HARQ-CC: The initial transmission contains only data and error detection. If a retransmission occurs upon a retransmission request, the retransmission will additionally contain FEC parity bits. At the receiver side, the received signals from the retransmission(s) and the initial transmission are combined through maximal ratio combining (MRC) to improve signal strength for decoding.

Under good channel conditions where the initial transmission of each data packet succeeds, only Type-I HARQ suffers throughput loss due to the use of FEC. Under bad channel conditions where retransmissions occur, Type-II HARQ-CC outperforms Type-I HARQ due to the use of the diversity combining technique.

Chapter 3

Wireless-Powered D2D

Communications with Ambient

Backscattering

This chapter¹ aims to address the energy-bottleneck of IoT devices. As reviewed in Chapter 2, both wireless-powered communication and ambient backscattering have their own shortcomings which limit their applications in certain cases. We therefore propose new solutions to overcome the limitations.

3.1 Related Work

Recently, wireless-powered communications [60] have attracted much attention and have been applied in D2D communications to improve energy efficiency. In [66], the authors investigate a cognitive D2D transmitter that harvests energy from cellular

¹A version of this chapter has been published in the IEEE Transactions on Wireless Communications [112] and also in part in the Proceedings of IEEE Vehicular Technology Conference [150].

users and transmits on a selected cellular channel. The study focuses on the impact of different spectrum access schemes on the transmission outage probability. In [67], the authors propose a selection scheme for cellular users to choose between wireless-powered D2D relaying and direct transmission. Under a K-tier heterogeneous network model, the outage probability of cellular users is derived in closed-form expressions. Both [66] and [67] aim at improving the self-sustainable D2D communications through efficient spectrum allocation. However, the use of wireless-powered transmission is subject to channel availability. In particular, wireless-powered transmission is not feasible when all the channels are occupied. Different from these research efforts, our hybrid design allows transmission by ambient backscattering when wireless-powered transmission is infeasible, which does not cause noticeable interference to legitimate users [26, 68].

Different from the works [66, 67] that consider ambient RF energy harvesting, the work in [69] studies D2D communications with dedicated power beacons for wireless energy provisioning. Both energy outage and secrecy outage probabilities are analyzed under different power beacon allocation schemes. The work in [70] introduces a system model termed wirelessly powered backscatter communication network, which utilizes dedicated power beacons transmitting unmodulated carrier signals to power the network nodes. Once successfully powered, each node can transmit information by backscattering the signals from the same power beacon. From the studies in [69] and [70], it is confirmed that adopting power beacons increases the available wireless power, and thus facilitates both wireless-powered communications and backscatter communications. However, this approach is costly and not energy-efficient due to the use of power beacons.

More recently, ambient backscatter communications have been analyzed in wire-

less network environments. The authors in [71] investigate a cognitive radio network where a wireless-powered secondary user can either harvest energy or adopt ambient backscattering from a primary user on transmission. To maximize the throughput of the secondary user, a time allocation problem is developed to obtain the optimal time ratio between energy harvesting and ambient backscattering. The work in [72] introduces a hybrid backscatter communication as an alternative access scheme for a wireless-powered transmitter. Specifically, when the ambient RF signals are not sufficient to support wireless-powered communications, the transmitter can adopt either bistatic backscattering or ambient backscattering depending on the availability of a dedicated carrier emitter. A throughput maximization problem is formulated to find the optimal time allocation for the hybrid backscatter communication operation. Both [71] and [72] study deterministic scenarios. Instead, our work takes into account the spatial randomness of network components and focuses on investigating the impact of different spatial distributions.

3.2 Network Model and Stochastic Geometry Characterization

3.2.1 Network Model

We consider a hybrid M2M communications between the hybrid transmitter S and the associated hybrid receiver D in coexistence with ambient RF transmitters, e.g., cellular base stations and mobiles. As shown in Fig. 3.1, the hybrid transmitter is equipped with an RF energy harvester, an RF transmitter and a load modulator which enables both harvest-then-transmit (HTT) and ambient backscattering

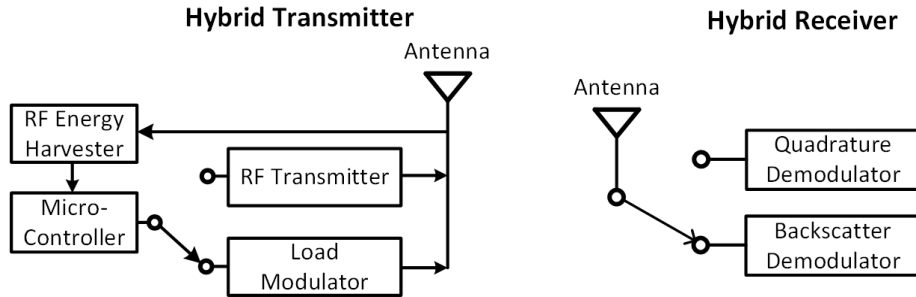


Figure 3.1: The structure of the hybrid transmitter and hybrid receiver.

functions. Accordingly, the hybrid receiver is equipped with both a quadrature demodulator and backscatter demodulator to decode the active transmission and ambient backscatter transmission, respectively. Fig. 3.2 illustrates our considered system model. We consider two groups of coexisting ambient transmitters, denoted as Φ and Ψ , respectively, which work on different frequency bands. The RF energy harvester of the hybrid transmitter scavenges on the transmission frequency of Φ .

If the hybrid transmitter is in ambient backscattering mode, it performs load modulation on the incident signals from Φ . Alternatively, when the hybrid transmitter is in HTT mode, it harvests energy from ambient transmitters in Φ , and transmits over a different frequency band used by ambient transmitters in Ψ .² The received signal at the hybrid receiver from the hybrid transmitter is impaired by the interference from Ψ . We assume that Φ and Ψ follow independent α -Ginibre point process (GPP) [56] which will be justified and detailed in Section 3.2.2. For example, the RF energy harvester of the hybrid transmitter scavenges energy from LTE-A cellular mobiles on 1800 MHz. In HTT mode, the active M2M transmission is performed using WiFi Direct [73] over 2.4 GHz, and gets interfered by the ambient

²Similar to [74], we assume that the hybrid transmitter decides the transmit frequency and indicates to the hybrid receiver through broadcasting in the preamble. Thus, the hybrid receiver is implemented to work on the transmit frequency of Φ and Ψ when the hybrid transmitter is in ambient backscattering mode and HTT mode, respectively.

users working on the same frequency band. The locations of the ambient users on 1800 MHz and those on 2.4 GHz are independent.

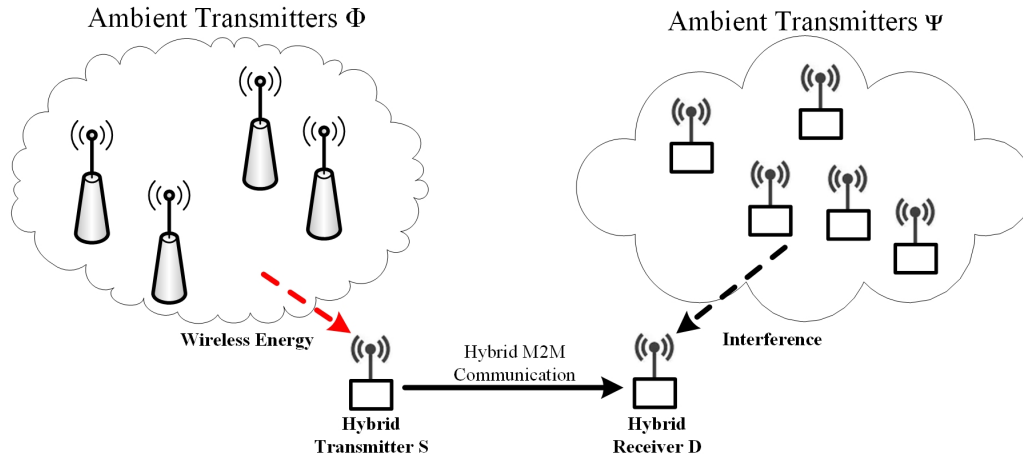


Figure 3.2: Illustration of the hybrid M2M communication.

Without loss of generality, the hybrid transmitter, denoted as S , and the associated hybrid receiver, denoted as D , are assumed to locate at the origin when we analyze their corresponding performance, respectively. In particular, the point processes Φ and Ψ are assumed to be supported on the circular observation windows \mathbb{O}_S and \mathbb{O}_D with radius R , which are centered at S and D , respectively. The transmit power of the ambient transmitters belonging to Φ and Ψ are denoted as P_A and P_B , respectively. Let ζ_A and ζ_B denote the spatial density of Φ and Ψ , respectively. And $\alpha \in (0, 1]$ represents the repulsion factor which measures the correlation among the spatial points in Φ and Ψ . Then, Φ can be represented by a homogeneous marked point process $\Phi = \{\mathbf{X}_A, \mathbf{C}_A, \mathcal{A}, \zeta_A, \alpha, P_A\}$, where $\mathbf{X}_A = \{\mathbf{x}_a | a \in \Phi\}$ denotes the set of locations of the ambient transmitters in Φ , $\mathbf{C}_A = \{c_a | a \in \Phi\}$ denotes the set of state indicators (in particular, $c_a = 1$ if transmitter a is on transmission in the reference time slot, and $c_a = 0$ otherwise), and \mathcal{A} denotes the set of active ambient transmitters of Φ observed in \mathbb{O}_S by the hybrid transmitter. We assume that c_a

is an independent and identically distributed (i.i.d.) random variable. Then, the *transmission load* of Φ can be calculated as $l_A = \mathbb{P}[c_a = 1]$, which measures the portion of time that an ambient transmitter is active. It is worth noting that the set of active transmitters in the reference time is a thinning point process with spatial density $l_A\zeta_A$. Similarly, Ψ is characterized by $\Psi = \{\mathbf{X}_B, \mathbf{C}_B, \mathcal{B}, \zeta_B, \alpha, P_B\}$, where \mathbf{X}_B denotes the set of the locations of transmitters in Ψ , \mathbf{C}_B is the set of state indicators for Ψ , and \mathcal{B} denotes the set of the ambient transmitters of Ψ observed in \mathbb{O}_D by the hybrid receiver. $l_B = \mathbb{P}[c_b = 1]$ denotes the transmission load of Ψ , where c_b is the state indicator of $b \in \mathcal{B}$. Let ξ represent the ratio of $l_B\zeta_B$ to $l_A\zeta_A$, i.e., $\xi = l_B\zeta_B/l_A\zeta_A$, referred to as the interference ratio. A larger value of ξ indicates a higher level of interference.

Let \mathbf{x}_S represent the location of the hybrid transmitter. The power of the incident RF signals at the antenna of S can be calculated as $P_I = P_A \sum_{a \in \mathcal{A}} h_{a,S} \|\mathbf{x}_a - \mathbf{x}_S\|^{-\mu}$, where $h_{x,y}$ represents the fading channel gain between x and y on the transmit frequency of Φ , and μ denotes the path loss exponent. The circuit of the hybrid transmitter becomes functional if it can extract sufficient energy from the incident RF signals. When the hybrid transmitter works in different modes (i.e., either HTT or ambient backscattering), the hardware circuit consumes different amounts of energy.³ Let ρ_B and ρ_H denote the circuit power consumption rates (in Watt) in ambient backscattering and HTT modes, respectively. If the hybrid transmitter cannot harvest sufficient energy, an outage occurs.

In ambient backscattering mode, if the instantaneous energy harvesting rate (in Watt) exceeds ρ_B , the hybrid transmitter can generate modulated backscatter. Dur-

³The typical circuit power consumption rate of a wireless-powered transmitter ranges from hundreds of micro-Watts to several milli-Watts [77, 78], while that of a backscatter transmitter ranges from several micro-Watts to hundreds of micro-Watts [23].

ing backscattering process, a fraction of the incident signal power, denoted as P_H , is rectified for conversion from RF signal to direct current (DC), and the residual amount of signal power, denoted as P_R , is reflected to carry the modulated information. In ambient backscattering mode, the energy harvesting rate (in Watt) can be represented as [75, 76] $P_E^B = \beta P_H = \beta \varrho P_I$, where $0 < \beta \leq 1$ denotes the efficiency of RF-to-DC energy conversion, and ϱ represents the fraction of the incident RF power for RF-to-DC energy conversion. Note that the value of ϱ depends on the symbol constellation adopted for multi-level load modulation [76]. For example, ϱ is 0.625 on average assuming equiprobable symbols if binary constellations are adopted with modulator impedance values set as 0.5 and 0.75 [75].

Let \mathbf{x}_D represent the location of the hybrid receiver. $d = \|\mathbf{x}_S - \mathbf{x}_D\|$ denotes the distance between S and D. Then, in ambient backscattering mode, the power of the received backscatter at D from S can be calculated as $P_{S,D} = \delta P_I (1 - \varrho) h_{S,D} d^{-\mu}$ if $P_E^B > \rho_B$ and $P_{S,D} = 0$ otherwise. Here $0 < \delta \leq 1$ is the backscattering efficiency of the transmit antenna, which is related to the antenna aperture [79]. If S is active in ambient backscattering mode, the resulted signal-to-noise ratio (SNR) at D is

$$\nu_B = \frac{P_{S,D}}{\sigma^2} = \frac{\delta P_I (1 - \varrho) h_{S,D}}{d^\mu \sigma^2}, \quad (3.1)$$

where σ^2 is the variance of additive white Gaussian noise (AWGN).

If the received SNR ν_B is above a threshold τ_B , D is able to successfully decode information from the modulated backscatter at a pre-designed rate T_B (in bits per second (bps)). This backscatter transmission rate is dependent on the setting of resistor-capacitor circuit elements.

When the hybrid transmitter S chooses to adopt active RF transmission, it is

operated by the HTT protocol [29]. In HTT mode, the hybrid transmitter works in a time-slot based manner. Specifically, in each time slot, the first period, with time fraction ω , is for harvesting energy, during which the impedance of the load modulator is tuned to fully match that of the antenna to maximize the energy conversion efficiency. The corresponding energy harvesting rate is $P_E^H = \omega\beta P_I$. This harvested energy is first utilized to power the circuit. Then the remaining energy, if available, is stored in an energy storage. If the harvested energy is enough to operate the circuit, the hybrid transmitter spends the rest of the period $(1 - \omega)$ to perform active transmission with the stored energy.

In the active transmission phase, the transmit power of S is $P_S = \frac{P_E^H - \rho_H}{1 - \omega}$ if $P_E^H > \rho_H$ and $P_S = 0$ otherwise. Then, the received SINR at D can be expressed as

$$\nu_H = \frac{P_S \tilde{h}_{S,D} d^{-\mu}}{\sum_{b \in \mathcal{B}} P_B \tilde{h}_{b,D} \|\mathbf{x}_b - \mathbf{x}_D\|^{-\mu} + \sigma^2}, \quad (3.2)$$

where $\tilde{h}_{x,y}$ denotes the fading channel gain between x and y on the transmit frequency of Ψ .

As the hybrid M2M communications and the transmission from ambient transmitters may occur in different environments, we consider different fading channels for $h_{S,D}$, $\tilde{h}_{S,D}$, $h_{a,S}$ and $\tilde{h}_{b,D}$. Specifically, $h_{S,D}$ and $\tilde{h}_{S,D}$ are assumed to follow Rayleigh fading. Both $h_{a,S}$ and $\tilde{h}_{b,D}$ follow i.i.d. Nakagami- m fading, which is a general channel fading model that contains Rayleigh distribution as a special case when $m = 1$. This channel model allows a flexible evaluation of the impact of the ambient signals.⁴ The fading channel gains are expressed as $h_{a,S}, \tilde{h}_{b,D} \sim \mathcal{G}(m, \theta/m)$ and $h_{S,D}, \tilde{h}_{S,D} \sim \mathcal{E}(\lambda)$,

⁴Our work can be extended to the case when $h_{S,D}$ and $\tilde{h}_{S,D}$ also follow a Nakagami- m distribution. However, the resulted analytical expressions bring about high computational complexity without much insight. Therefore, we focus on exponentially distributed $h_{S,D}$ and $\tilde{h}_{S,D}$ in this chapter.

where θ and λ are expectation of the corresponding fading channel gains.

Let W denote the frequency bandwidth for active transmission in HTT mode. The transmission capacity of a hybrid transmitter in HTT mode can be computed as $\mathcal{T}_H = (1 - \omega)W \log_2(1 + \nu_H)$ if $P_E^H > \rho_H$ and $\nu_H > \tau_H$, and $\mathcal{T}_H = 0$ otherwise. Here τ_H is the minimum SINR threshold for the hybrid receiver to successfully decode from the received active RF signals [50].

For operation of our proposed hybrid transmitter, we consider two mode selection protocols, namely, *power threshold-based protocol* (PTP) and *SNR threshold-based protocol* (STP).

- Under PTP, a hybrid transmitter first detects the available energy harvesting rate P_E^H . If P_E^H is below the threshold which is needed to power the RF transmitter circuit (for active transmission), i.e., $P_E^H \leq \rho_H$, ambient backscattering mode will be used. Otherwise, HTT mode will be adopted.
- Under STP, the hybrid transmitter first attempts to transmit by backscattering. If the achieved SNR at the receiver is above the threshold which is needed to decode information from the backscatter, i.e., $\nu_B > \tau_B$, the transmitter will be in ambient backscattering mode. Otherwise, it will switch to HTT mode.

The motivation behind PTP is to use active transmission for higher throughput if the ambient energy resource is abundant, and adopt backscattering to diminish the occurrences of energy outage otherwise. The motivation of STP is to enjoy full-time transmission by backscattering when the achievable SNR is high, and adopt HTT if ambient backscattering does not have good performance. Note that for implementation of the two protocols, PTP allows the transmitter to operate independently based on its local information while STP requires the transmitter to obtain feedback

Table 3.1: NOTATIONS.

Symbol	Definition
α	Repulsion factor of the ambient transmitters
β	RF-to-DC energy conversion efficiency of the hybrid transmitter
d	The distance between the hybrid transmitter and the hybrid receiver
μ	Path loss exponent
ω	The time fraction used to harvest energy in HTT mode
ρ_B, ρ_H	The circuit power consumption in ambient backscattering mode and HTT mode, respectively
P_A, P_B	The transmit power of ambient transmitters operating on energy harvesting frequency and transmission frequency, respectively
P_I	The incident RF power at the antenna of the typical hybrid transmitter
P_E^B, P_E^H	The RF energy harvesting rate of a typical hybrid transmitter in ambient backscattering mode and HTT mode, respectively
σ^2	The variance of AWGN
δ	Backscattering coefficient
ξ	The ratio between ζ_B and ζ_A
ζ_A, ζ_B	The spatial density of ambient transmitters in Φ and Ψ , respectively
ν_B, ν_H	Achieved SNR and SINR of a hybrid transmitter in ambient backscattering mode and HTT mode, respectively
τ_B, τ_H	Target SNR and SINR for a hybrid receiver to decode information in ambient backscattering mode and HTT mode, respectively

from the receiver.

We investigate the two simple protocols described above in view of their practicality of implementation and tractable analysis. We will reveal how the naive mechanism adopted in each protocol affects different performance metrics. More sophisticated protocols that offer superior performance can be designed by utilizing system information such as channel state information feedback, interference detection, and energy source localization. However, these protocols may require more computational overhead as well as complicated and expensive hardware implementation, which are not practical for low-power devices based on energy harvesting.

Remark 1: The analytical expressions derived in this chapter represent a lower bound on the achievable performance. This is because for implementation simplicity

and practicability we consider that the mode selection is performed only once at the beginning of hybrid M2M communication. The selected mode may not always be the better choice when the network channel condition varies. The analytical approach presented in the chapter can be straightforwardly extended to the case when mode selection is performed at the beginning of each fading block.

The main notations used in this chapter are listed in Table 5.1.

3.2.2 Geometric Modeling of the Systems

Due to its tractability, the Poisson point process (PPP) has been widely adopted for modeling different types of wireless networks [50]. PPP abstracts each randomly located point according to a uniform distribution in the Euclidean space. However, as pointed out in [52], PPP modeling only serves as lower bounds to the coverage probability and mean rate of real-world deployment. The reason is that the spatial points in a PPP may locate very close to each other because of independence. This calls for the need of more sophisticated and general geometric approaches to model the correlation among spatial points. In this context, GPP and its variants have attracted considerable attention. Recent research work has adopted GPP in [80], α -GPP in [81–84] and β -GPP in [85] to model the distribution of cellular base stations. In this chapter, the performance analysis of the hybrid M2M communications is based on α -GPP [56]. We use α -GPP because it renders tractable analytical expressions in terms of Fredholm determinants. The Fredholm determinant is a generalized determinant of a matrix defined by bounded operators on a Hilbert space and has shown to be efficient for numerical evaluation of the relevant quantities [56].

3.2.3 Performance Metrics

We measure the performance of the hybrid M2M communications in three important metrics, namely, energy outage probability, coverage probability, and throughput.

The hybrid transmitter experiences an energy outage when the energy obtained from the ambient transmitters is not enough to support its circuit operation. Let \mathcal{O}_B and \mathcal{O}_H denote the energy outage probability of the hybrid transmitter being in ambient backscattering mode and HTT mode, respectively. Mathematically, the overall energy outage probability is given as

$$\mathcal{O} = \mathcal{B}\mathcal{O}_B + (1 - \mathcal{B})\mathcal{O}_H = \mathcal{B}\mathbb{P}[P_E^B \leq \rho_B] + (1 - \mathcal{B})\mathbb{P}[P_E^H \leq \rho_H], \quad (3.3)$$

where \mathcal{B} denotes the probability that the hybrid transmitter selects ambient backscattering mode.

The transmission of the hybrid transmitter is considered to be successful if the achieved SNR or SINR at the associated receiver exceeds its target threshold. We define coverage as an event of successful transmission. Let \mathcal{C}_B and \mathcal{C}_H denote the coverage probability of the hybrid transmitter being in ambient backscattering mode and HTT mode, respectively. Then, the overall coverage probability is given as

$$\begin{aligned} \mathcal{C} &= \mathcal{B}\mathcal{C}_B + (1 - \mathcal{B})\mathcal{C}_H \\ &= \mathcal{B}\mathbb{P}[\nu_B > \tau_B, P_E^B > \rho_B] + (1 - \mathcal{B})\mathbb{P}[\nu_H > \tau_H, P_E^H > \rho_H]. \end{aligned} \quad (3.4)$$

Moreover, the average throughput achieved by the hybrid transmitter is given as

$$\mathcal{T} = \mathcal{B}\mathcal{T}_B + (1 - \mathcal{B})\mathcal{T}_H, \quad (3.5)$$

where \mathcal{T}_B denotes the average throughput in ambient backscattering mode and \mathcal{T}_H has been defined in Subsection 4.2.

An upper bound on the achievable performance can be obtained by considering block fading channels with mode selection performed at the beginning of each fading block. As we focus on the impact of system parameters and comparison of the proposed mode selection protocols, we omit presenting the upper bound. The upper bound performance can be derived by following the same analytical approach presented in this chapter.

3.3 Analytical Results

In this section, we derive analytical expressions for the performance metrics introduced in Section 3.2.3 based on the repulsive point process framework introduced in Section 3.2.2.

3.3.1 Energy Outage Probability

We first derive the expressions of the energy outage probability based on the definition in (3.3).

Theorem 3.3.1 *Under PTP, the energy outage probability of a hybrid transmitter is calculated as*

$$\mathcal{O}_{\text{PTP}} = F_{P_I}\left(\frac{\rho_H}{\omega\beta}\right) \left(F_{P_I}\left(\frac{\rho_B}{\beta\varrho}\right) - F_{P_I}\left(\frac{\rho_H}{\omega\beta}\right) + 1 \right), \quad (3.6)$$

where $F_{P_I}(\rho)$ is the CDF of P_I given as

$$F_{P_I}(\rho) = \mathcal{L}^{-1} \left\{ \frac{\text{Det}(\text{Id} + \alpha \mathbb{A}_\Phi(s))^{-\frac{1}{\alpha}}}{s} \right\} (\rho), \quad (3.7)$$

wherein \mathcal{L}^{-1} means inverse Laplace transform and $\mathbb{A}_\Phi(s)$ is given by

$$\begin{aligned} \mathbb{A}_\Phi(s) = & \sqrt{1 - \left(1 + \frac{s\theta P_A}{m\|\mathbf{x} - \mathbf{x}_S\|^\mu}\right)^{-m}} \\ & \times G_\Phi(\mathbf{x}, \mathbf{y}) \sqrt{1 - \left(1 + \frac{s\theta P_A}{m\|\mathbf{y} - \mathbf{x}_S\|^\mu}\right)^{-m}}, \end{aligned} \quad (3.8)$$

and G_Φ is the Ginibre kernel of Φ defined as

$$G_\Phi(\mathbf{x}, \mathbf{y}) = l_A \zeta_A e^{\pi l_A \zeta_A \mathbf{x} \bar{\mathbf{y}}} e^{-\frac{\pi l_A \zeta_A}{2} (|\mathbf{x}|^2 + |\mathbf{y}|^2)}, \quad \mathbf{x}, \mathbf{y} \in \mathcal{A}. \quad (3.9)$$

For readability, we present the proof of **Theorem 3.3.1** in Appendix 3.6.1.

Consequently, we extend the above outcome in **Theorem 3.3.1** to the case of STP by altering the mode selection probability based on the STP criteria, resulting in the following Theorem.

Theorem 3.3.2 *Under STP, the energy outage probability of a hybrid transmitter is*

$$\mathcal{O}_{\text{STP}} = \int_{\frac{\rho_B}{\beta e}}^{\infty} \exp\left(-\frac{\lambda \tau_B d^\mu \sigma^2}{\delta \rho (1 - \varrho)}\right) f_{P_I}(\rho) d\rho \left(F_{P_I}\left(\frac{\rho_B}{\beta \varrho}\right) - F_{P_I}\left(\frac{\rho_H}{\omega \beta}\right) \right) + F_{P_I}\left(\frac{\rho_H}{\omega \beta}\right), \quad (3.10)$$

where $F_{P_I}(\rho)$ has been given in (3.7), and $f_{P_I}(\rho)$ is the PDF of P_I calculated as

$$f_{P_I}(\rho) = \mathcal{L}^{-1} \left\{ \text{Det}(\text{Id} + \alpha \mathbb{A}_\Phi(s))^{-\frac{1}{\alpha}} \right\} (\rho), \quad (3.11)$$

wherein $\mathbb{A}_\Phi(s)$ has been defined in (3.8).

The proof of Theorem 3.3.2 is shown in Appendix 3.6.2.

Note that both \mathcal{O}_{PTP} and \mathcal{O}_{STP} are functions of ζ_A , not ζ_B . Thus, given ζ_A and the transmission load l_A , the interference ratio ξ does not affect the energy outage probability. We also note that similar to the stochastic geometry analysis based on PPP in the existing literature, e.g., [52], it is difficult to see the relationship between the performance metric and system parameters directly from the general-case results in Theorems 3.3.1 and 3.3.2 derived based on the α -GPP framework. However, these general-case results can be simplified in some special cases. We then investigate a special setting which considerably simplifies the above results.

Corollary 1 *When the distribution of ambient transmitters in Φ follows a PPP, the RF signals from these transmitters experience Rayleigh fading (i.e., $h_{a,s} \sim \mathcal{E}(1)$), and the path loss exponent is equal to 4, the energy outage probability of a hybrid transmitter can be evaluated by (3.6) under PTP and (3.10) under STP, with $f_{P_I}(\rho)$ and $F_{P_I}(\rho)$ expressed, respectively, as*

$$f_{P_I}(\rho) = \frac{1}{4} \left(\frac{\pi}{\rho} \right)^{\frac{3}{2}} \zeta_A \sqrt{P_A} \exp \left(-\frac{\pi^4 \zeta_A^2 P_A}{16\rho} \right), \quad (3.12)$$

$$F_{P_I}(\rho) = \text{erfc} \left(\frac{\zeta_A \sqrt{P_A} \pi^2}{4\sqrt{\rho}} \right). \quad (3.13)$$

The proof of **Corollary 3** is given in Appendix 4.8.2.

3.3.2 Coverage Probability

Next, we consider the coverage probability between a hybrid M2M transmitter-receiver pair. We have the coverage probability of PTP described as follows.

Theorem 3.3.3 *The coverage probability of the hybrid M2M communications under PTP is*

$$\begin{aligned} \mathcal{C}_{\text{PTP}} = & \left(1 - F_{P_I}\left(\frac{\rho_H}{\omega\beta}\right)\right) \int_{\frac{\rho_H}{\beta\omega}}^{\infty} \exp\left(-\frac{\lambda\tau_H d^\mu \sigma^2(1-\omega)}{\omega\beta\rho - \rho_H}\right) \text{Det}(\text{Id} + \alpha\mathbb{B}_\Psi(\rho))^{-\frac{1}{\alpha}} f_{P_I}(\rho) d\rho \\ & + F_{P_I}\left(\frac{\rho_H}{\omega\beta}\right) \int_{\frac{\rho_B}{\beta\varrho}}^{\infty} \exp\left(-\frac{\lambda\tau_B d^\mu \sigma^2}{\delta\rho(1-\varrho)}\right) f_{P_I}(\rho) d\rho, \end{aligned} \quad (3.14)$$

where $F_{P_I}(\rho)$ and $f_{P_I}(\rho)$ have been obtained in (3.7) and (3.11), respectively, and $\mathbb{B}_\Psi(\rho)$ is

$$\begin{aligned} \mathbb{B}_\Psi(\rho) = & \sqrt{1 - \left(1 + \frac{\theta\lambda\tau_H d^\mu(1-\omega)P_B}{m(\omega\beta\rho - \rho_H)\|\mathbf{x} - \mathbf{x}_D\|^\mu}\right)^{-m}} \\ & \times G_\Psi(\mathbf{x}, \mathbf{y}) \sqrt{1 - \left(1 + \frac{\theta\lambda\tau_H d^\mu(1-\omega)P_B}{m(\omega\beta\rho - \rho_H)\|\mathbf{y} - \mathbf{x}_D\|^\mu}\right)^{-m}}, \end{aligned} \quad (3.15)$$

wherein G_Ψ is the Ginibre kernel of Ψ defined as

$$G_\Psi(\mathbf{x}, \mathbf{y}) = l_B \zeta_B e^{\pi l_B \zeta_B \mathbf{x} \bar{\mathbf{y}}} e^{-\frac{\pi l_B \zeta_B}{2} (|\mathbf{x}|^2 + |\mathbf{y}|^2)}, \quad \mathbf{x}, \mathbf{y} \in \mathcal{B}. \quad (3.16)$$

The proof of **Theorem 3.3.3** is shown in Appendix 3.6.4.

Moreover, we derive the coverage probability for STP in the following Theorem.

Theorem 3.3.4 *The coverage probability of the hybrid M2M communications under*

STP is

$$\begin{aligned} \mathcal{C}_{\text{STP}} &= \int_{\frac{\rho_{\text{H}}}{\beta\omega}}^{\infty} \exp\left(-\frac{\lambda\tau_{\text{H}}d^{\mu}(1-\omega)\sigma^2}{\omega\beta\rho - \rho_{\text{H}}}\right) \text{Det}(\text{Id} + \alpha\mathbb{B}_{\Psi}(\rho))^{-\frac{1}{\alpha}} f_{P_I}(\rho) d\rho \\ &\times \int_0^{\frac{\rho_{\text{B}}}{\beta\varrho}} \exp\left(-\frac{\lambda\tau_{\text{B}}d^{\mu}\sigma^2}{\delta\rho(1-\varrho)}\right) f_{P_I}(\rho) d\rho + \left[\int_{\frac{\rho_{\text{B}}}{\beta\varrho}}^{\infty} \exp\left(-\frac{\lambda\tau_{\text{B}}d^{\mu}\sigma^2}{\delta\rho(1-\varrho)}\right) f_{P_I}(\rho) d\rho \right]^2, \end{aligned} \quad (3.17)$$

where $f_{P_I}(\rho)$ has been obtained in (3.11), and $\mathbb{B}_{\Psi}(\rho)$ is defined in (3.15).

Proof. According to the criteria of STP, \mathcal{C}_{STP} can be expressed by \mathcal{C}_{PTP} in (3.37) with \mathcal{B}_{PTP} replaced by \mathcal{B}_{STP} given in (3.33). Therefore, (3.17) can be obtained from (3.14) through the aforementioned replacement. ■

3.3.3 Throughput

Then, we move on to calculate the average throughput that can be achieved over a hybrid M2M communication link. We have the average throughput of PTP presented as follows:

Theorem 3.3.5 *Under PTP, the average throughput of a hybrid M2M communication link can be computed as*

$$\begin{aligned} \mathcal{T}_{\text{PTP}} &= T_{\text{B}} F_{P_I}\left(\frac{\rho_{\text{B}}}{\omega\beta}\right) \int_{\frac{\rho_{\text{B}}}{\beta\varrho}}^{\infty} \exp\left(-\frac{\lambda\tau_{\text{B}}d^{\mu}\sigma^2}{\delta\rho(1-\varrho)}\right) f_{P_I}(\rho) d\rho + (1-\omega)W\left(1 - F_{P_I}\left(\frac{\rho_{\text{B}}}{\omega\beta}\right)\right) \\ &\times \int_{\log_2(1+\tau_{\text{H}})}^{\infty} \int_{\frac{\rho_{\text{H}}}{\beta\omega}}^{\infty} \text{Det}(\text{Id} + \alpha\mathbb{C}_{\Psi}(\rho))^{-\frac{1}{\alpha}} \exp\left(-\frac{\lambda d^{\mu}\sigma^2(1-\omega)(2^t-1)}{\omega\beta\rho - \rho_{\text{H}}}\right) f_{P_I}(\rho) d\rho dt, \end{aligned} \quad (3.18)$$

where $F_{P_I}(\rho)$ and $f_{P_I}(\rho)$ have been obtained in (3.7) and (3.11), respectively, and

$\mathbb{C}_\Psi(\rho)$ is computed as

$$\begin{aligned} \mathbb{C}_\Psi(\rho) = & \sqrt{1 - \left(1 + \frac{\theta \lambda d^\mu (2^t - 1)(1 - \omega) P_B}{m(\omega \beta \rho - \rho_H) \|\mathbf{x} - \mathbf{x}_D\|^\mu}\right)^{-m}} \\ & \times G_\Psi(\mathbf{x}, \mathbf{y}) \sqrt{1 - \left(1 + \frac{\theta \lambda d^\mu (2^t - 1)(1 - \omega) P_B}{m(\omega \beta \rho - \rho_H) \|\mathbf{y} - \mathbf{x}_D\|^\mu}\right)^{-m}}. \end{aligned} \quad (3.19)$$

The proof of **Theorem 3.3.5** is presented in Appendix 3.6.5.

Consequently, utilizing \mathcal{B}_{STP} obtained in (3.33), we arrive at the following theorem stating the achievable throughput for STP.

Theorem 3.3.6 *Under STP, the average throughput of a hybrid M2M communication link can be computed as*

$$\begin{aligned} \mathcal{T}_{\text{STP}} = & T_B \left[\int_{\frac{\rho_B}{\beta \varrho}}^{\infty} \exp\left(-\frac{\lambda \tau_B d^\mu \sigma^2}{\delta \rho (1 - \varrho)}\right) f_{P_I}(\rho) d\rho \right]^2 + (1 - \omega) W \int_0^{\frac{\rho_B}{\beta \varrho}} \exp\left(-\frac{\lambda \tau_B d^\mu \sigma^2}{\delta \rho (1 - \varrho)}\right) \\ & \times f_{P_I}(\rho) d\rho \int_{\log_2(1 + \tau_H)}^{\infty} \int_{\frac{\rho_H}{\beta \omega}}^{\infty} \exp\left(-\frac{\lambda d^\mu \sigma^2 (1 - \omega) (2^t - 1)}{\omega \beta \rho - \rho_H}\right) \\ & \times \text{Det}(\text{Id} + \alpha \mathbb{C}_\Psi(\rho))^{-\frac{1}{\alpha}} f_{P_I}(\rho) d\rho dt, \end{aligned} \quad (3.20)$$

where $f_{P_I}(\rho)$ has been obtained in (3.11) and $\mathbb{C}_\Psi(\rho)$ is defined in (3.19).

Proof. By replacing \mathcal{B}_{PTP} in (3.40) with \mathcal{B}_{STP} expressed as (3.33), \mathcal{T}_{STP} can be obtained as in (3.20). ■

Though Theorems 3.3.5 and 3.3.6 do not provide closed-form analytical expressions, the integrals can be efficiently evaluated by numerical analysis software like Matlab and Mathematica. Moreover, the expressions can be simplified considerably in some special cases like Corollary 3. We only present the general results for the throughput expressions of PTP and STP in this chapter due to limited space.

Table 3.2: Parameter Setting.

Symbol	μ	d	R	θ	λ	ϱ	β	δ	τ_H	τ_B
Value	4	5 m	30 m	1	1	0.625 [75]	30 % [60]	1	-40 dB	5 dB

3.4 Performance Evaluation and Analysis

In this section, we validate our derived analytical expressions and conduct performance analysis based on numerical simulations. The performance of the proposed hybrid M2M communications is evaluated in the scenario coexisting with two groups of ambient transmitters Φ and Ψ , respectively, working on the energy harvesting frequency and active RF transmission frequency of the hybrid transmitter. The transmit power level of the transmitters in Φ and Ψ are set to be $P_A = P_B = 0.2$ W, which is within the typical range of uplink transmit power for mobile devices. The interference ratio and transmission load are set to $\xi = 0.2$ and $l_A = l_B = 1$, respectively. The bandwidth of the transmitted signal W in HTT mode is 1 MHz, and the noise variance σ^2 is -120 dBm/Hz. When the hybrid transmitter is in HTT mode, we assume equal time duration for energy harvesting and information transmission and the circuit power consumption is set at $113 \mu\text{W}$ [86]. In ambient backscattering mode, we consider $\rho_B = 8.9 \mu\text{W}$ for circuit power consumption and $T_B = 1$ kbps for the transmission rate [26].

For the simulation of α -GPP, we consider three typical scenarios, strong repulsion ($\alpha = -1$), medium repulsion ($\alpha = -0.5$) and no repulsion ($\alpha \rightarrow 0$, i.e., PPP), representing different social degrees among the ambient transmitters. In addition, for the evaluation of the Fredholm determinant, we adopt (2.6) and set N_{closed} to be 100. The other system parameters adopted in this section are listed in Table 4.2 unless otherwise stated.

In the remaining of this section, the lines and symbols are used to represent the

results evaluated from analytical expressions and Monte Carlo simulations, respectively. Additionally, for the comparison purpose, we evaluate the performance of a pure wireless-powered transmitter operated by the HTT protocol and a pure ambient backscatter transmitter as references, the plots of which are labeled as “Pure HTT” and “Pure Ambient Backscattering”, respectively. The performance of a pure wireless-powered transmitter (called pure HTT transmitter) and a pure ambient backscatter transmitter can be obtained by setting the hybrid transmitter in HTT mode and ambient backscattering mode, respectively, in all conditions. Specifically, the energy outage probability, coverage probability and average throughput of the pure ambient backscatter transmitter can be evaluated by \mathcal{O}_B in (4.5), \mathcal{C}_B in (3.35) and \mathcal{T}_B in (3.38), respectively. Moreover, the energy outage probability, coverage probability and average throughput of the pure HTT transmitter can be evaluated by \mathcal{O}_H in (3.28), \mathcal{C}_H in (3.36) and \mathcal{T}_H in (3.39), respectively.

We first examine the energy outage probabilities. Figs. 3.3 and 3.4 show \mathcal{O}_{PTP} and \mathcal{O}_{STP} obtained in (3.6) and (3.10), respectively, as a function of ζ_A . Note that when ζ_A varies from 0 to 0.04, equivalently, the average number of ambient transmitters changes from 0 to 113. The accuracy of the energy outage probability expressions are validated by the simulation results with different values of α and μ under different transmission load l_A and fading factors. In principle, larger ζ_A results in larger incident power at the hybrid transmitter, thus decreasing energy outage probabilities under a certain operation mode. However, one finds that only \mathcal{O}_{STP} is a monotonically decreasing function of ζ_A while \mathcal{O}_{PTP} not necessarily is. This is because the energy outage probability in HTT mode is higher than that in ambient backscattering mode given a certain ζ_A . PTP works in ambient backscattering mode when ζ_A is low and \mathcal{O}_{PTP} first decreases with the increase of ζ_A . When ζ_A reaches a certain

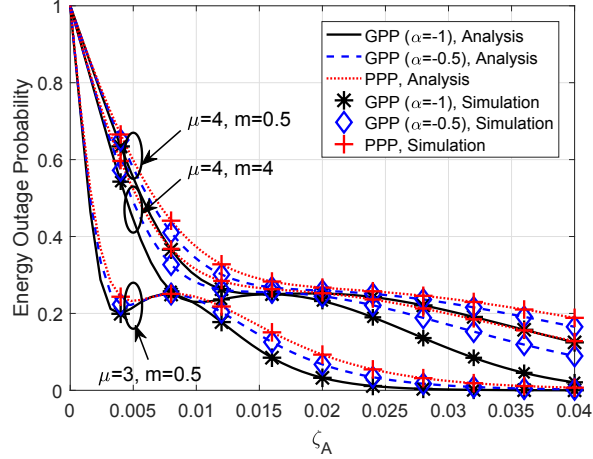


Figure 3.3: \mathcal{O}_{PTP} as a function of ζ_A .

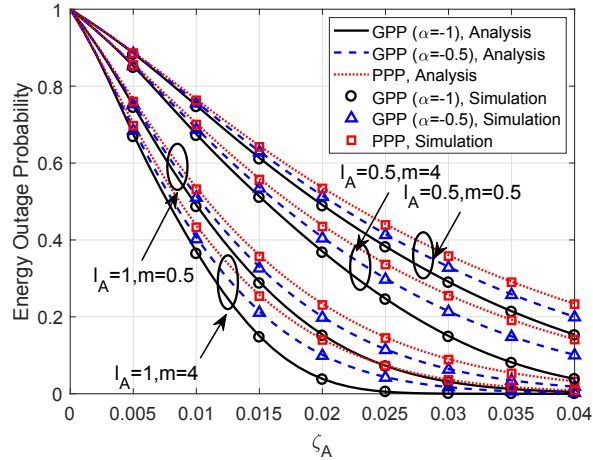


Figure 3.4: \mathcal{O}_{STP} as a function of ζ_A .

level (e.g., 0.005 for case $\mu = 3$), the hybrid transmitter is more in HTT mode, thus causing an increase of \mathcal{O}_{PTP} . As for STP, it is in HTT mode when ζ_A is low. When ζ_A becomes higher, the STP is more in ambient backscattering mode, which means that lower energy outage probability can be achieved. Therefore, mode switching results in a smooth and monotonic performance measure for \mathcal{O}_{STP} .

From both Figs. 3.3 and 3.4, we observe that the repulsion factor α among ambient transmitters has a considerable impact on energy outage probability. In other words, stronger attraction among the ambient transmitters leads to a lower en-

energy outage probability of the hybrid transmitter. This can be understood that the incident power is more affected by the ambient transmitters in the vicinity of the hybrid transmitter. Strong repulsion generates a more scattered distribution of ambient transmitters guaranteeing that the hybrid transmitter is surrounded by ambient transmitters. By contrast, in the case of PPP, the distribution of ambient transmitters exhibits clustering behavior. Therefore, the likelihood that the hybrid transmitter has ambient transmitters nearby turns smaller, resulting in a higher chance of energy outage.

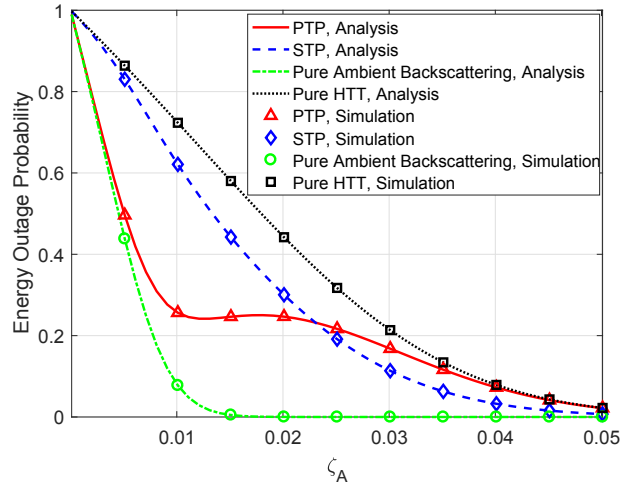


Figure 3.5: Comparison of energy outage probabilities. ($\alpha = -1$)

We observe that either a smaller path loss exponent (e.g., $\mu = 3$ in Fig. 3.3) or a larger Nakagami shape parameter m (e.g., $m = 4$ in Fig. 3.4) can reduce energy outage probabilities as both render less propagation attenuation. Additionally, as shown in Fig. 3.4, the transmission load l_A is directly related to the aggregated energy harvesting rate, and thus the energy outage probability is inversely proportional to l_A .

Then, in Fig. 3.5, we compare energy outage probability of PTP, STP, pure am-

bient backscattering, and pure HTT under different ambient transmitter densities. It can be found that energy outage probabilities are directly proportional to ζ_A . As expected, the pure ambient backscatter transmitter experiences less energy outage than the pure HTT transmitter in all cases due to lower circuit power consumption. Moreover, we observe that in terms of the energy outage probability, PTP is advantageous over STP when ζ_A is low (e.g., smaller than 0.02), and is outperformed by STP when ζ_A is high. This is due to the fact that PTP and STP, respectively, have better chance to be in ambient backscattering and HTT modes if ζ_A is low, and tend to switch to the other mode otherwise.

Figs. 3.6 and 3.7 illustrate how the coverage probabilities \mathcal{C}_{PTP} and \mathcal{C}_{STP} obtained in (3.14) and (3.17), respectively, vary with ambient transmitter density ζ_A under different transmission loads and fading coefficients. In principle, larger density ζ_A , repulsion factor α , transmission load l_A , and Nakagami shape parameter m lead to more incident power, and thus, result in increased transmit power at the hybrid transmitter (either in ambient backscattering mode or in HTT mode) to improve the coverage probability. The mentioned effects on the coverage probability have been verified for both PTP and STP in Figs. 3.6 and 3.7, respectively, which indicates that both \mathcal{C}_{PTP} and \mathcal{C}_{STP} are monotonically increasing functions of ζ_A , α , l_A and m . Note that from Figs. 3.6 and 3.7, with the increase of ζ_A , the coverage probabilities tend to be steady below 1. This is because, given an interference ratio ξ , the increase of ζ_A not only provides the hybrid transmitter with more harvested energy to transmit, but also leads to more interference that harms the transmission.

Fig. 3.8 compares coverage probabilities (as functions of density ζ_A) of PTP, STP, pure ambient backscattering, and pure HTT. When ξ is small (i.e., $\xi = 0.2$) as shown in Fig. 3.8(a), the pure HTT transmitter experiences low interference, and

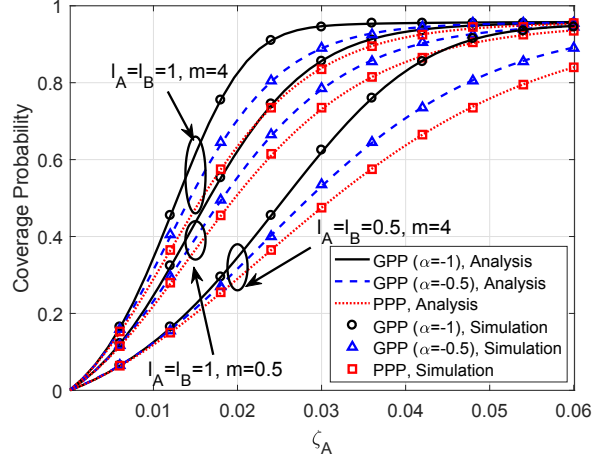


Figure 3.6: \mathcal{C}_{PTP} as a function of ζ_A .

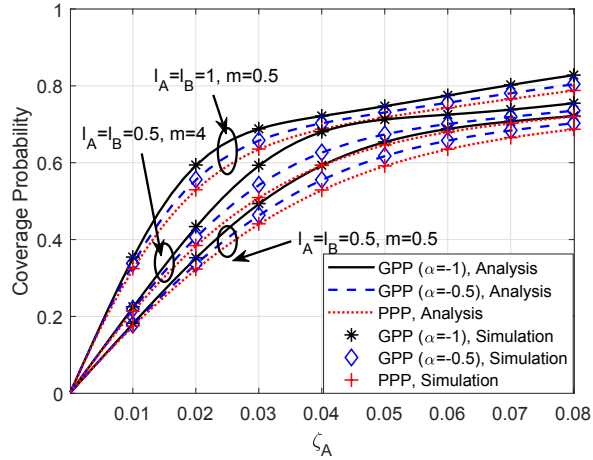
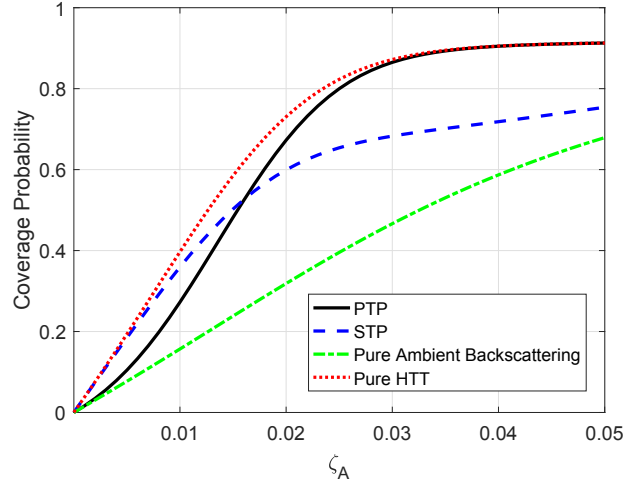
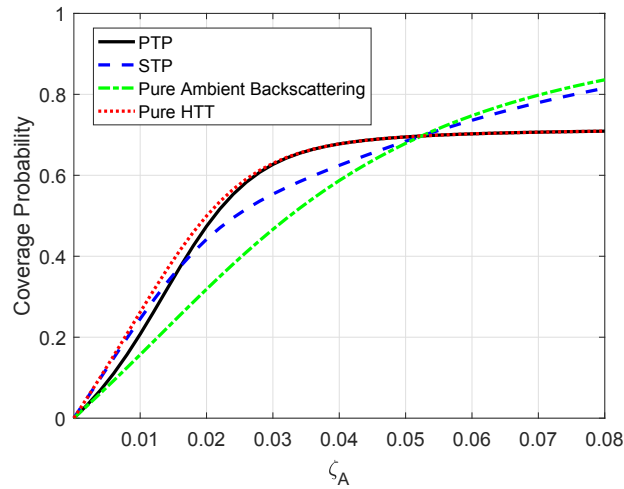


Figure 3.7: \mathcal{C}_{STP} as a function of ζ_A .

thus, achieves significantly higher coverage probability than pure ambient backscattering. However, in the case with high interference ratio (i.e., $\xi = 0.8$) as depicted in Fig. 3.8(b), their performance gap becomes smaller and pure ambient backscattering outperforms pure HTT when ζ_A is large (e.g., above 0.06), due to the high interference received by the pure HTT transmitter. We also observe that PTP achieves similar performance to that of STP under small ζ_A and is obviously outperformed by STP as ζ_A grows larger (e.g., above 0.06). The reason behind is that PTP selects operation mode solely based on the incident power and is unaware of the interference



(a) Comparison of coverage probabilities. ($\xi = 0.2$)



(b) Comparison of coverage probabilities. ($\xi = 0.8$)

Figure 3.8: Comparison of coverage probabilities as a function of ζ_A . ((a) $\xi = 0.2$, (b) $\xi = 0.8$)

level so that it remains in HTT mode even when the achieved SINR is low. This reflects that STP is more suitable for use in an interference rich environment.

In Fig. 3.9, we show the coverage probability as a function of backscattering efficiency δ when ζ_A is set at 0.02 and 0.04. As pure HTT is not affected by the backscattering efficiency, the resulting coverage probability remains constant. We

observe that the coverage probability of a pure backscattering transmitter is a monotonically increasing function of the backscattering efficiency. Under PTP, when ζ_A is small (e.g., $\zeta_A = 0.02$), the hybrid transmitter is likely to select either HTT mode or ambient backscattering mode, resulting in a coverage probability between that of pure HTT and that of pure ambient backscattering. When ζ_A is large (e.g., $\zeta_A = 0.04$), the hybrid transmitter has very high chance to stay in HTT mode, and thus results in a coverage probability almost overlapping with that of pure HTT. Under STP, when $\zeta_A = 0.02$, the increase of backscatter efficiency gives the hybrid transmitter more chance to select ambient backscattering mode which has lower coverage probability than that of HTT mode, and therefore, the overall coverage probability of STP decreases. When $\zeta_A = 0.04$, the hybrid transmitter also has larger chance to select ambient backscattering mode as the backscattering efficiency increases. However, in this case, the coverage probability of ambient backscattering mode is significantly improved with higher backscattering efficiency. Thus, the overall coverage probability of STP increases with ζ_A .

In Fig. 3.10, we demonstrate how the coverage probabilities vary with the RF-to-DC conversion efficiency β when ζ_A is set at 0.02 and 0.04. It is straightforward that the coverage probabilities are monotonically increasing functions of β . We can also see that the variations of the coverage probabilities due to the change of β decrease as ζ_A becomes larger. This indicates that higher RF-to-DC conversion efficiency is more beneficial to the coverage probability of the hybrid transmitter when the density of ambient transmitters is small. Additionally, the coverage probability of a pure backscattering transmitter changes very slightly as β varies. This is because the coverage probability is mainly affected by two factors, i.e., energy harvesting rate $P_E^B = \beta \varrho P_I$ and effective backscattered power $P_R = \delta(1 - \varrho)P_I$. Once the en-

energy harvesting rate exceeds the circuit power consumption of a pure backscattering transmitter ρ_B , the effective backscattered power is not impacted by the energy harvesting rate. Due to the fact that ρ_B is very small, the energy harvesting rate reaches ρ_B with a probability approaching 1 at both $\zeta_A = 0.02$ and $\zeta_A = 0.04$. Therefore, the variation of β within a normal range, i.e., from 0.3 to 0.8, does not cause significant change on the coverage probability of a pure backscattering transmitter.

Furthermore, Fig. 3.11 illustrates the comparisons of the coverage probabilities (as functions of transmitter-receiver distance d) under different density of the ambient transmitters ζ_A and interference ratio ξ . We focus on evaluating the scenario with both small ζ_A and ξ and the scenario with both large ζ_A and ξ . In the former scenario (i.e., $\zeta_A = 0.02$ and $\xi = 0.1$) as shown in Fig. 3.11(a), the pure HTT transmitter is inferior to the pure ambient backscatter transmitter when d is small (e.g., $d < 2$). It is because the pure HTT transmitter has a higher chance of energy outage when ζ_A is small. However, the pure HTT transmitter is more robust to longer d since it first aggregates the harvested energy and generates higher transmit power than backscattered power. Moreover, with the increase of d from 0, STP first outperforms PTP by operating in ambient backscattering mode in low ζ_A and is outperformed by PTP when d is larger due to the same reason. Eventually, both achieve comparable performance when d is above a certain value (i.e., around 7 m).

Conversely, in the scenario with larger ζ_A and ξ (i.e., $\zeta_A = 0.04$ and $\xi = 0.6$), as depicted in Fig. 3.11(b), the pure HTT transmitter is superior to the pure ambient backscatter transmitter when d is small (e.g., $d < 6$) because abundant ambient RF resources mitigate the occurrence of energy outage. However, due to severe interference, \mathcal{C}_H (coverage probability of the pure HTT transmitter) plunges with the increase of d . Instead, the pure ambient backscatter transmitter becomes more

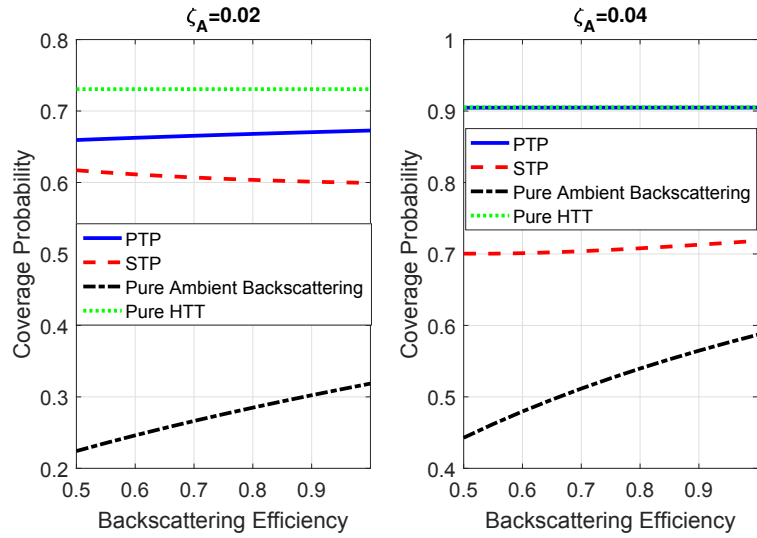


Figure 3.9: Coverage probability as a function of backscattering efficiency.

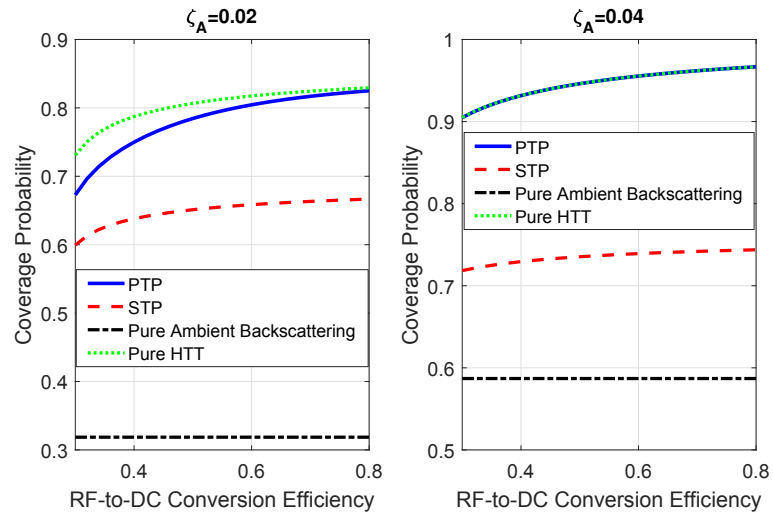
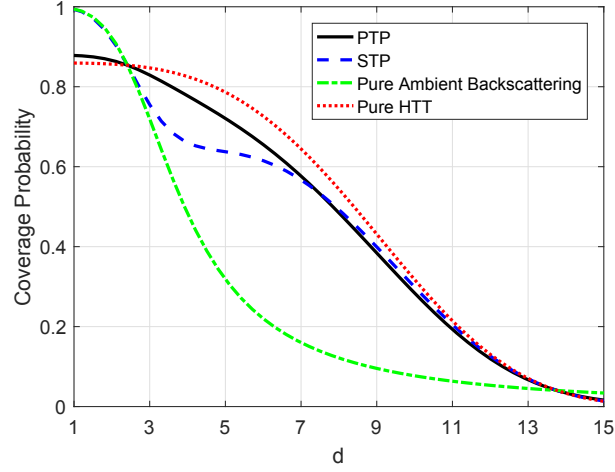


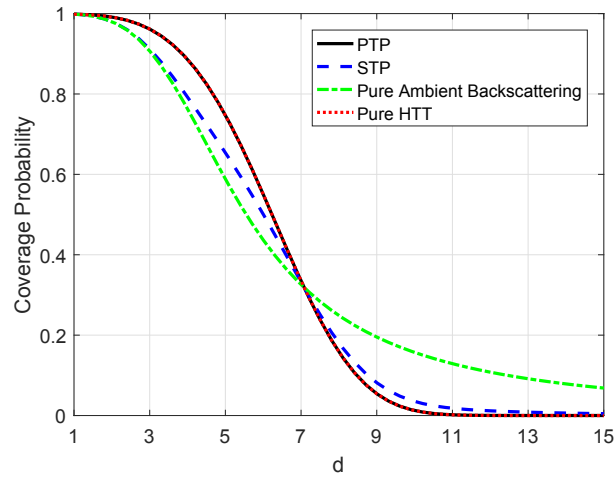
Figure 3.10: Coverage probability as a function of RF-to-DC conversion efficiency.

robust to longer d . It can be seen that \mathcal{C}_{PTP} overlaps with \mathcal{C}_{H} because when the harvested energy is ample the hybrid transmitter always operates in HTT mode. Overall, the performance gap between PTP and STP is small in this scenario.

Fig. 3.12 compares the throughput (as a function of density ζ_A) of PTP, STP, pure



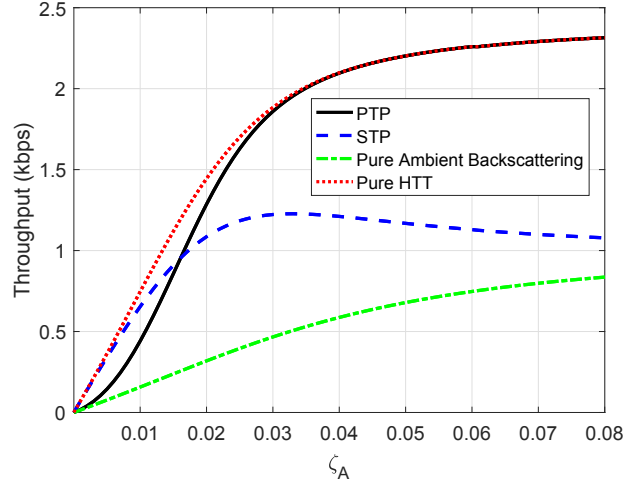
(a)



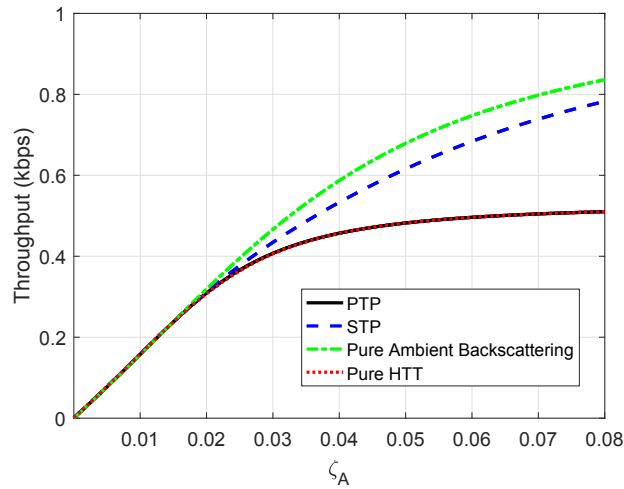
(b)

Figure 3.11: Comparison of coverage probabilities as a function of d . ((a) $\zeta_A = 0.02$, $\xi = 0.1$, (b) $\zeta_A = 0.04$, $\xi = 0.6$)

ambient backscattering, and pure HTT. We focus on the cases when the interference ratio is small ($\xi = 0.2$) and large ($\xi = 0.8$) with the corresponding results shown in Figs. 3.12(a) and 3.12(b), respectively. We observe that the trend of throughput performance has been somehow reflected by the coverage probabilities shown in Fig. 3.8. Similar to our observation for Fig. 3.8, we can draw the conclusion that, in



(a)

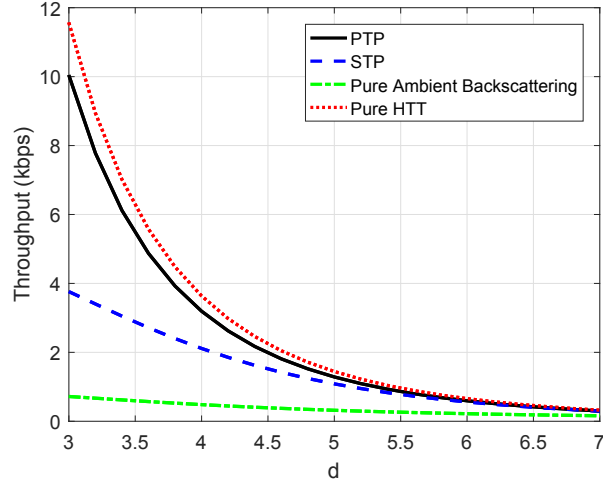


(b)

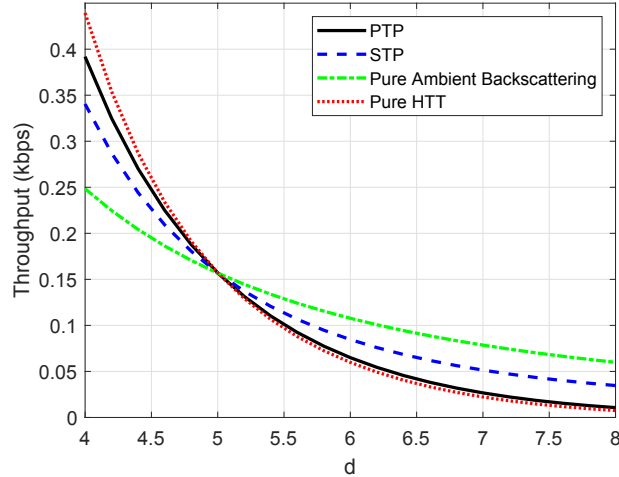
Figure 3.12: Comparison of average throughput as a function of ζ_A . ((a) $d = 5$, $\xi = 0.2$, (b) $d = 5$, $\xi = 0.8$)

general, PTP yields higher throughput when the interference level is low. Otherwise, STP is more suitable for use.

Additionally, Fig. 3.13 examines the influence of transmitter-receiver distance d on the throughput performance. As expected, the pure HTT transmitter prominently outperforms the pure ambient backscatter transmitter with relatively smaller ξ and



(a)



(b)

Figure 3.13: Comparison of average throughput as a function of d . ((a) $\xi = 0.2$, $\zeta_A = 0.02$, (b) $\xi = 0.8$, $\zeta_A = 0.01$)

larger ζ_A (i.e., $\xi = 0.2$ and $\zeta_A = 0.02$) as shown in Fig. 3.13(a). The performance gap becomes progressively significant with decreasing d . PTP also attains remarkable throughput gain over STP since, in this context, energy harvesting rate is a better indication to select HTT mode. By contrast, in the case with relatively larger ξ and smaller ζ_A (i.e., $\xi = 0.8$ and $\zeta_A = 0.01$) as shown in Fig. 3.13(b), PTP is less

advantageous than STP because the energy harvesting rate detection in PTP fails to take into account the increased interference. By contrast, STP becomes superior and exhibits less susceptibility as d grows. The cause is that STP operates more in ambient backscattering mode which is immune to the increased interference.

3.5 Conclusion and Future Work

In this chapter, we have introduced a novel paradigm of hybrid M2M communications that integrate ambient backscattering with wireless-powered communications. To enable the operation of our proposed hybrid transmitter in diverse environments, two simple mode selection protocols, namely PTP and STP, have been devised based on the energy harvesting rate and received SNR of the modulated backscatter, respectively. Under the framework of repulsive point process modeling, we have analyzed the hybrid M2M communications and focused on investigating the impact of environment factors. In particular, the performance of the hybrid M2M communications has been characterized in terms of energy outage probability, coverage probability, and average throughput. The performance analysis has shown that the self-sustainable M2M communications benefit from larger repulsion, transmission load and density of ambient energy sources. Moreover, we have found that PTP is more suitable for use in the scenarios with a large density of ambient energy sources and low interference level. On the contrary, STP becomes favorable in the scenarios when the interference level and density of ambient energy sources are both low or both high. Additionally, PTP appears to be more reliable to yield better throughput for long-range transmission in general.

3.6 Appendix

3.6.1 Proof of Theorem 3.3.1

Proof. The distribution of the aggregated received power at the origin from ambient transmitters can be determined by the calculation of its Laplace transform. Specifically, the Laplace transform of the accumulated incident power at the antenna of the hybrid transmitter can be obtained as

$$\begin{aligned}
\mathcal{L}_{P_I}(s) &= \mathbb{E} [\exp(-sP_I)] \\
&= \mathbb{E} \left[\prod_{a \in \mathcal{A}} \exp \left(-\frac{sP_A h_{a,S}}{\|\mathbf{x}_a - \mathbf{x}_S\|^\mu} \right) \right] \\
&= \mathbb{E} \left[\prod_{a \in \mathcal{A}} M_h \left(-\frac{sP_A}{\|\mathbf{x}_a - \mathbf{x}_S\|^\mu} \right) \right] \\
&= \mathbb{E} \left[\exp \left(\sum_{a \in \mathcal{A}} \ln \left(M_h \left(-\frac{sP_A}{\|\mathbf{x}_a - \mathbf{x}_S\|^\mu} \right) \right) \right) \right] \\
&\stackrel{(i)}{=} \text{Det}(\text{Id} + \alpha \mathbb{A}_\Phi(s))^{-\frac{1}{\alpha}}, \tag{3.21}
\end{aligned}$$

where $M_h(\cdot)$ is the MGF of $h_{a,S}$ and (i) follows by applying Proposition 1, and \mathbb{A}_Φ is

$$\begin{aligned}
\mathbb{A}_\Phi(s) &= \sqrt{1 - M_h(-sP_A \|\mathbf{x} - \mathbf{x}_S\|^{-\mu})} \\
&\quad \times G_\Phi(\mathbf{x}, \mathbf{y}) \sqrt{1 - M_h(-sP_A \|\mathbf{y} - \mathbf{x}_S\|^{-\mu})}, \tag{3.22}
\end{aligned}$$

where G_Φ is the Ginibre kernel given in (2.5). Since $h \sim \mathcal{G}(m, \frac{\theta}{m})$, the MGF of a Gamma random variable h can be calculated as $M_h(z) = (1 - \frac{\theta z}{m})^{-m}$. Therefore, we

have

$$M_h(-sP_A\|\mathbf{x} - \mathbf{x}_S\|^{-\mu}) = \left(1 + \frac{s\theta P_A}{m\|\mathbf{x} - \mathbf{x}_S\|^\mu}\right)^{-m}. \quad (3.23)$$

Inserting (3.23) in (3.22) gives the expression in (3.8).

Given the Laplace transforms of P_I , by definition, the PDF of P_I is attained by taking the inverse Laplace transform as follows:

$$\begin{aligned} f_{P_I}(\rho) &= \mathcal{L}^{-1}\{\mathcal{L}_{P_I}(s)\}(\rho) \\ &= \mathcal{L}^{-1}\left\{\text{Det}(\text{Id} + \alpha\mathbb{A}_\Phi(s))^{-\frac{1}{\alpha}}\right\}(\rho), \end{aligned} \quad (3.24)$$

with $\mathbb{A}_\Phi(s)$ given in (3.8).

Furthermore, integrating PDF in (3.24) yields

$$\begin{aligned} F_{P_I}(\rho) &= \int_{-\infty}^{\rho} \mathcal{L}^{-1}\{\mathcal{L}_{P_I}(s)\}(t)dt \\ &= \mathcal{L}^{-1}\left\{\frac{\mathcal{L}_{P_I}(s)}{s}\right\}(\rho) \\ &= \mathcal{L}^{-1}\left\{\frac{\text{Det}(\text{Id} + \alpha\mathbb{A}_\Phi(s))^{-\frac{1}{\alpha}}}{s}\right\}(\rho). \end{aligned} \quad (3.25)$$

When the hybrid transmitter is working in ambient backscattering mode, one can obtain the Laplace transform $\mathcal{L}_{P_E^B}(s)$ as

$$\mathcal{L}_{P_E^B}(s) = \mathbb{E}[\exp(-s\beta\rho P_I)] = \mathcal{L}_{P_I}(s\beta\rho). \quad (3.26)$$

Consequently, we can obtain the energy outage probability in ambient backscattering mode \mathcal{O}_B , or equivalently, the CDF of P_E^B evaluated at ρ_B , by integrating the

PDF obtained in (3.26) as

$$\begin{aligned}\mathcal{O}_B &= F_{P_E^B}(\rho_B) = F_{P_I} \left(\frac{\rho_B}{\beta \varrho} \right) \\ &= \mathcal{L}^{-1} \left\{ \frac{\text{Det}(\text{Id} + \alpha \mathbb{A}_\Phi(s))^{-\frac{1}{\alpha}}}{s} \right\} \left(\frac{\rho_B}{\beta \varrho} \right).\end{aligned}\quad (3.27)$$

Similarly, one obtains the energy outage probability in HTT mode \mathcal{O}_H , or equivalently the CDF of P_E^H evaluated at ρ_H , as

$$\begin{aligned}\mathcal{O}_H &= F_{P_E^H}(\rho_H) = F_{P_I} \left(\frac{\rho_H}{\omega \beta} \right) \\ &= \mathcal{L}^{-1} \left\{ \frac{\text{Det}(\text{Id} + \alpha \mathbb{A}_\Phi(s))^{-\frac{1}{\alpha}}}{s} \right\} \left(\frac{\rho_H}{\omega \beta} \right).\end{aligned}\quad (3.28)$$

Let \mathcal{B}_{PTP} denote the probability that the hybrid transmitter operated by PTP is in ambient backscattering mode. According to the criteria of PTP, from the definition in (3.3), we have

$$\mathcal{O}_{\text{PTP}} = \mathcal{B}_{\text{PTP}} \mathcal{O}_B + (1 - \mathcal{B}_{\text{PTP}}) \mathcal{O}_H \quad (3.29)$$

$$= \mathbb{P} \left[P_I \leq \frac{\rho_H}{\omega \beta} \right] F_{P_I} \left(\frac{\rho_B}{\beta \varrho} \right) + \left(1 - \mathbb{P} \left[P_I \leq \frac{\rho_H}{\omega \beta} \right] \right) F_{P_I} \left(\frac{\rho_H}{\omega \beta} \right). \quad (3.30)$$

One notices that \mathcal{B}_{PTP} is equal to the CDF of P_I evaluated at $\frac{\rho_H}{\omega \beta}$, which is expressed as

$$\begin{aligned}\mathcal{B}_{\text{PTP}} &= F_{P_I} \left(\frac{\rho_H}{\omega \beta} \right) \\ &= \mathcal{L}^{-1} \left\{ \frac{\text{Det}(\text{Id} + \alpha \mathbb{A}_\Phi(s))^{-\frac{1}{\alpha}}}{s} \right\} \left(\frac{\rho_H}{\omega \beta} \right).\end{aligned}\quad (3.31)$$

Then, by inserting (4.5), (3.28) and (3.31) in (3.30), we obtain \mathcal{O}_{PTP} in (3.6). ■

3.6.2 Proof of Theorem 3.3.2

Proof. According to the criteria of STP, we have the probability of being in ambient backscattering mode as

$$\begin{aligned}
\mathcal{B}_{\text{STP}} &\triangleq \mathbb{P}[\nu_{\text{B}} > \tau_{\text{B}}, P_{\text{E}}^{\text{B}} > \rho_{\text{B}}] & (3.32) \\
&= \mathbb{P}\left[\frac{\delta P_{\text{I}} h_{\text{S,D}}}{d^{\mu} \sigma^2} (1 - \varrho) > \tau_{\text{B}}, P_{\text{E}}^{\text{B}} > \rho_{\text{B}}\right] \\
&= \mathbb{P}\left[h_{\text{S,D}} > \frac{\tau_{\text{B}} d^{\mu} \sigma^2}{\delta P_{\text{I}} (1 - \varrho)}, P_{\text{I}} \beta \varrho > \rho_{\text{B}}\right] \\
&\stackrel{\text{(a)}}{=} \mathbb{P}\left[h_{\text{S,D}} > \frac{\tau_{\text{B}} d^{\mu} \sigma^2}{\delta P_{\text{I}} (1 - \varrho)} \middle| P_{\text{I}} > \frac{\rho_{\text{B}}}{\beta \varrho}\right] \mathbb{P}\left[P_{\text{I}} > \frac{\rho_{\text{B}}}{\beta \varrho}\right] \\
&= \mathbb{E}_{P_{\text{I}}}\left[\mathbb{P}\left[h_{\text{S,D}} > \frac{\tau_{\text{B}} d^{\mu} \sigma^2}{\delta P_{\text{I}} (1 - \varrho)} \middle| P_{\text{I}}\right] \mathbb{1}_{\{P_{\text{I}} > \frac{\rho_{\text{B}}}{\beta \varrho}\}}\right] \\
&= \int_{\frac{\rho_{\text{B}}}{\beta \varrho}}^{\infty} \exp\left(-\frac{\lambda \tau_{\text{B}} d^{\mu} \sigma^2}{\delta \rho (1 - \varrho)}\right) f_{P_{\text{I}}}(\rho) d\rho, & (3.33)
\end{aligned}$$

where (a) follows by the Bayes' theorem [89, page 36], and $\mathbb{1}_{\{\text{E}\}}$ is an indicator function that takes the value of 1 if event E happens, and takes the value of 0 otherwise.

Then, by replacing \mathcal{B}_{PTP} in the expression of (3.29) with \mathcal{B}_{STP} shown as (3.33), we have (3.10) in **Theorem 3.3.2** after some mathematical manipulations. ■

3.6.3 Proof of Corollary 3

Proof. When there exists no repulsion, the GPP becomes a PPP with α approaching zero. By using the expansion [57]

$$\text{Det}(\text{Id} + \alpha \mathbb{A}_\Phi(s))^{-\frac{1}{\alpha}} \xrightarrow{\alpha \rightarrow 0} \exp\left(-\int_{\mathbb{O}_S} \mathbb{A}_\Phi(\mathbf{x}, \mathbf{x}) d\mathbf{x}\right), \quad (3.34)$$

we can simplify (3.24) as follows when $h_{a,S} \sim \mathcal{E}(1)$ and $\mu = 4$.

$$\begin{aligned} f_{P_I}(\rho) &= \mathcal{L}^{-1}\left\{\exp\left(-2\pi\zeta_A \int_0^{R \rightarrow \infty} \frac{r}{1+r^4(sP_A)^{-1}} dr\right)\right\}(\rho) \\ &= \mathcal{L}^{-1}\left\{\frac{1}{s} \exp\left(-\frac{\pi^2\zeta_A\sqrt{sP_A}}{2}\right)\right\}(\rho) \\ &\stackrel{\text{(ii)}}{=} \frac{1}{2\pi i} \lim_{T \rightarrow \infty} \int_{z-iT}^{z+iT} \exp\left(\rho s - \frac{\pi^2\zeta_A\sqrt{sP_A}}{2}\right) ds \\ &\stackrel{\text{(iii)}}{=} \frac{1}{2\pi i} \int_0^\infty \exp(-\rho t) \left[\exp\left(\frac{\pi^2\zeta_A\sqrt{-tP_A}}{2}\right) - \exp\left(-\frac{\pi^2\zeta_A\sqrt{-tP_A}}{2}\right) \right] dt \\ &\stackrel{\text{(iv)}}{=} \frac{1}{\pi} \int_0^\infty \exp\left(-\rho \frac{4u^2}{\pi^4\zeta_A^2 P_A}\right) \sin(u) \frac{8u}{\pi^4\zeta_A^2 P_A} du \\ &\stackrel{\text{(v)}}{=} \frac{1}{4} \left(\frac{\pi}{\rho}\right)^{\frac{3}{2}} \zeta_A \sqrt{P_A} \exp\left(-\frac{\pi^4\zeta_A^2 P_A}{16\rho}\right), \end{aligned}$$

where (ii) follows Mellin's inverse formula [90] which transforms the inverse Laplace transform into the complex plane, i is the imaginary unit, i.e., $i = \sqrt{-1}$, and z is a fixed constant greater than the real parts of the singularities of $\exp\left(-\frac{\pi^2\zeta_A\sqrt{sP_A}}{2}\right)$, (iii) applies the Bromwich inversion theorem with the modified contour [91, Chapter 2], (iv) applies Euler's formula [92, Page 1035] and a replacement of $u = \frac{\pi^2\zeta_A\sqrt{tP_A}}{2}$, and (v) uses the method of integration by parts.

Furthermore, based on the $f_{P_I}(\rho)$ expression, the CDF $F_{P_I}(\rho)$ in (3.12) can be obtained after some mathematical manipulations. ■

3.6.4 Proof of Theorem 3.3.3

Proof. We first determine the coverage probability in ambient backscattering mode. One simply notes that the expression of \mathcal{C}_B in (3.4) is equivalent to the definition of \mathcal{B}_{STP} in (3.32). Hence, we have

$$\mathcal{C}_B = \int_{\frac{\rho_B}{\beta\varrho}}^{\infty} \exp\left(-\frac{\lambda\tau_B d^\mu \sigma^2}{\delta\rho(1-\varrho)}\right) f_{P_I}(\rho) d\rho. \quad (3.35)$$

Let $Q = \xi \sum_{b \in \mathcal{B}} P_B \tilde{h}_{b,D} \|\mathbf{x}_b - \mathbf{x}_D\|^{-\mu}$ denote the aggregated interference at the receiver. We then derive the coverage probability in HTT mode as

$$\begin{aligned} \mathcal{C}_H &= \mathbb{P}[\nu_H > \tau_H, P_E^H > \rho_H] \\ &= \mathbb{E}_{P_I} \left[\mathbb{P} \left[\tilde{h}_{S,D} > \frac{\tau_H d^\mu (1-\omega)(Q + \sigma^2)}{\omega\beta P_I - \rho_H} \middle| P_I \right] \mathbb{1}_{\{P_I > \frac{\rho_H}{\beta\omega}\}} \right] \\ &= \mathbb{E}_{P_I} \left[\exp\left(-\frac{\lambda\tau_H d^\mu \sigma^2 (1-\omega)}{\omega\beta P_I - \rho_H}\right) \mathbb{E} \left[\exp\left(-\frac{\lambda\tau_H d^\mu (1-\omega)}{\omega\beta P_I - \rho_H} \right. \right. \right. \\ &\quad \left. \left. \left. \times \xi \sum_{b \in \mathcal{B}} P_B \tilde{h}_{b,D} \|\mathbf{x}_b - \mathbf{x}_D\|^{-\mu} \right) \right] \mathbb{1}_{\{P_I > \frac{\rho_H}{\beta\omega}\}} \right] \\ &\stackrel{(vi)}{=} \int_{\frac{\rho_H}{\beta\omega}}^{\infty} \exp\left(-\frac{\lambda\tau_H d^\mu \sigma^2 (1-\omega)}{\omega\beta\rho - \rho_H}\right) \text{Det}(\text{Id} + \alpha\mathbb{B}_\Psi(\rho))^{-\frac{1}{\alpha}} f_{P_I}(\rho) d\rho, \end{aligned} \quad (3.36)$$

where (vi) is given following Proposition 1, and $\mathbb{B}_\Psi(\rho)$ is defined in (3.15).

By definition in (3.4), the coverage probability under PTP can be written as

$$\mathcal{C}_{\text{PTP}} = \mathcal{B}_{\text{PTP}} \mathcal{C}_B + (1 - \mathcal{B}_{\text{PTP}}) \mathcal{C}_H. \quad (3.37)$$

Then, by plugging \mathcal{B}_{PTP} shown as (3.31), \mathcal{C}_B shown as (3.35) and \mathcal{C}_H shown as (3.36) into (3.37), we have (3.14). ■

3.6.5 Proof of Theorem 3.3.5

Proof. The average throughput in ambient backscattering mode \mathcal{T}_B can be calculated as

$$\begin{aligned}\mathcal{T}_B &= \mathbb{E}[T_B \mathbb{1}_{\{\nu_B > \tau_B, P_E^B > \rho_B\}}] \\ &= T_B \mathbb{P}[\nu_B > \tau_B, P_E^B > \rho_B] = T_B \mathcal{C}_B,\end{aligned}\tag{3.38}$$

where T_B has been defined in Subsection 4.2 and \mathcal{C}_B has been obtained in (3.35).

Moreover, the average throughput in HTT mode can be computed as

$$\begin{aligned}\mathcal{T}_H &= \mathbb{E}[(1 - \omega)W \log_2(1 + \nu_H) \mathbb{1}_{\{\nu_H > \tau_H, P_E^H > \rho_H\}}] \\ &\stackrel{\text{(vii)}}{=} (1 - \omega)W \mathbb{E} \left[\int_0^\infty \mathbb{P}[\log_2(1 + \nu_H) > t] dt \mathbb{1}_{\{\nu_H > \tau_H, P_E^H > \rho_H\}} \right] \\ &= (1 - \omega)W \int_{\log_2(1 + \tau_H)}^\infty \mathbb{E}_{P_I} \left[\exp \left(-\frac{\lambda d^\mu (1 - \omega) (2^t - 1)}{\omega \beta P_I - \rho_H} \right) \right. \\ &\quad \left. \times \left(\sigma^2 + \xi \sum_{b \in \mathcal{B}} P_B \tilde{h}_{b,D} \|\mathbf{x}_b - \mathbf{x}_D\|^{-\mu} \right) \mathbb{1}_{\{P_I > \frac{\rho_H}{\beta \omega}\}} \right] dt \\ &\stackrel{\text{(viii)}}{=} (1 - \omega)W \int_{\log_2(1 + \tau_H)}^\infty \int_{\frac{\rho_H}{\beta \omega}}^\infty \exp \left(-\frac{\lambda d^\mu \sigma^2 (1 - \omega) (2^t - 1)}{\omega \beta \rho - \rho_H} \right) \\ &\quad \times \text{Det}(\text{Id} + \alpha \mathbf{C}_\Psi(\rho))^{-\frac{1}{\alpha}} f_{P_I}(\rho) d\rho dt,\end{aligned}\tag{3.39}$$

where (vii) follows $\mathbb{E}[X] = \int_0^\infty \mathbb{P}[X > x] dx$ [52], (viii) is derived by applying Proposition 1, and $\mathbf{C}_\Psi(\rho)$ is defined in (3.19).

By definition in (3.5), the average throughput under PTP can be written as

$$\mathcal{T}_{\text{PTP}} = \mathcal{B}_{\text{PTP}} T_B \mathcal{C}_B + (1 - \mathcal{B}_{\text{PTP}}) \mathcal{T}_H.\tag{3.40}$$

Inserting \mathcal{B}_{PTP} shown as (3.31), \mathcal{C}_{B} shown as (3.35), and \mathcal{T}_{H} shown as (3.39) into (3.40) yields (3.18). ■

Chapter 4

Ambient Backscatter-Assisted Wireless-Powered Relaying

This Chapter¹ aims to proposed new solutions to improve the connectivity of MTC.

4.1 Related Works

There are limited research efforts in the literature on wireless-powered communications enhanced with ambient backscattering. Reference [88] investigated a cognitive radio network where the wireless-powered secondary user is equipped with ambient backscattering capability. In this network, when the primary user is on transmission, the secondary user can select to perform energy harvesting or ambient backscattering. When the primary user is off, the secondary user can perform active transmission with the harvested energy. Optimal transmission policies are designed to maximize

¹A version of this chapter has been published in the IEEE Transactions on Green Communications and Networking [93] and also in part in the Proceedings of IEEE International Conference on Communications [94].

the throughput of the secondary network. Based on the system model in [88], the authors in [95] formulated optimal resource allocation problems to maximize the sum throughput of the secondary users. Moreover, the authors in [96] extended the system model in [88] to a large scale and characterized the coverage probability and throughput for both primary users and secondary users based on stochastic geometry analysis. Additionally, our work in the previous chapter of this dissertation investigated an integrated wireless-powered transmitter with ambient backscattering for M2M communication. It was shown that ambient backscattering is suitable to work as an alternative to wireless-powered transmission when the ambient energy is not sufficient and or when the interference level is high. To further exploit the benefits of wireless-powered communications with ambient backscattering for extending the communication range, we investigate this hybrid communication paradigm for cooperative relaying. To the best of our knowledge, this is the first time that the integration of wireless-powered transmission and ambient backscattering is proposed for cooperative IoT networks, to enhance the applicability and performance.

4.2 System Model and Stochastic Geometry Characterization

This section introduces the system model under consideration and then describes some preliminary results of the adopted stochastic geometry framework.

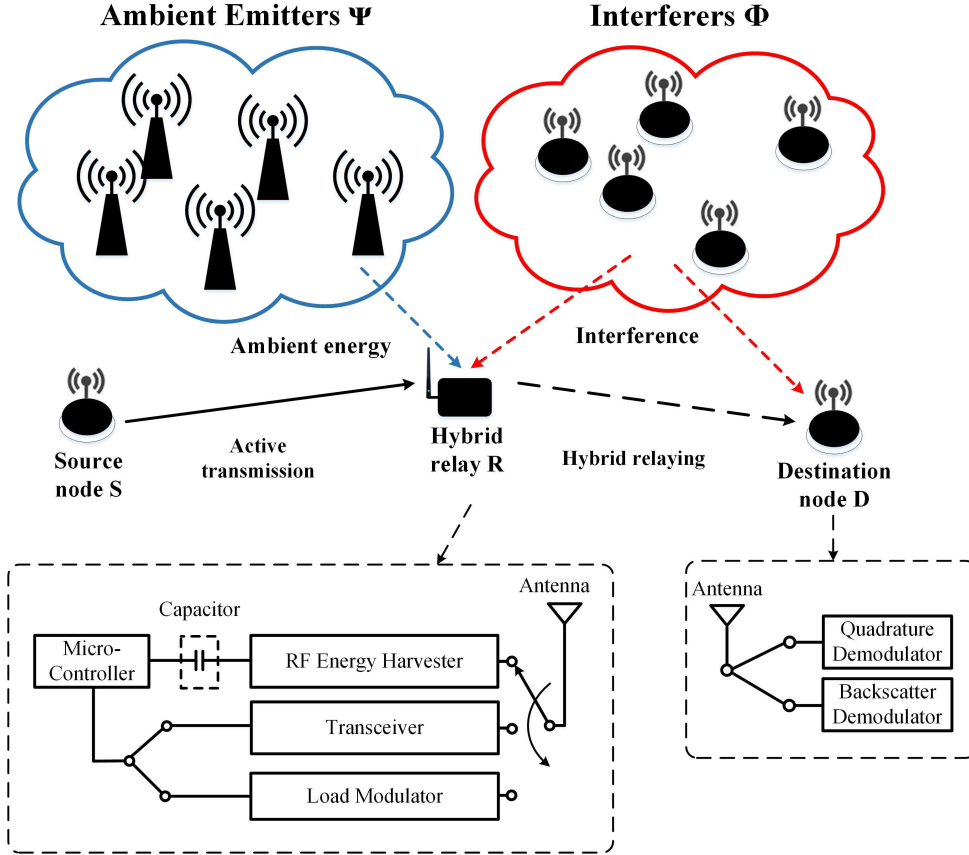


Figure 4.1: A dual-hop relaying system in an α -GPP field of ambient emitters and interferers.

4.2.1 System and Relaying Protocol

As shown in Fig. 4.1, the system model contains a source node S that needs to transmit to a destination node D. However, there exists no direct link between S and D, e.g., due to obstacles/shadowing or severe path loss. Similar to [97, 98], we only consider the scenario where the information from S to D is forwarded through the relay node R to focus on investigating the relaying performance. R is composed of both an active transceiver and an ambient backscatter transmitter so that it can perform either wireless-powered relaying (WPR) or ambient backscatter relaying (ABR). Accordingly, D is equipped with both a quadrature demodulator and

backscatter demodulator to decode the information from R. All three nodes S, R, and D are equipped with a single antenna and work in a half-duplex fashion. Similar to the system models in [30,99], both S and D are assumed to have sufficient energy, e.g., from its internal battery, to supply their operations. Thus, the focus is on R which is equipped with an energy harvester and an onboard capacitor with capacity E_C to store the harvested energy for the relaying operation. Similar to [100,101], we consider that R adopts the *harvest-use* architecture, with which the harvested energy is either consumed immediately or lost, e.g., due to hardware limitations such as high leakage of the capacitor. This implies that no harvested energy is accumulated for the subsequent time slot. We leave the case with energy accumulation for future work.

As shown in the left block diagram in Fig. 4.1, a time switching-based receiver architecture [60] is adopted to enable R to work in either energy harvesting, information decoding or transmission. R performs energy harvesting/ambient backscattering and active transmission on two different frequency bands. For example, the hybrid relay can be designed to harvest energy and perform ambient backscattering by using the downlink signals of ambient BSs while the hybrid relay can actively transmit data on the operating frequency of the source node S. Let Ψ and Φ denote the point processes, i.e., the sets, of ambient emitters and the interferers, respectively. The ambient emitters are the surrounding transmitters working on the frequency band that the hybrid relay performs energy harvesting/ambient backscattering². The interferers are the surrounding low-power transmitters, e.g., sensors, working on the frequency band that the hybrid relay performs active transmission. We assume that

²As the interferers are considered to be low-power devices, the transmit power of the interferers are much lower than that of the carrier emitters. Therefore, we do not consider complex multi-band rectifier design at the hybrid relay to additionally harvest energy from the interferers.

during any time slot the distributions of Ψ and Φ follow independent homogeneous α -GPPs³. As during each time slot the source-to-relay and relay-to-destination transmissions are considered to be affected by the same set of interferers, our analytical framework is suitable to model relaying systems with no or low mobility where the locations of ambient transmitters relatively remain static during each transmission. Let $\tilde{\zeta}(\zeta)$, $\tilde{\alpha}(\alpha)$, and $\tilde{P}_T(P_T)$ denote the spatial density, repulsion factor, and transmit power of the transmitters in Ψ (Φ), respectively⁴. The system model in Fig. 4.1 is expected to find its applications in various IoT scenarios featured with low traffic volume and data rate, such as wireless sensor networks, body area networks and M2M communication networks, where the source and interferers are energy-constrained IoT devices that have communication demand. The source node relies on the hybrid relay which utilizes the resources from ambient emitters (e.g., BSs and Wi-Fi access points) to enhance the communication performance (e.g., connectivity and transmission range).

Fig. 4.2 shows the time slots of the relaying protocol adopted by the considered hybrid relaying system to coordinate among energy harvesting and the dual-hop relaying. Let T denote the duration of a time slot. At the beginning of each time slot, an ω ($0 < \omega < 1$) fraction of T is allocated for R to harvest ambient energy. Then, the first half and second half of the remaining time (i.e., each with duration $\frac{(1-\omega)T}{2}$) are allocated for the source-to-relay transmission and relay-to-destination transmission, respectively. During the relay-to-destination transmission, R operates in either the WPR mode or the ABR mode, denoted as W and A⁵, respectively, based on the

³The mathematical details about α -GPP can be found in [56, 102].

⁴We use $\tilde{(\cdot)}$ to denote notations related to ambient emitters Ψ and their frequency band. We do not have tilde for notations related to the interferers Φ and their frequency band.

⁵W and A appear in the subscripts and superscripts of variables to represent the operation mode.

system environment. The mode selection is performed by the hybrid relay and the proposed mode selection protocols are to be introduced in Sec. 4.3. Once the mode selection is complete, R indicates the selected mode to D through signaling and D is tuned to the corresponding receiver for signal decoding. If the WPR mode is chosen, R first decodes the active transmission from S in the source-to-relay transmission phase and adopts the decode-and-forward protocol for relaying the data from S to D in the relay-to-destination transmission phase⁶. If the ABR mode is chosen, R also first decodes the active transmission from S in the source-to-relay transmission phase, but forwards the decoded message to D through ambient backscattering. The source node can work as the controller to coordinate the transmissions of the relaying system. For example, S can maintain a clock and send control signals to schedule the operation of the hybrid relaying system according to the relaying protocol shown in Fig. 4.2. The control signal for the relay node can be received directly, and that for the destination node can be forwarded by the relay node. The synchronization between the source and relay nodes and that between the relay and destination nodes can be achieved through a correlation-based timing estimator [103, 104]. Similar to [99] and [30], we consider no timing synchronization errors among S, R and D.

In the WPR and ABR mode, denote E_W and E_A , respectively, as the circuit energy consumption over the whole time slot plus the energy consumption for decoding information in the source-to-relay transmission phase. We have $E_A < E_W < E_C$, with E_C being the capacitor capacity of R. The hybrid relay is able to function in the WPR mode and ABR mode only if the harvested energy during the energy harvesting phase of each time slot E_R exceeds E_W and E_A , respectively.

⁶Our analytical framework can be straightforwardly extended to the case when the amplify-and-forward protocol is adopted in WPR mode. The relaying protocols shown in Fig. 4.2 directly applies.

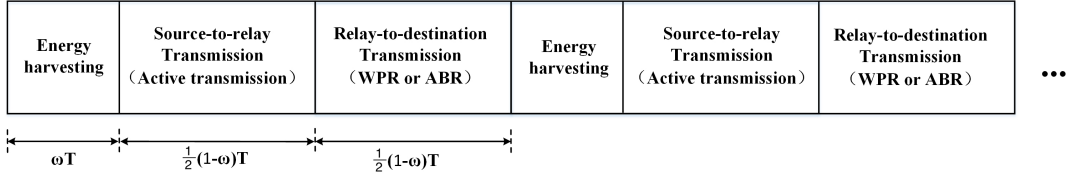


Figure 4.2: A time-slot based relaying protocol.

4.2.2 Channel Model

We consider the quasi-static interference scenario [105] where the interferers Φ remain static within each time-slot and vary across different time slots. All the channels in the systems are considered to experience independent and identically distributed (i.i.d.) block Rayleigh fading. In particular, the fading channel gains follow exponential distributions. Besides, we consider i.i.d. zero-mean AWGN with variance $\tilde{\sigma}^2$ and σ^2 on the transmit frequency of Ψ and Φ , respectively.

Harvested Energy

The hybrid relay harvests energy from the ambient emitters in Ψ for its operation. The power of the RF signals from Ψ received by the hybrid relay can be computed as $Q_R = \tilde{P}_T \sum_{\mathbf{x}_k \in \Psi} \tilde{h}_{k,R} \|\mathbf{x}_k - \mathbf{x}_R\|^{-\tilde{\mu}}$, where $\tilde{h}_{a,b} \sim \mathcal{E}(1)$ is the fading channel gain between nodes a and b on the transmit frequency of Ψ , and $\tilde{\mu}$ represents the path-loss exponent for the signals from the ambient emitters in Ψ . Then, the instantaneous energy harvesting rate (in Watt) at the hybrid relay can be expressed as $\rho_R = \beta Q_R$, where $\beta \in (0, 1]$ denotes the RF-to-DC conversion efficiency. And the amount of energy harvested during the energy harvesting phase is obtained as $E_R = \omega T \rho_R$.

Source-to-Relay Transmission

During the source-to-relay transmission phase, the receive signal-to-interference-plus-noise ratio (SINR) at the relay node R is given by $\nu_R = \frac{P_S h_{S,R} d_{S,R}^{-\mu}}{I_R + \sigma^2}$, where P_S is the transmit power of the source node, $h_{a,b} \sim \mathcal{E}(1)$ denotes the fading channel gain between a and b on the transmit frequency of Φ , $d_{x,y}$ represents the distance between x and y , μ is the path-loss exponent for signals from the interferers Φ , S and R, $I_R = \sum_{j \in \Phi} P_T h_{j,R} \|\mathbf{x}_j - \mathbf{x}_R\|^{-\mu}$ is the aggregated interference received at R.

Relay-to-Destination Transmission

Let $\rho_W = \frac{E_W}{T}$ and $\rho_A = \frac{E_A}{T}$ denote the average circuit power consumption rate of R in the WPR mode and the ABR mode, respectively, and $\rho_C \triangleq \frac{E_C}{T}$ denotes the normalized energy capacity over a time slot duration. Moreover, let us define $\varrho_W \triangleq \frac{\rho_W}{\omega\beta}$, $\varrho_A \triangleq \frac{\rho_A}{\omega\beta}$ and $\varrho_C \triangleq \frac{\rho_C}{\omega\beta}$.

If the WPR mode is chosen, R uses all the available energy for active transmission during the relay-to-destination transmission phase. Then, the transmit power can be calculated as

$$P_R^W = \begin{cases} 0 & \text{if } Q_R \leq \varrho_W, \\ \frac{T\omega\beta Q_R - E_W}{\frac{T(1-\omega)}{2}} = \frac{2(\omega\beta Q_R - \rho_W)}{1-\omega} & \text{if } \varrho_W < Q_R \leq \varrho_C, \\ \frac{E_C - E_W}{\frac{T(1-\omega)}{2}} = \frac{2(\rho_C - \rho_W)}{1-\omega} & \text{otherwise.} \end{cases} \quad (4.1)$$

Correspondingly, the receive SINR at D is $\nu_D^W = \frac{P_R^W h_{R,D} d_{R,D}^{-\mu}}{I_D + \sigma^2}$, where $I_D = \sum_{j \in \Phi} P_T h_{j,D} \|\mathbf{x}_j - \mathbf{x}_D\|^{-\mu}$ is the aggregated interference received at D.

Then, the end-to-end capacity achieved in WPR mode can be computed as

$$C_W = \begin{cases} \frac{(1-\omega)}{2} W \log_2 (1 + \nu) & \text{if } \nu \geq \tau_W, \\ 0 & \text{otherwise,} \end{cases} \quad (4.2)$$

where W denotes the transmission bandwidth of R in the WPR mode, ν represents the end-to-end SINR calculated as [106] $\nu = \min(\nu_R, \nu_D^W)$, and τ_W is the target SINR threshold for active transmission at R and D.

Otherwise, if R decides to forward data through ambient backscattering, the transmit power of modulated backscatter can be calculated as [76]

$$P_R^A = \eta \xi Q_R, \quad (4.3)$$

where η is the fraction of the incoming RF signals reflected during backscattering and $\xi \in (0, 1]$ is the backscattering efficiency of the transmit antenna. ξ represents the portion of the reflected signals that are effectively used to carry the modulated data. The values of η and ξ are dependent on the tag-encoding scheme [75] and tag antenna aperture [107], respectively.

We consider that *frequency shifting* [108] is adopted by the hybrid relay to transform the backscattered signals to another frequency that does not overlap with that of the signals from the carrier emitters ⁷. Then, the backscattered signals will be exempt from the interference from the carrier emitters. Consequently, the SNR from ambient backscatter at D is expressed as $\nu_D^A = \frac{P_R^A \tilde{h}_{R,D} d_{R,D}^{-\mu}}{\bar{\sigma}^2}$.

For ambient backscattering, due to the adopted simple amplitude demodulation

⁷Frequency shifting, for example, can be achieved by toggling the RF transistor of an ambient backscatter transmitter at a different speed [109]

based on envelope detection [26], the Shannon capacity expression cannot be used to calculate the channel capacity. Following the experimental results of the hardware design in [26], we consider an empirical backscatter capacity model for the relay-to-destination link, i.e., a fixed channel capacity $C_A > 0$ predefined by the hardware configuration of the ambient backscatter transmitter or zero channel capacity can be achieved once the receive SNR at D is above or below a threshold τ_A , respectively. A similar backscatter channel capacity mode has also been adopted in the references [88, 95]. The value of C_A is dependent on the encoding scheme adopted and the setting of the resistor-capacitor of the ambient backscattering circuit [26, 88]. An ambient backscatter receiver typically requires much higher receive SNR to achieve a low bit error rate compared with a quadrature demodulator [110]. For example, a bit error rate of around 10^{-3} can be obtained with 10 dB receive SNR [111]. We refer to [24, 26] for more physical layer details of ambient backscattering. As ambient backscattering usually adopts very simple modulation schemes with small constellations, such as amplitude shift keying and binary phase shift keying, it is reasonable to consider that $C_A < C_W$. Therefore, when the hybrid relay is in ABR mode, the end-to-end capacity becomes C_A if the dual-hop transmission is successful.

Table 4.1 summarizes the main notations used in this chapter.

4.2.3 Operation Model Selection Protocols

The advantage of the hybrid relay lies in the fact that it can select the more suitable operational mode to achieve better performance under different network conditions. However, as the hybrid relay is a wireless-powered device, any mode selection protocols that have large computational complexity, e.g., based on online optimizations, are not applicable. For implementation practicality, low complexity mode selection

Table 4.1: NOTATIONS.

Symbol	Definition
Ψ, Φ	The point processes representing the ambient emitters and interferers, respectively
S, R, D	The source node, hybrid relay, and destination node
$\tilde{\alpha}, \alpha$	Repulsion factors for Ψ and Φ , respectively
\tilde{P}_T, P_T	The transmit power of the transmitters in Ψ and Φ , respectively
$\tilde{\mu}, \mu$	Pass-loss exponent for the signals from Ψ and Φ , respectively
P_S	The transmit power of the source node S
E_A, E_B	The circuit power consumption of the hybrid relay in a time slot with wireless-powered relaying and ambient backscatter relaying, respectively
$\tilde{\sigma}^2, \sigma^2$	The variance of AWGN in the transmit frequency of the transmitters in Ψ and Φ , respectively
E_R	The amount of harvested energy at the hybrid relay R
E_C	The capacitor capacity of R
W	The channel bandwidth for the hybrid relaying system
ξ	Backscattering efficiency
β	The RF-to-DC conversion efficiency
ω	Fraction of time used by R for energy harvesting
ν_D^W, ν_D^A	The receive SINR and SNR at D from the active transmission and ambient backscatter, respectively
τ_W, τ_A	The SINR threshold to decode from the active transmission and ambient backscatter, respectively

based on available information and limited communication overhead needs to be devised. For the mode selection of the hybrid relay, we consider the situations with and without instantaneous CSI of active transmission. For the former and the latter situations, we propose two protocols, namely, *energy and SINR-aware protocol* (ESAP) and *explore-then-commit protocol* (ETCP), respectively, for the hybrid relay adapting to the network environment. The operational procedures of the mode selection protocols are described in the following.

- ESAP: At the beginning of each time slot, S first sends preamble signals to R and R detects its instantaneous energy harvesting rate ρ_R . If the instantaneous energy harvesting rate $\rho_R > \rho_W$, R first detects the receive SINR ν_R . If $\tau_R > \tau_W$ then R transmits preambles to D through active transmission with transmit power $P_R^W = \left[\frac{2(\rho_R - \rho_W)}{1 - \omega}, \frac{2\rho_C}{1 - \omega} \right]^+$. Then, D provides feedback of its receive SINR to R through signaling. If the receive SINR at D is greater than τ_W , R chooses the WPR mode for relaying and D works with the quadrature demodulator. Otherwise, R chooses ABR mode for relaying and D uses the backscatter demodulator. For ESAP, we consider the ideal case that the detection at the beginning of each time slot causes negligible time compared to the duration of a time slot.
- ETCP: ECTP begins with an exploration period that occupies the first initial $2n$ ($n \in \mathbb{N}^+$) time slots to learn the network conditions before committing to a certain operation mode for steady-state transmission based on the learned knowledge. Specifically, in the exploration period, R works in each operational mode for n times in an arbitrary sequence. Afterward, D feeds back the numbers of successful transmissions in the WPR mode and ABR mode, denoted

as N_{WPR} and N_{ABR} , respectively, to S. From then on, R always selects the WPR mode, if $N_{\text{WPR}} > N_{\text{ABR}}$, and the ABR mode, if $N_{\text{ABR}} > N_{\text{WPR}}$, and uniformly selects between the ABR and WPR modes at random, otherwise if $N_{\text{ABR}} = N_{\text{WPR}}$.

Note that both of the proposed mode selection protocols are adopted only at the hybrid relay. ESAP operates based on the information including the physical parameters of R, i.e., ρ_{W} and ρ_{C} , and network environment-dependent parameters, i.e., ρ_{R} , and ν_{D} . The physical parameters can be known by the relay as predefined knowledge, while the network-dependent parameters can be obtained through detection at the beginning of each time slot. By contrast, ETCP chooses the mode based on the history information without knowing the current channel condition. It can be seen that both mode selection protocols are practical as they are based on information attainable at the hybrid relay.

It is worth mentioning that ESAP incurs much higher overhead than that of ETCP. In particular, ESAP requires the hybrid relay to know the expression of P_{R}^{W} in (4.1) and values of ρ_{W} and ρ_{C} a priori. Additionally, the hybrid relay with ESAP needs feedback from the destination node and calculation of P_{R}^{W} according to (4.1) for every time slot. By contrast, the hybrid relay with ETCP only incurs communication and computation overhead once at end of the exploration period, i.e., in the first initial $2n$ time slots, it only needs one feedback from the destination node and one comparison operation between the values of N_{WPR} and N_{ABR} after the first $2n$ initial time slots. Therefore, ETCP has much lower overhead than ESAP.

4.2.4 Geometric Modeling of the System

In this chapter, the stochastic geometry analysis of the proposed hybrid relaying is based on α -GPP [56]. The analysis on a generic point located at $\|\mathbf{x}\|$ is restricted to an observation window $\mathbb{O}_{\mathbf{x}}$, denoted as a circular Euclidean plane with positive radius R . α -GPP is a repulsive point process which allows characterizing the repulsion among the distribution of the randomly located points and covers the PPP as a special case (i.e., when $\alpha \rightarrow 0$). The coefficient α ($\alpha = -1/k$ for a positive integer k) indicates the repulsion degree of the spatial points. Specifically, the repulsion is the strongest with $\alpha = -1$ and disappears with $\alpha \rightarrow 0$.

4.2.5 Preliminaries

This subsection describes some primarily results of α -GPP modeling which are applied later in the analysis of this chapter. We consider that the hybrid relay R locates at the origin of the Euclidean space surrounded by the α -GPP distributed ambient emitters Ψ with transmit power \tilde{P}_T . In the Rayleigh fading environment, the distribution of the received signal power from Ψ at R, i.e., Q_R , are presented in the following proposition.

Proposition 3 [112, Theorem 1] *The probability density function (PDF) and cumulative distribution function (CDF) of Q_R are given, respectively, as*

$$f_{Q_R}(q) = \mathcal{L}^{-1} \left\{ \text{Det}(\text{Id} + \tilde{\alpha} \mathbb{G}_{\Psi}(\mathbf{x}, \mathbf{y}) \varpi_{\mathbf{x}}(s) \varpi_{\mathbf{y}}(s))^{-\frac{1}{\tilde{\alpha}}} \right\}(q), \quad (4.4)$$

$$\text{and } F_{Q_R}(q) = \mathcal{L}^{-1} \left\{ \frac{1}{s} \text{Det}(\text{Id} + \tilde{\alpha} \mathbb{G}_{\Psi}(\mathbf{x}, \mathbf{y}) \varpi_{\mathbf{x}}(s) \varpi_{\mathbf{y}}(s))^{-\frac{1}{\tilde{\alpha}}} \right\}(q), \quad (4.5)$$

where $\mathcal{L}^{-1}\{\cdot\}(x)$ represents the inverse Laplace transform which can be evaluated by the Mellin's inverse formula [90], $\text{Det}(\text{Id}+\cdot)$ denotes the Fredholm determinant [102, (10)], $\varpi_{\mathbf{z}}(s) \triangleq \sqrt{1 - (1 + s\tilde{P}_T\|\mathbf{z}\|^{-\tilde{\mu}})^{-1}}$, and $\mathbb{G}_{\Psi}(\mathbf{x}, \mathbf{y}) \triangleq \tilde{\zeta} \exp\left(-\frac{\pi\tilde{\zeta}}{2}(\|\mathbf{x}\|^2 + \|\mathbf{y}\|^2 - 2\mathbf{x}\bar{\mathbf{y}})\right)$, $\mathbf{x}, \mathbf{y} \in \Phi$, is the Ginibre kernel of Ψ , which represents the correlation force among different spatial points in Ψ .

4.3 Operational Model Selection Protocols

The advantage of the hybrid relay lies in the fact that it can select the more suitable operational mode to achieve better performance under different network conditions. However, as the hybrid relay is a wireless-powered device, any mode selection protocols that have heavy computational complexity, e.g., based on online optimizations, are not applicable. For implementation practicality, low complexity mode selection based on obtainable information and limited communication overhead needs to be devised. For the mode selection of the hybrid relay, we consider the situations with and without instantaneous CSI of active transmission. For the former and the latter situations, we propose two protocols, namely, *energy and SINR-aware Protocol (ESAP)* and *explore-then-commit protocol (ETCP)*, respectively, for the hybrid relay adapting to the network environment. The operational procedures of the mode selection protocols are specified as follows.

- ESAP: The idea of the ESAP is using ABR to assist data forwarding when the WPR is not feasible (i.e., either when R does not harvest sufficient energy or the forwarded data cannot be successfully decoded by D) based on the current system conditions. At the end of each energy harvesting phase, the mode selection of ESAP is performed based on the CSI of WPR mode which can

be obtained from the receiver's feedback for the training preambles sent by the transmitter [113]. In particular, S first sends preamble signals to R, and R detects its receive SINR ν_R and the amount of harvested energy E_R . If $\nu_R > \tau_W$ and $E_R > E_W$, R transmits preambles to D with transmit power given in (4.1). If the preamble signals from R are successfully decoded by D, i.e., $\nu_D^W > \tau_W$, D provides feedback of ν_D^W to R through signaling. R selects the WPR mode if the above two conditions are jointly satisfied, selects the ABR mode if the above two conditions are not jointly satisfied but the condition that $\nu_R > \tau_W$ and $E_R > E_A$ holds⁸, and remains silent otherwise. For ESAP, we consider the ideal case that the mode selection at the end of each energy harvesting phase causes negligible time and energy consumption.

- ETCP: The idea of the ETCP is to select the averagely better-performed mode in terms of success probability based on the history information. In particular, ECTP begins with an exploration period that occupies the first initial $2n$ ($n \in \mathbb{N}^+$) time slots to learn the network conditions before committing to a certain operation mode for steady-state transmission based on the learned knowledge. Specifically, in the exploration period, R works in each operational mode (WPR or ABR) for n time slots in an arbitrary sequence. Afterward, D feeds back the numbers of successful transmissions in the WPR mode and ABR mode, denoted as N_{WPR} and N_{ABR} , respectively, to S. Since then, R always selects the WPR mode, if $N_{WPR} > N_{ABR}$, and the ABR mode, if $N_{ABR} > N_{WPR}$, and uniformly selects between the ABR and WPR modes at random, if $N_{ABR} = N_{WPR}$.

Note that the hybrid relay with ESAP requires feedback from the destination node

⁸Equivalently, the ABR mode is selected if ($\nu_R > \tau_W$ and $E_W \geq E_R > E_A$) or ($\nu_R > \tau_W$, $E_R > E_W$, and $\nu_D^W \leq \tau_W$). Note that ESAP does not need the CSI of ABR.

and the calculation of P_R^W given in (4.1) every time slot. By contrast, the hybrid relay with ETCP only needs one feedback from the destination node at the end of the exploration period and one comparison operation between the values of N_{WPR} and N_{ABR} after the feedback. Therefore, ETCP incurs much lower communication and computation overhead than ESAP. We also note that ETCP is designed to choose the mode with higher success probability instead of capacity as the hybrid relaying mainly targets for IoT applications, such as wireless actuators and medical sensors, where the communication devices usually have low traffic volume and power budget. For those applications, instant access is more important than throughput. However, ETCP can be easily modified to favor capacity by letting the hybrid relay select the mode that results in higher achieved capacity in the exploration period. The modified ETCP is not considered in this chapter due to the space limit.

4.4 Analysis of Success Probability

In this section, we analyze the performance of the hybrid relaying system in the presence of randomly located ambient emitters and interferers. For this,

- we first derive the mode selection probabilities of the hybrid relay with the proposed protocols,
- we characterize the interference distribution under the α -GPP modeling framework and derive the success probabilities of the hybrid relaying with both ESAP and ETCP,
- and we also simplify the success probabilities in the special cases when one of the operational modes of the hybrid relay is disabled and when the distribution

of ambient transmitters follow PPPs.

The transmission of the dual-hop hybrid relaying system succeeds if 1) the relay can harvest sufficient energy for its circuit operation and the achieved SINR at the relay is greater than the threshold τ_W so that the information transmitted by the source can be successfully decoded and 2) the achieved SINR or SNR at the destination is greater than τ_W or τ_A so that the information forwarded by the relay through WPR or ABR, respectively, can be successfully decoded. Let $M \in \{W, A\}$ denote the operational mode indicator of the hybrid relay R. Mathematically, the success probability of the hybrid relaying is expressed as

$$\begin{aligned} \mathcal{S}_{\text{HR}} &= \mathbb{P}\left[\nu_{\text{R}} > \tau_{\text{W}}, \nu_{\text{D}}^{\text{W}} > \tau_{\text{W}}, E_{\text{R}} > E_{\text{W}}, M = \text{W}\right] \\ &\quad + \mathbb{P}\left[\nu_{\text{R}} > \tau_{\text{W}}, \nu_{\text{D}}^{\text{A}} > \tau_{\text{A}}, E_{\text{R}} > E_{\text{A}}, M = \text{A}\right] \\ &\stackrel{\text{(a)}}{=} \mathbb{P}\left[\nu_{\text{R}} > \tau_{\text{W}}, \nu_{\text{D}}^{\text{W}} > \tau_{\text{W}}, E_{\text{R}} > E_{\text{W}} | M = \text{W}\right] \mathbb{P}\left[M = \text{W}\right] \\ &\quad + \mathbb{P}\left[\nu_{\text{R}} > \tau_{\text{W}}, \nu_{\text{D}}^{\text{A}} > \tau_{\text{A}}, E_{\text{R}} > E_{\text{A}} | M = \text{A}\right] \mathbb{P}\left[M = \text{A}\right]. \end{aligned} \quad (4.6)$$

4.4.1 General-Case Result for ESAP

We first investigate the hybrid relaying with ESAP. Note that with block Rayleigh fading channels, the source-to-relay transmission and relay-to-destination transmission in the WPR mode are affected by the same set of interferers with static locations. In other words, the relay and destination nodes experience spatially and temporally correlated interference [114]. In this scenario, we characterize the success probability of hybrid relaying defined in (4.6) in the following theorem.

Theorem 4.4.1 *The success probability of the hybrid relaying with ESAP is*

$$\begin{aligned} \mathcal{S}_{\text{HR}}^{\text{ESAP}} = & \exp\left(-\kappa(\tau_{\text{W}})\sigma^2\right) \left(\chi_{\text{A}}(\tau_{\text{W}}, \rho_{\text{C}} - \rho_{\text{W}}) \left(1 - F_{Q_{\text{R}}}(\varrho_{\text{C}}) - \int_{\varrho_{\text{C}}}^{\infty} \delta(q) f_{Q_{\text{R}}}(q) dq \right) \right. \\ & + \int_{\varrho_{\text{W}}}^{\varrho_{\text{C}}} (1 - \delta(q)) \chi_{\text{A}}(\tau_{\text{W}}, \omega\beta q - \rho_{\text{W}}) f_{Q_{\text{R}}}(q) dq \\ & \left. + \text{Det}\left(\text{Id} + \alpha \mathbb{G}_{\Phi}(\mathbf{x}, \mathbf{y}) \psi_{\mathbf{x}}(\kappa(\tau_{\text{W}})) \psi_{\mathbf{y}}(\kappa(\tau_{\text{W}}))\right)^{-\frac{1}{\alpha}} \int_{\varrho_{\text{A}}}^{\infty} \delta(q) f_{Q_{\text{R}}}(q) dq \right), \end{aligned} \quad (4.7)$$

where $\kappa(v) \triangleq \frac{d_{\text{S,R}}^{\mu} v}{P_{\text{S}}}$, $\delta(q) \triangleq \exp\left(-\frac{d_{\text{R,D}}^{\mu} \tilde{\sigma}^2 \tau_{\text{A}}}{\eta \xi q}\right)$, $\mathbb{G}_{\Phi}(\mathbf{x}, \mathbf{y}) \triangleq \zeta \exp\left(-\frac{\pi \zeta}{2} (\|\mathbf{x}\|^2 + \|\mathbf{y}\|^2 - 2\mathbf{x}\bar{\mathbf{y}})\right)$, $\psi_{\mathbf{z}}(s) \triangleq \sqrt{1 - (1 + s P_{\text{T}} \|\mathbf{z}\|^{-\mu})^{-1}}$, $f_{Q_{\text{R}}}(q)$ and $F_{Q_{\text{R}}}(q)$ are given in (4.4) and (4.5), respectively, χ_{A} is given as:

$$\chi_{\text{A}}(v, p) = \exp\left(-\ell(v, p)\sigma^2\right) \text{Det}\left(\text{Id} + \alpha \mathbb{G}_{\Phi}(\mathbf{x}, \mathbf{y}) \varphi_{\mathbf{x}}(\ell(v, p)) \varphi_{\mathbf{y}}(\ell(v, p))\right)^{-\frac{1}{\alpha}}, \quad (4.8)$$

therein $\ell(v, p) \triangleq \frac{d_{\text{R,D}}^{\mu} v(1-\omega)}{2p}$, and

$$\varphi_{\mathbf{z}}(s) \triangleq \sqrt{1 - \left(1 + \kappa(\tau_{\text{W}}) P_{\text{T}} \|\mathbf{z}\|^{-\mu}\right)^{-1} \left(1 + s P_{\text{T}} \|\mathbf{z} - \mathbf{x}_{\text{D}}\|^{-\mu}\right)^{-1}}.$$

For readability, the proof of **Theorem 4.4.1** is presented in Appendix 4.8.1.

The analytical expression in (4.7) appears in terms of the Fredholm determinant [56], which allows efficient numerical evaluation of the relevant quantities [82, 112, 115, 116]. It is observed that the analytical expression of $\mathcal{S}_{\text{HR}}^{\text{ESAP}}$ in (4.7) has multiple terms. This is due to the feature that the proposed hybrid relaying has a two-mode operation. The analytical expression involves the joint probabilities that an operational mode is selected and the relay transmission in the selected mode is

successful. We note that the analytical expression in (4.7) has a comparable computational complexity to the analytical results in [112, 116]. The term that has the highest computational complexity (e.g., the last term in (4.7)) involves one integral of the inverse Laplace transform of the Fredholm determinant, which can be evaluated relatively easily with numerical integration tools.

4.4.2 Special-Case Results

Next, we investigate some special settings in which the general-case result in (4.7) can be considerably simplified.

Pure Ambient Backscatter Relaying

In the special case when R forwards information from S to D through ambient backscattering only, referred to as *pure ABR*, we have the corresponding success probability as follows.

Corollary 2 *The success probability of the pure ABR is*

$$\mathcal{S}_{\text{ABR}} = \exp\left(-\kappa(\tau_{\text{W}})\sigma^2\right) \text{Det}\left(\text{Id} + \alpha \mathbb{G}_{\Phi}(\mathbf{x}, \mathbf{y}) \psi_{\mathbf{x}}(\kappa(\tau_{\text{W}})) \psi_{\mathbf{y}}(\kappa(\tau_{\text{W}}))\right)^{-\frac{1}{\alpha}} \times \int_{\varrho_{\text{A}}}^{\infty} \delta(q) f_{Q_{\text{R}}}(q) dq, \quad (4.9)$$

where $f_{Q_{\text{R}}}(q)$ is given in (4.4).

Proof. The performance of the pure ABR can be derived by setting R exclusively in ABR mode for relaying as long as the harvested energy is enough to support the function. Mathematically, by plugging $\mathbb{P}[\text{M} = \text{W}] = 0$ and $\mathbb{P}[\text{M} = \text{A}] = \mathbb{P}[E_{\text{R}} > E_{\text{A}}]$ into the definition in (4.6), the corresponding success probability can

be expressed as

$$\mathcal{S}_{\text{ABR}} = \mathbb{P}\left[\nu_{\text{R}} > \tau_{\text{W}}, \nu_{\text{D}}^{\text{A}} > \tau_{\text{A}}, E_{\text{R}} > E_{\text{A}}\right], \quad (4.10)$$

which is equivalent to the second term of $\mathcal{S}_{\text{A}}^{\text{ESAP}}$ in (4.31) with E_{W} replaced by ∞ . Therefore, the analytical expression of \mathcal{S}_{ABR} in (4.9) yields from the derivation of $\mathcal{S}_{\text{A}}^{\text{ESAP}}$ with the mentioned replacement. ■

We note that the success probability of the hybrid relaying in (4.7) can be expanded as follows:

$$\begin{aligned} & \mathcal{S}_{\text{HR}}^{\text{ESAP}} \\ &= \mathbb{P}\left[\nu_{\text{R}} > \tau_{\text{W}}, \nu_{\text{D}}^{\text{W}} > \tau_{\text{W}}, \nu_{\text{D}}^{\text{A}} > \tau_{\text{A}}, E_{\text{R}} > E_{\text{W}}\right] + \mathbb{P}\left[\nu_{\text{R}} > \tau_{\text{W}}, \nu_{\text{D}}^{\text{W}} > \tau_{\text{W}}, \nu_{\text{D}}^{\text{A}} \leq \tau_{\text{A}}, E_{\text{R}} > E_{\text{W}}\right] \\ &+ \mathbb{P}\left[\nu_{\text{R}} > \tau_{\text{W}}, \nu_{\text{D}}^{\text{A}} > \tau_{\text{A}}, \nu_{\text{D}}^{\text{W}} \leq \tau_{\text{W}}, E_{\text{R}} > E_{\text{W}}\right] + \mathbb{P}\left[\nu_{\text{R}} > \tau_{\text{W}}, \nu_{\text{D}}^{\text{A}} > \tau_{\text{A}}, E_{\text{W}} \geq E_{\text{R}} > E_{\text{A}}\right] \\ &= \mathbb{P}\left[\nu_{\text{R}} > \tau_{\text{W}}, \nu_{\text{D}}^{\text{A}} > \tau_{\text{A}}, E_{\text{R}} > E_{\text{A}}\right] + \mathbb{P}\left[\nu_{\text{R}} > \tau_{\text{W}}, \nu_{\text{D}}^{\text{W}} > \tau_{\text{W}}, \nu_{\text{D}}^{\text{A}} \leq \tau_{\text{A}}, E_{\text{R}} > E_{\text{W}}\right], \quad (4.11) \end{aligned}$$

where the first equality follows by expanding the first term of (4.31) into two cases when $\nu_{\text{D}}^{\text{A}} > \tau_{\text{A}}$ and $\nu_{\text{D}}^{\text{A}} \leq \tau_{\text{A}}$ and the last equality follows by combining the first, the third and the fourth terms before the equality. One finds that the probability representation of \mathcal{S}_{ABR} in (4.10) is exactly the first term of (4.11). Given that the second term of (4.11) is always positive, we have the following observation.

Remark 1: The success probability of the hybrid relaying with ESAP is strictly higher than that of the pure ABR.

Let $\mathcal{G}_{\text{ABR}}^{\text{ESAP}}$ denote the performance improvement of the hybrid relaying with ESAP over the pure ABR in terms of the success probability, i.e., $\mathcal{G}_{\text{ABR}}^{\text{ESAP}} = \mathcal{S}_{\text{HR}}^{\text{ESAP}} - \mathcal{S}_{\text{ABR}}$.

In particular, we have

$$\mathcal{G}_{\text{ABR}}^{\text{ESAP}} = \exp\left(-\kappa(\tau_{\text{W}})\sigma^2\right) \underbrace{\left(\chi_{\text{A}}(\tau_{\text{W}}, \rho_{\text{C}} - \rho_{\text{W}}) \left(1 - F_{Q_{\text{R}}}\left(\frac{\rho_{\text{C}}}{\omega\beta}\right) - \int_{\frac{\rho_{\text{C}}}{\omega\beta}}^{\infty} \delta(q) f_{Q_{\text{R}}}(q) dq\right)\right)}_{\mathcal{G}_1} + \underbrace{\int_{\frac{\rho_{\text{W}}}{\omega\beta}}^{\frac{\rho_{\text{C}}}{\omega\beta}} (1 - \delta(q)) \chi_{\text{A}}(\tau_{\text{W}}, \omega\beta q - \rho_{\text{W}}) f_{Q_{\text{R}}}(q) dq}_{\mathcal{G}_2}. \quad (4.12)$$

Based on the expansion of the Fredholm determinant in [116, eqn. 14], $\chi_{\text{A}}(\tau_{\text{W}}, \rho_{\text{C}} - \rho_{\text{W}})$ can be expressed as

$$\chi_{\text{A}}(\tau_{\text{W}}, \rho_{\text{C}} - \rho_{\text{W}}) = \exp\left(-\frac{d_{\text{R,D}}^{\mu} \tau_{\text{W}} (1 - \omega) \sigma^2}{2(\rho_{\text{C}} - \rho_{\text{W}})}\right) \times \prod_{n \geq 0} \left(1 + \frac{2\alpha(\pi\zeta)^{n+1}}{n!} \int_0^R \frac{\exp(-\pi\zeta r^2) r^{2n+1}}{1 + 2(\rho_{\text{C}} - \rho_{\text{W}}) r^{\mu} (d_{\text{R,D}}^{\mu} \tau_{\text{W}} (1 - \omega) P_{\text{T}})^{-1}} dr\right)^{-\frac{1}{\alpha}}. \quad (4.13)$$

As the repulsion factor $\alpha \in [-1, 0)$ and all the other parameters take positive values, it is readily checked that χ_{A} is an increasing function of $\rho_{\text{C}} - \rho_{\text{W}}$. Given that the physical capacity of the capacitor, i.e., ρ_{C} , is fixed, χ_{A} decreases with the increase of ρ_{W} . As a result, both \mathcal{G}_1 and \mathcal{G}_2 in (4.12), and thus $\mathcal{G}_{\text{ABR}}^{\text{ESAP}}$, are decreasing functions of ρ_{W} . It is also noted that ρ_{A} does not appear in the expression of $\mathcal{G}_{\text{ABR}}^{\text{ESAP}}$.

Remark 2: According to (4.12), the improvement of the hybrid relaying with ESAP over the pure ABR $\mathcal{G}_{\text{ABR}}^{\text{HR}}$ can be increased with the reduced circuit power consumption E_{W} , while $\mathcal{G}_{\text{ABR}}^{\text{HR}}$ is not affected by any change of the circuit power consumption E_{A} .

Furthermore, considering the special case of **Corollary 2** where the distributions of Ψ and Φ exhibit no repulsion, i.e., the Poisson field of the ambient emitters and interferers with $\tilde{\alpha} \rightarrow 0$ and $\alpha \rightarrow 0$, we can simplify \mathcal{S}_{ABR} in a closed form.

Corollary 3 *When the path-loss exponent μ equals 4, the success probability of pure ABR in the Poisson field of ambient emitters and interferers is*

$$\mathcal{S}_{\text{ABR}} = \frac{\pi^2}{4} \tilde{\zeta} \sqrt{\tilde{P}_T N^{-1}} \exp\left(-\frac{d_{\text{S,R}}^4 \sigma^2 \tau_{\text{W}}}{P_{\text{S}}} - \frac{\pi^2 \zeta d_{\text{S,R}}^2}{2} \sqrt{\frac{\tau_{\text{W}} P_T}{P_{\text{S}}}}\right) \text{Erf}\left(\sqrt{N \varrho_{\text{A}}^{-1}}\right), \quad (4.14)$$

where $N \triangleq \frac{d_{\text{R,D}}^4 \tilde{\sigma}^2 \tau_{\text{A}}}{\eta \xi} + \frac{\pi^4 \zeta_{\text{Q}}^2 \tilde{P}_T}{16}$ and $\text{Erf}(t) = \frac{1}{\sqrt{t}} \int_{-t}^t \exp(-x^2) dx$ is the error function [117].

The proof of **Corollary 3** is presented in Appendix 4.8.2.

The closed-form expression in (4.14) directly reveals the effects of the parameters on the success probability. As the circuit power consumption of the pure ABR is ultra-low, we have $\varrho_{\text{A}} \rightarrow 0$, and thus $\text{Erf}\left(\sqrt{\frac{N}{\varrho_{\text{A}}}}\right) \rightarrow 1$ and $\mathcal{S}_{\text{ABR}} \approx \frac{\pi^2}{4} \tilde{\zeta} \sqrt{\frac{\tilde{P}_T}{N}} \exp\left(-\frac{d_{\text{S,R}}^4 \sigma^2 \tau_{\text{W}}}{P_{\text{S}}} - \frac{\pi^2 \zeta d_{\text{S,R}}^2}{2} \sqrt{\frac{\tau_{\text{W}} P_T}{P_{\text{S}}}}\right)$. One easily observes that \mathcal{S}_{ABR} is an increasing function of $\tilde{\zeta}$, P_{S} , and \tilde{P}_T , and a decreasing function of τ_{W} , τ_{A} , $d_{\text{S,R}}$, $d_{\text{R,D}}$, ζ , and P_T .

Pure Wireless-Powered Relaying

Next, we consider another special case when R forwards information over the relay-to-destination link only with wireless-powered transmission referred to as the pure WPR. The corresponding success probability is given in the following corollary.

Corollary 4 *The success probability of the pure WPR is*

$$\begin{aligned} \mathcal{S}_{\text{WPR}} = \exp\left(-\kappa(\tau_{\text{W}})\sigma^2\right) & \left(\int_{\varrho_{\text{W}}}^{\varrho_{\text{C}}} \chi_{\text{A}}(\tau_{\text{W}}, \omega\beta q - \rho_{\text{W}}) f_{\text{Q}_{\text{R}}}(q) dq \right. \\ & \left. + \chi_{\text{A}}(\tau_{\text{W}}, \rho_{\text{C}} - \rho_{\text{W}}) \left(1 - F_{\text{Q}_{\text{R}}}(\varrho_{\text{C}})\right) \right), \quad (4.15) \end{aligned}$$

where χ_{A} , $F_{\text{Q}_{\text{R}}}(q)$, and $f_{\text{Q}_{\text{R}}}(q)$ are given in (4.8), (4.5), and (4.4), respectively.

Proof. The performance of the pure WPR can be obtained by letting R forward the information from S to D with active transmission only, once the harvested energy is sufficient for the function. Mathematically, we have $\mathbb{P}[M = W] = \mathbb{P}[\nu_R > \tau_W, \nu_D^W > \tau_W, E_R > E_W]$ and $\mathbb{P}[M = A] = 0$. By assigning the above conditions to the definition in (4.6), the corresponding success probability can be expressed as

$$\mathcal{S}_{\text{WPR}} = \mathbb{P}[\nu_R > \tau_W, \nu_D^W > \tau_W, E_R > E_W], \quad (4.16)$$

which is exactly the probability representation of $\mathcal{S}_W^{\text{ESAP}}$ in (4.31). Therefore, the analytical expression of \mathcal{S}_{WPR} in (4.15) can be directly obtained from (4.35). ■

Remark 3: As the probability representation of \mathcal{S}_{WPR} in (4.16) is exactly $\mathcal{S}_W^{\text{ESAP}}$ in (4.31), we have $\mathcal{S}_{\text{HR}}^{\text{ESAP}} = \mathcal{S}_W^{\text{ESAP}} + \mathcal{S}_A^{\text{ESAP}} > \mathcal{S}_{\text{WPR}}$, noting that $\mathcal{S}_A^{\text{ESAP}}$ is positive. Therefore, the success probability of the hybrid relaying with ESAP is strictly higher than that of the pure WPR.

Let $\mathcal{G}_{\text{WPR}}^{\text{HR}}$ denote the performance improvement of the hybrid relaying over the pure WPR in terms of the success probability, i.e., $\mathcal{G}_{\text{WPR}}^{\text{ESAP}} = \mathcal{S}_{\text{HR}}^{\text{ESAP}} - \mathcal{S}_{\text{WPR}}$. In particular, we have

$$\begin{aligned} & \mathcal{G}_{\text{WPR}}^{\text{ESAP}} \\ &= \exp(-\kappa(\tau_W)\sigma^2) \left(\underbrace{\left(\text{Det} \left(\text{Id} + \alpha \mathbb{G}_\Phi(\mathbf{x}, \mathbf{y}) \psi_{\mathbf{x}}(\kappa(\tau_W)) \psi_{\mathbf{y}}(\kappa(\tau_W)) \right) \right)^{-\frac{1}{\alpha}}}_{\mathcal{G}_3} \int_{\varrho_A}^{\infty} \delta(q) f_{Q_R}(q) dq \right. \\ & \left. - \underbrace{\chi_{\mathbb{A}}(\tau_W, \rho_C - \rho_W) \left(\int_{\varrho_C}^{\infty} \delta(q) f_{Q_R}(q) dq + \int_{\varrho_W}^{\varrho_C} \delta(q) \chi_{\mathbb{A}}(\tau_W, \omega\beta q - \rho_W) f_{Q_R}(q) dq \right)}_{\mathcal{G}_4} \right). \end{aligned} \quad (4.17)$$

Recall that χ_A is a decreasing function of ρ_W from the previous analysis. Given that the physical capacity of the capacitor is fixed, it is readily checked that \mathcal{G}_3 remains constant with ϱ_W while \mathcal{G}_4 decreases with ρ_W , and thus ϱ_W . Hence, $\mathcal{G}_{\text{WPR}}^{\text{ESAP}}$ is an increasing function of ϱ_W . Additionally, we have

$$\frac{\partial \mathcal{G}_{\text{WPR}}^{\text{ESAP}}}{\partial \varrho_A} = -\exp(-\kappa(\tau_W)\sigma^2)\mathcal{G}_3\delta(\varrho_A)f_{Q_A}(\varrho_A) < 0.$$

Thus, $\mathcal{G}_{\text{WPR}}^{\text{ESAP}}$ is a decreasing function of ϱ_A .

Remark 4: It is observed from (4.17) that the improvement of the hybrid relaying with ESAP over the pure WPR becomes more remarkable with increased circuit power consumption E_W and reduced circuit power consumption E_A .

4.4.3 General-Case Results for ETCP

Next, we continue to investigate the performance of hybrid relaying with ETCP at the steady states when R has committed to a particular mode based on its selection criterion. The mode selection probability of ETCP depends on the average success probabilities of the pure ABR and WPR, which have been obtained in **Corollary 2** and **Corollary 4**, respectively. Based on these results with ETCP, we have the success probability of hybrid relaying in the following theorem.

Theorem 4.4.2 *The success probability of the hybrid relaying with ETCP at the steady states is*

$$\mathcal{S}_{\text{HR}}^{\text{ETCP}} = \frac{1}{2}(\mathcal{S}_{\text{WPR}} + \mathcal{S}_{\text{ABR}}) + \frac{1}{2}\left(\phi(\mathcal{S}_{\text{WPR}}, \mathcal{S}_{\text{ABR}}) - \phi(\mathcal{S}_{\text{ABR}}, \mathcal{S}_{\text{WPR}})\right)(\mathcal{S}_{\text{WPR}} - \mathcal{S}_{\text{ABR}}), \quad (4.18)$$

where \mathcal{S}_{ABR} and \mathcal{S}_{WPR} are given in (4.9) and (4.15), respectively, and ϕ is given as

$$\phi(x, y) = \sum_{i=1}^n \sum_{j=1}^i \binom{n}{i} \binom{n}{i-j} x^i (1-x)^{n-i} y^{i-j} (1-y)^{n-i+j}.$$

The proof of **Theorem** 4.4.2 can be found in Appendix 4.8.3.

When the hybrid relay adopts a strategy that uniformly selects between the ABR and WPR modes at random, referred to as *uniform random mode selection* (URMS), the corresponding success probability can be easily obtained by averaging the success probabilities of the two modes, i.e., $\mathcal{S}_{\text{HR}}^{\text{URMS}} = \frac{1}{2}(\mathcal{S}_{\text{ABR}} + \mathcal{S}_{\text{WPR}})$. Let $\Upsilon \triangleq \mathcal{S}_{\text{HR}}^{\text{ETCP}} - \mathcal{S}_{\text{HR}}^{\text{URMS}} = \frac{1}{2}(\phi(\mathcal{S}_{\text{WPR}}, \mathcal{S}_{\text{ABR}}) - \phi(\mathcal{S}_{\text{ABR}}, \mathcal{S}_{\text{WPR}}))(\mathcal{S}_{\text{WPR}} - \mathcal{S}_{\text{ABR}})$. It is readily checked that $\phi(\mathcal{S}_{\text{WPR}}, \mathcal{S}_{\text{ABR}}) - \phi(\mathcal{S}_{\text{ABR}}, \mathcal{S}_{\text{WPR}})$ and $\mathcal{S}_{\text{WPR}} - \mathcal{S}_{\text{ABR}}$ are both positive, both negative, or both equal to zero. Therefore, we have $\Upsilon \geq 0$, which yields the following observation.

Remark 5: The success probability of the hybrid relaying with ETCP is strictly no worse than that with uniformly random mode selection.

4.5 Analysis of Ergodic Capacity

This section investigates the end-to-end ergodic capacity that can be achieved from the hybrid relaying. Specifically, we provide the general-case results for hybrid relaying with ESAP and ETCP and the special-case results for pure ABR and WPR.

The ergodic capacity of the hybrid relaying can be defined as

$$\begin{aligned} \mathcal{C}_{\text{HR}} &\triangleq \frac{(1-\omega)}{2} \left(C_{\text{W}} \mathbb{P}[\text{M} = \text{W}] + C_{\text{A}} \mathbb{P}[\text{M} = \text{A}] \right) \\ &= \frac{(1-\omega)}{2} \left(\mathbb{E} \left[W \log_2(1+\nu) | \text{M} = \text{W} \right] \mathbb{P}[\text{M} = \text{W}] \right. \\ &\quad \left. + C_{\text{A}} \mathbb{P} \left[\nu_{\text{R}} > \tau_{\text{W}}, \nu_{\text{D}}^{\text{A}} > \tau_{\text{A}} | \text{M} = \text{A} \right] \mathbb{P}[\text{M} = \text{A}] \right), \end{aligned} \quad (4.19)$$

where the coefficient $\frac{1-\omega}{2}$ comes from the fact that the transmission for each hop occupies $\frac{1-\omega}{2}$ fraction of a time slot duration and the last equality follows the assumption that $C_{\text{A}} \ll C_{\text{W}}$.

4.5.1 General-Case Results for ESAP

According to the definition in (4.19), the ergodic capacity of the hybrid relaying with ESAP is presented in the following theorem.

Theorem 4.5.1 *The ergodic capacity of the hybrid relaying with ESAP is*

$$\begin{aligned} \mathcal{C}_{\text{HR}} &= \frac{1-\omega}{2} \left(\frac{W}{\ln(2)} \int_{\tau_{\text{W}}}^{\infty} \frac{\exp(-\kappa(v)\sigma^2)}{1+v} \left(\chi_{\text{A}}(v, \rho_{\text{C}} - \rho_{\text{W}}) \left(1 - F_{Q_{\text{R}}}(\varrho_{\text{C}}) \right) \right. \right. \\ &\quad \left. \left. + \int_{\varrho_{\text{W}}}^{\varrho_{\text{C}}} \chi_{\text{A}}(v, \omega\beta q - \rho_{\text{W}}) f_{Q_{\text{R}}}(q) dq \right) dv + C_{\text{A}} \mathcal{S}_{\text{A}}^{\text{ESAP}} \right), \end{aligned} \quad (4.20)$$

where χ_{A} , $F_{Q_{\text{R}}}(q)$, $f_{Q_{\text{R}}}(q)$, and $\mathcal{S}_{\text{A}}^{\text{ESAP}}$ are given in (4.8), (4.5), (4.4), and (4.36), respectively.

The proof of **Theorem 4.5.1** is presented in Appendix 4.8.4.

4.5.2 Special-Case results

For the analysis of the ergodic capacity, we also investigate the special cases when R relays the information from S to D by using only ambient backscattering or only wireless-powered transmission. In particular, the result of the former case is presented in the following corollary.

Corollary 5 *The capacity of the pure ABR is*

$$\begin{aligned} \mathcal{C}_{\text{ABR}} = & \frac{(1-\omega)C_A}{2} \exp\left(-\kappa(\tau_W)\sigma^2\right) \\ & \times \text{Det}\left(\text{Id} + \alpha \mathbb{G}_{\Phi}(\mathbf{x}, \mathbf{y}) \psi_{\mathbf{x}}(\kappa(\tau_W)) \psi_{\mathbf{y}}(\kappa(\tau_W))\right)^{-\frac{1}{\alpha}} \int_{\varrho_A}^{\infty} \delta(q) f_{Q_R}(q) dq, \end{aligned} \quad (4.21)$$

where $f_{Q_R}(q)$ is given in (4.4).

Proof. If the relay-to-destination transmission is performed only through ambient backscattering, we have

$$\mathbb{P}[M = W] = 0 \quad \text{and} \quad \mathbb{P}[M = A] = \mathbb{P}[\nu_R > \tau_A, \nu_D^A > \tau_A, E_R > E_A] = \mathcal{S}_{\text{ABR}}, \quad (4.22)$$

By assigning (4.22) into the definition in (4.19), we have the corresponding ergodic capacity as

$$\mathcal{C}_{\text{ABR}} = \frac{1-\omega}{2} C_A \mathcal{S}_{\text{ABR}}, \quad (4.23)$$

where \mathcal{S}_{ABR} has been obtained in **Corollary 2**.

Subsequently, \mathcal{C}_{ABR} in (4.21) can be directly obtained by inserting \mathcal{S}_{ABR} in (4.9) into (4.23). ■

Moreover, if R performs relaying with only the wireless-powered transmission, we

have the capacity of the pure WPR in the following corollary.

Corollary 6 *The capacity of the pure WPR is*

$$\mathcal{C}_{\text{WPR}} = \frac{W(1-\omega)}{2\ln(2)} \int_{\tau_{\text{W}}}^{\infty} \frac{\exp(-\kappa(v)\sigma^2)}{1+v} \left(\chi_{\text{A}}(v, \rho_{\text{C}} - \rho_{\text{W}}) \left(1 - F_{Q_{\text{R}}}(\varrho_{\text{C}})\right) + \int_{\varrho_{\text{W}}}^{\varrho_{\text{C}}} \chi_{\text{A}}(v, \omega\beta q - \rho_{\text{W}}) f_{Q_{\text{R}}}(q) dq \right) dv, \quad (4.24)$$

where χ_{A} , $F_{Q_{\text{R}}}(q)$, and $f_{Q_{\text{R}}}(q)$ are given in (4.8), (4.5), and (4.4), respectively.

Proof. From the proof of **Corollary 6**, we have the conditions that R only performs WPR as

$$\mathbb{P}[\text{M} = \text{W}] = \mathbb{P}[\nu_{\text{R}} > \tau_{\text{W}}, E_{\text{R}} > E_{\text{W}}, \nu_{\text{D}}^{\text{W}} > \tau_{\text{W}}] \quad \text{and} \quad \mathbb{P}[\text{M} = \text{A}] = 0. \quad (4.25)$$

By inserting (4.25) into (4.19), we have

$$\mathcal{C}_{\text{WPR}} = \frac{(1-\omega)}{2} \mathbb{E} \left[W \log_2(1+\nu) \mathbf{1}_{\{\nu_{\text{R}} > \tau_{\text{W}}, \nu_{\text{D}}^{\text{W}} > \tau_{\text{W}}, E_{\text{R}} > E_{\text{W}}\}} \right], \quad (4.26)$$

where $\mathbb{E} \left[W \log_2(1+\nu) \mathbf{1}_{\{\nu_{\text{R}} > \tau_{\text{W}}, \nu_{\text{D}}^{\text{W}} > \tau_{\text{W}}, E_{\text{R}} > E_{\text{W}}\}} \right]$ has been obtained in (4.44). We, therefore, have \mathcal{C}_{WPR} in (4.24) by plugging (4.44) into (4.26). ■

4.5.3 General-Case Results for ETCP

Theorem 4.5.2 *The ergodic capacity of the hybrid relaying with ETCP at the steady states is*

$$\mathcal{C}_{\text{HR}}^{\text{ETCP}} = \frac{1}{2}(\mathcal{C}_{\text{ABR}} + \mathcal{C}_{\text{WPR}}) + \frac{1}{2} \left(\phi(\mathcal{S}_{\text{WPR}}, \mathcal{S}_{\text{ABR}}) - \phi(\mathcal{S}_{\text{ABR}}, \mathcal{S}_{\text{WPR}}) \right) (\mathcal{C}_{\text{WPR}} - \mathcal{C}_{\text{ABR}}), \quad (4.27)$$

where \mathcal{C}_{ABR} , \mathcal{C}_{WPR} , \mathcal{S}_{ABR} , and \mathcal{S}_{WPR} have been obtained in (4.21), (4.24), (4.9), and (4.15), respectively.

Proof. Recall that, from the proof of Theorem 4.4.2, we have obtained the probability of R selecting the ABR mode and WPR mode under ETCP at the steady states in (4.41) and (4.42), respectively. According to the mode selection criterion of ETCP described in Section 4.2, the ergodic capacity of the hybrid relaying with ETCP at the steady states can be expressed as

$$\mathcal{C}_{\text{HR}}^{\text{ETCP}} = \frac{1}{2}(\mathcal{C}_{\text{ABR}} + \mathcal{C}_{\text{WPR}}) + \frac{1}{2}(\mathbb{P}[N_{\text{WPR}} > N_{\text{ABR}}] - \mathbb{P}[N_{\text{ABR}} > N_{\text{WPR}}])(\mathcal{C}_{\text{WPR}} - \mathcal{C}_{\text{ABR}}). \quad (4.28)$$

By inserting the expressions of $\mathbb{P}[N_{\text{ABR}} > N_{\text{WPR}}]$, $\mathbb{P}[N_{\text{WPR}} > N_{\text{ABR}}]$, \mathcal{C}_{ABR} , and \mathcal{C}_{WPR} obtained in (4.41), (4.42), (4.21), and (4.24), respectively, into (4.28), we have the expression of $\mathcal{C}_{\text{HR}}^{\text{ETCP}}$ in (4.27). ■

4.6 Numerical Results

In this section, we show numerical results to validate and evaluate the success probabilities and ergodic capacity of the hybrid relaying system analyzed in Section 4.4. To demonstrate the advantage of the proposed hybrid relaying with the mode selection protocols, we compare their performance with that of the pure WPR, and the pure ABR. The performance results of the hybrid relaying with ESAP and those with ETCP, the pure WPR and the pure ABR are labeled as “HR-EASP”, “HR-ETCP”, “WPR” and “ABR”, respectively. In the simulation, the ambient emitters Ψ and interferers Φ are distributed on a circular disc of radius $R = 500$ m with the relay node R centered at the origin. Besides, the source node S and destination node D

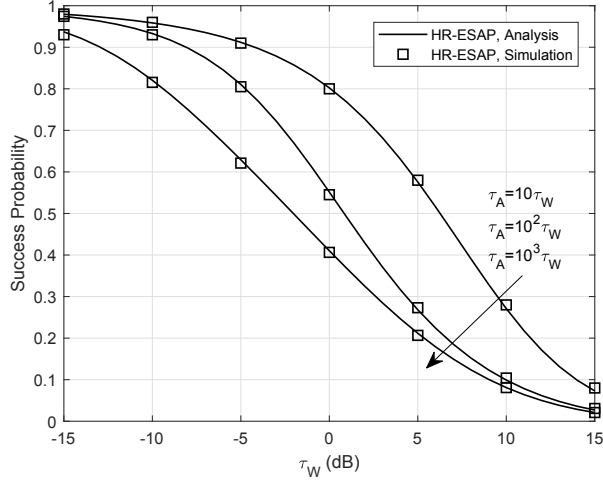
are placed at $(-d_{S,R},0)$ and $(d_{R,D},0)$, respectively. Ψ and Φ are considered as BSs and sensor devices with transmit power $\tilde{P}_T = 40$ dBm and $P_T = 20$ dBm, respectively. The frequency bandwidth of Ψ and Φ are set as 20 MHz [118] and 50 kHz [119], respectively. The noise variance is -120 dBm/Hz. We set the transmit power of the source node as $P_S = P_T$. The energy harvesting time fraction of the hybrid relay is set at $\omega = 0.4$. If the WPR is adopted, the average circuit power consumption rate of R is set at $\rho_W = 50\mu W$, which is within the typical power consumption range of a wireless-powered transmitter [156]. For the ABR, we set $\rho_A = 5\mu W$, an order of magnitude smaller than ρ_W . The normalized capacitor capacity ρ_C is 0.02 Joules/second. The ambient backscattering efficiency and capacity are set at $\xi = 0.25$ and $C_A = 50$ Kbps, respectively. The other system parameters adopted are listed in Table 4.2 unless otherwise stated.

Table 4.2: Parameter Setting.

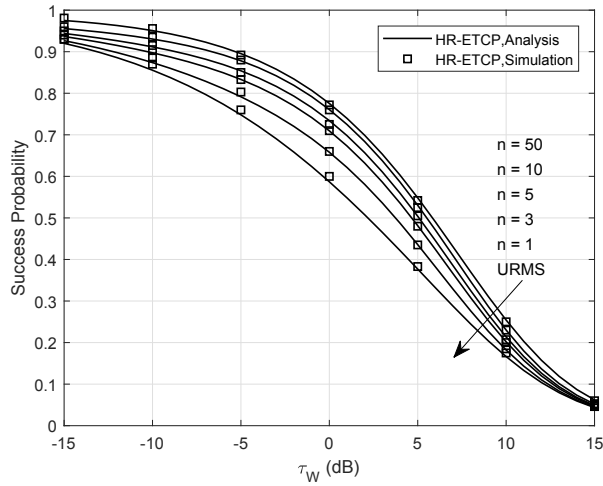
Symbol	α	$\tilde{\alpha}$	μ	$\tilde{\mu}$	$d_{S,R}, d_{R,D}$	τ_W	τ_A	η	β
Value	-0.5	-1	3.5	3.0	5 m	0 dB	20 dB	0.375 [75]	0.5 [60]

4.6.1 SINR Threshold on Success Probability

In Fig. 5.1, the success probabilities \mathcal{S}_{HR}^{ESAP} and \mathcal{S}_{HR}^{ETCP} obtained in **Theorem 4.4.1** and **Theorem 4.4.2**, respectively, are shown as functions of the SINR threshold τ_W . To demonstrate the accuracy of the analytical expressions, we compare them with the results generated by Monte Carlo simulations. It can be seen that for both \mathcal{S}_{HR}^{ESAP} and \mathcal{S}_{HR}^{ETCP} , the analytical results match closely with the simulation results over a wide range of τ_W and τ_A . Fig. 4.3(b) depicts \mathcal{S}_{HR}^{ETCP} under different settings of n . For comparison, we also show the success probability of hybrid relaying with URMS, i.e., $\mathcal{S}_{HR}^{URMS} = \frac{1}{2}(\mathcal{S}_{ABR} + \mathcal{S}_{WPR})$, labeled as ‘‘URMS’’. It can be found that \mathcal{S}_{ETCP}



(a) ESAP



(b) ETCP ($\tau_W = 10\tau_W$)

Figure 4.3: Success probability as a function of τ_W .

under different settings of n outperforms all $\mathcal{S}_{\text{HR}}^{\text{URMS}}$, which agrees with **Remark 5**. Moreover, $\mathcal{S}_{\text{ETCP}}$ monotonically increase with n . This is due to the fact that the more number of the time slots to explore, the higher chance the hybrid relay finds the averagely better-performed mode. We can see that the performance gap resulted from the increase of n decreases when n is large. In the following simulations, the

value of n is set as 5 to avoid a lengthy exploration period.

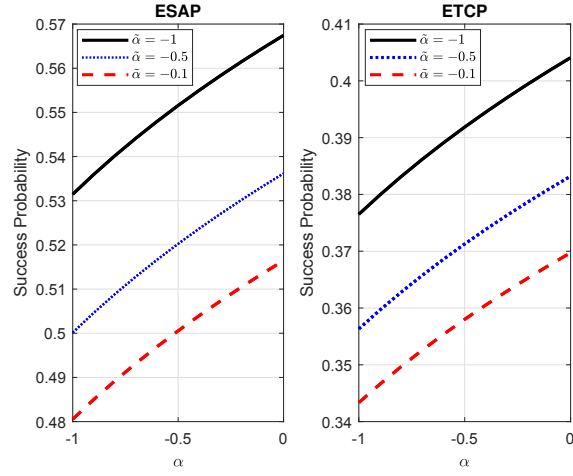


Figure 4.4: Success probability as a function of α .

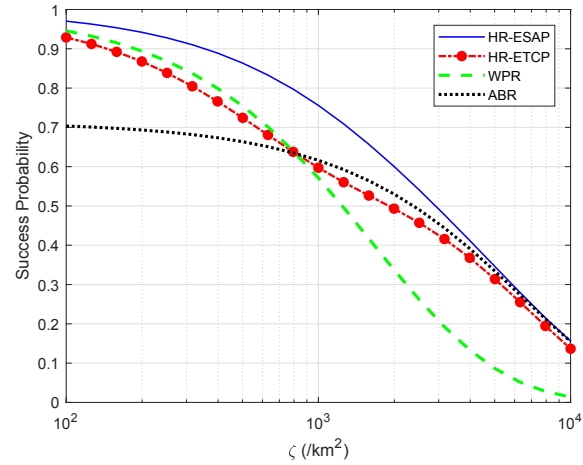


Figure 4.5: Success probability as a function of ζ . ($\tilde{\zeta} = 2000/\text{km}^2$)

4.6.2 Impact of System Environment (i.e., repulsion factors $\tilde{\alpha}$ and α and densities $\tilde{\zeta}$ and ζ of Ψ and Φ) on Success Probability

Fig. 4.4 shows the success probabilities $\mathcal{S}_{\text{HR}}^{\text{ESAP}}$ and $\mathcal{S}_{\text{HR}}^{\text{ETCP}}$ as functions of α under different $\tilde{\alpha}$. It can be found that greater repulsion among the ambient emitters Ψ , i.e., smaller $\tilde{\alpha}$, increases the success probabilities. By contrast, greater repulsion among the interferers Φ decreases the success probabilities. This comes from the fact that, given the spatial density, larger repulsion among the transmitters in Ψ (Φ) results in the higher probability that some transmitters in Ψ (Φ) locate near R, and thus stronger received signals from Ψ (Φ). As a result, smaller $\tilde{\alpha}$ leads to more carrier signals for energy harvesting and smaller α generates more interference at R.

Fig. 4.5 studies how the success probabilities vary under different density of interferers ζ . As expected, the success probabilities monotonically decrease with ζ . We observe that the hybrid relaying with ESAP achieves a higher success probability than that of the pure ABR and the pure WPR, which corroborates **Remark 1** and **Remark 3**, respectively. Given the knowledge of receive SINR at the destination node, ESAP can switch the hybrid relay to the ABR mode when the detected interference is high. Therefore, the hybrid relaying with ESAP outperforms both the pure WPR the pure ABR. When ζ is large, e.g., $\zeta = 10^4/\text{km}^2$, pure ABR achieves comparable performance to that of the hybrid relaying with ESAP.

For the hybrid relaying with ETCP, $\mathcal{S}_{\text{HR}}^{\text{ETCP}}$ approaches the better-performed mode (WPR or ABR) than the worse-performed mode in most conditions, which demonstrates the effectiveness of the exploration period in determining the better-performed mode. For the pure ABR, it is worth noting that, though the interference

on the transmit frequency of Φ does not affect the ABR link on the transmit frequency of Ψ , the interference still affects the source-to-relay link and thus \mathcal{S}_{ABR} . Since only the source-to-relay link is affected, \mathcal{S}_{ABR} is more robust to the impact of increased interference than \mathcal{S}_{WPR} . This is evident from Fig. 4.5 that \mathcal{S}_{ABR} decreases with the increase of ρ at a much slower rate than that of \mathcal{S}_{WPR} .

Fig. 4.6 examines the impact of the density of the ambient emitters $\tilde{\zeta}$. In contrast to the influence of ζ , the increase of $\tilde{\zeta}$ augments the success probabilities of all types of relaying. The reason is that a larger $\tilde{\zeta}$ means more ambient energy resources, and thus more transmit power in either the WPR mode or APR mode. When $\tilde{\zeta}$ is relatively large, (e.g., above 2000/km²), the pure ABR outperforms the pure WPR. The reason is that when the signal power from ambient emitters is strong, the transmit power of the pure WPR is mostly limited by its capacitor capacity while that of the pure ABR does not have such a limitation. In other words, P_{R}^{W} stops increasing with $\tilde{\zeta}$ once the capacitor is fully charged. By contrast, P_{R}^{A} keeps increasing with $\tilde{\zeta}$.

4.6.3 Impact of Normalized Capacitor Capacity ρ_C on Success Probability

In Fig. 4.7, we investigate the impact of the normalized capacitor capacity i.e., $\rho_C = \frac{E_C}{T}$. It can be found that the capacity of the capacitor has a considerable impact on the success probabilities of the hybrid relaying with ESAP and the pure WPR. The reason is that the capacitor capacity is directly related to the transmit power of the wireless-powered transmission. By contrast, \mathcal{S}_{ABR} remains steady with the variation of ρ_C , as the transmit power of the pure ABR is not related to the

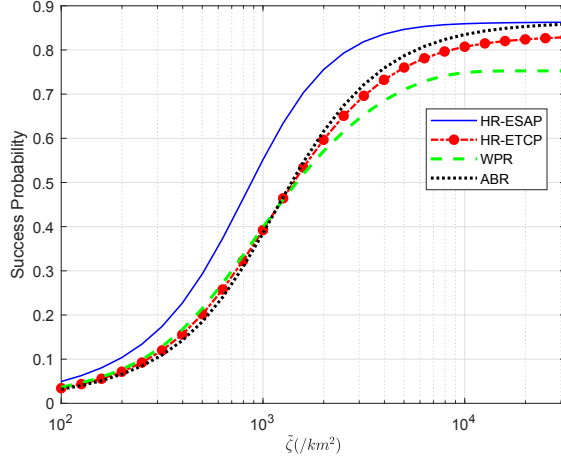


Figure 4.6: Success probability as a function of $\tilde{\zeta}$.

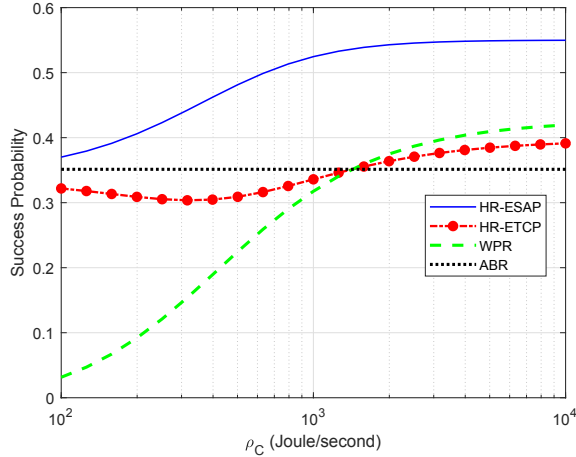


Figure 4.7: Success probability as a function of ρ_C .

capacitor capacity. Again, $\mathcal{S}_{\text{HR}}^{\text{ETCP}}$ approaches more closely to the better-performed one among \mathcal{S}_{ABR} and \mathcal{S}_{WPR} in most of the shown range. We note that both the success probabilities of the hybrid relaying with ESAP and the pure WPR are saturated when ρ_C becomes large. This implies that it is not necessary to equip a capacitor with oversized capacity for the hybrid relaying and the pure WPR. In practice, the capacitor capacity can be properly chosen to achieve a certain objective of success probability in the target network environment. Furthermore, by integrating ambi-

ent backscattering, the hybrid relaying with either ESAP or ETCP can relieve the requirement on capacitor capacity compared with the pure WPR.

4.6.4 Effect of Energy Harvesting Time Fraction ω on Success Probability and Ergodic Capacity

Fig. 4.8 evaluates how the energy harvesting time fraction ω of the relaying protocol affects the success probability. We observe that the success probabilities of WPR, ESAP and ETCP monotonically increase with ω . The reason is that larger ω not only decreases the probability of harvesting insufficient energy for the circuit power consumption but also increases the transmit power of WPR, resulting in higher success probabilities. By contrast, the variation of ω barely changes the success probability of ABR. This is because the energy demand for circuit power consumption of ABR is ultra-low which can be satisfied at a very small value of ω , and thus, further increasing ω does not cause a noticeable impact on the success probability.

Fig. 4.9 examines the impact of ω on the ergodic capacity performance. We first validate the analytical expressions of $\mathcal{C}_{\text{HR}}^{\text{ESAP}}$, $\mathcal{C}_{\text{HR}}^{\text{ETCP}}$, \mathcal{C}_{ABR} , and \mathcal{C}_{WPR} obtained in **Theorem 4.5.1**, **Theorem 4.5.2**, **Corollary 4**, and **Corollary 5**, respectively. It can be seen that our analytical results of ergodic capacity well match the Monte Carlo simulation results over a wide range of ω . In terms of the ergodic capacity, the hybrid relaying with ESAP still achieves the higher ergodic capacity than those of the pure ABR and the pure WPR. We can observe that the plots of the hybrid relaying with ESAP and the pure WPR are unimodal functions of ω within the shown range. This reveals that there can be an optimal value of ω to maximize the ergodic capacity of the hybrid relaying and the pure WPR. It is noted that the ergodic

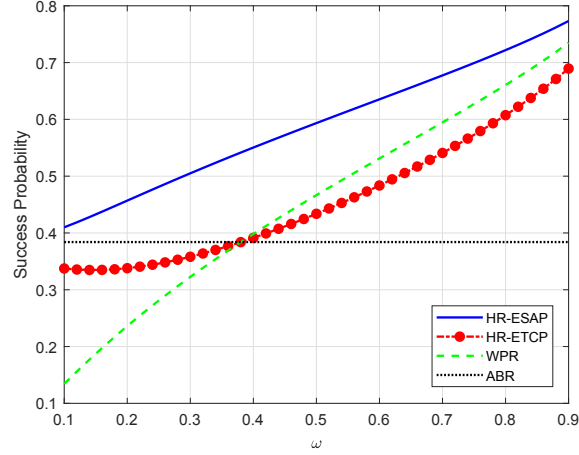


Figure 4.8: Success probability as a function of the energy harvesting time fraction ω .

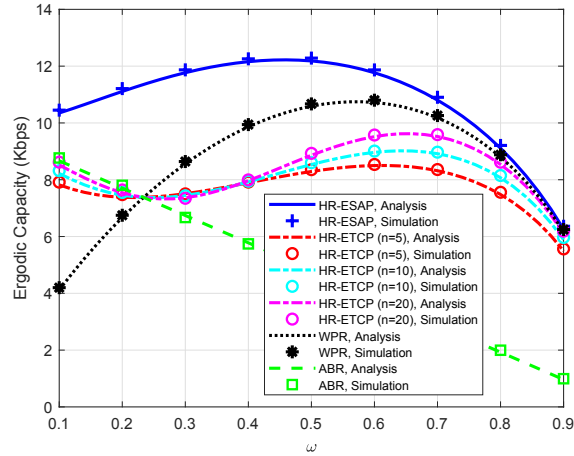


Figure 4.9: Ergodic capacity as a function of the energy harvesting time fraction ω .

capacity of the pure ABR is also a unimodal function of ω . Due to the ultra-lower circuit power consumption, the maximal \mathcal{C}_{ABR} is achieved at a value much smaller than the shown range, and thus we omit displaying it. Moreover, the performance gap between the hybrid relaying with ESAP and the pure WPR becomes larger with the decrease of the energy harvesting time fraction. This implies that the smaller the energy harvesting time, the greater the performance gain of the hybrid relaying with

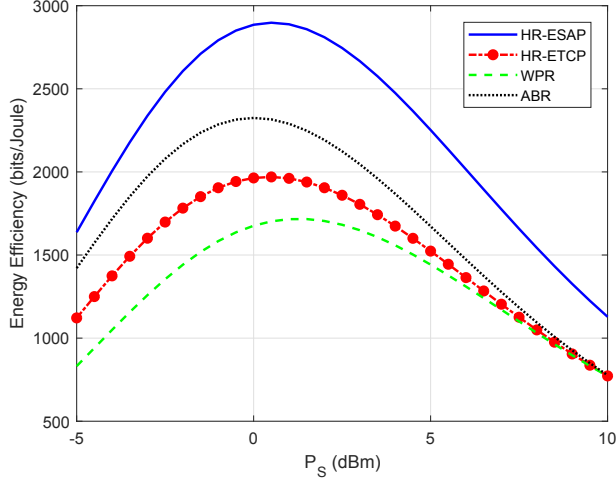


Figure 4.10: Energy efficiency as a function of P_S ($\tau_W = 10\tau_W$).

ESAP over the pure WPR. The reason is that ABR is adopted in ESAP when the harvested energy is deficient for active transmission. For ETCP, it can be seen that a longer exploration period may not always result in higher ergodic capacity. The reason is that ETCP favors higher success probability instead of ergodic capacity.

4.6.5 Impact of Transmit Power P_S on Energy Efficiency

Based on the analytical results of ergodic capacity, we also evaluate the energy efficiency (in bits/Joule) of the relaying system, defined as the ergodic capacity versus the transmit power of the source node, i.e., $\mathcal{E}_{HR} = \frac{C_{HR}}{P_S}$. As shown in Fig. 4.10, the ergodic capacities of all types of the relaying are unimodal functions of P_S . Specifically, increasing P_S at first enhances the energy efficiency because of an increase of the ergodic capacity. However, as P_S keeps increasing, the ergodic capacity increases at a rate lower than that of P_S , and thus, the energy efficiency starts to decrease.

4.6.6 Applications of Analytical Framework

Furthermore, we demonstrate applications of the derived analytical framework in optimizing system parameters. In energy-constrained communication systems, power allocation is a crucial design issue. Therefore, we consider two power allocation-related design problems: transmit power minimization and energy efficiency maximization. For the first problem, we minimize the transmit power of the source node with constraints on the minimum capacity by optimizing the energy harvesting time fraction ω . The formulation is expressed as follows:

$$\begin{aligned}
 \mathbf{P1} : \quad & \min_{\omega} \quad P_S \\
 \text{subject to} \quad & \mathbf{C1} : \mathcal{C}_{\text{HR}} \geq \mathcal{C}_{\text{HR}}^{\text{Target}}, \\
 & \mathbf{C2} : 0 \leq P_S \leq \bar{P}, \quad 0 \leq P_R^{\text{W}} \leq \bar{P}, \\
 & \mathbf{C3} : 0 \leq \omega \leq 1,
 \end{aligned}$$

where $\mathcal{C}_{\text{HR}}^{\text{Target}}$ denotes the target ergodic capacity and \bar{P} denotes the maximum transmit power for the source node and the relay node in the WPR mode. **C2** denotes the transmit power constraints for the source node and the hybrid relay, and **C3** denotes the time allocation constraint.

For the second problem, we maximize the energy efficiency of the relaying system with the reliability constraint that the success probability of the hybrid relaying should be above some target value, denoted as $\mathcal{S}_{\text{HR}}^{\text{Target}}$. The formulation is shown as

follows:

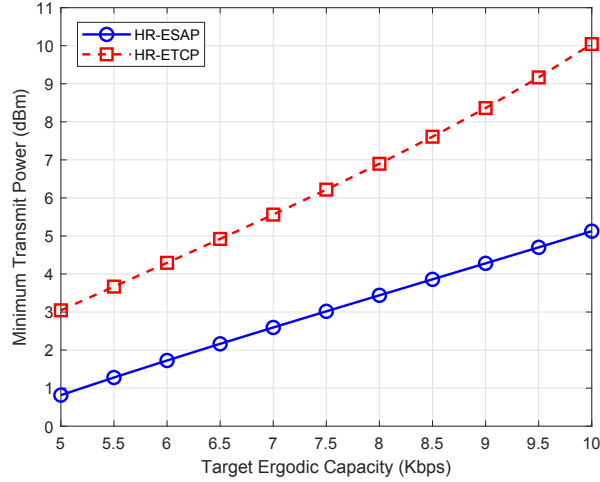
$$\begin{aligned}
\mathbf{P2} : \quad & \max_{\omega, P_S} \quad \mathcal{E}_{\text{HR}} = \frac{C_{\text{HR}}}{P_S} \\
\text{subject to } \quad & \mathbf{C1} : \quad \mathcal{S}_{\text{HR}} \geq \mathcal{S}_{\text{HR}}^{\text{Target}}, \\
& \mathbf{C2} : \quad 0 \leq P_S \leq \bar{P}, \quad 0 \leq P_R^{\text{W}} \leq \bar{P}, \\
& \mathbf{C3} : \quad 0 \leq \omega \leq 1,
\end{aligned}$$

where **C1** is the reliability requirement and **C2** and **C3** are the same as those in **P1**. Solving this problem provides us optimal choices of the energy harvesting time fraction ω and transmit power P_S .

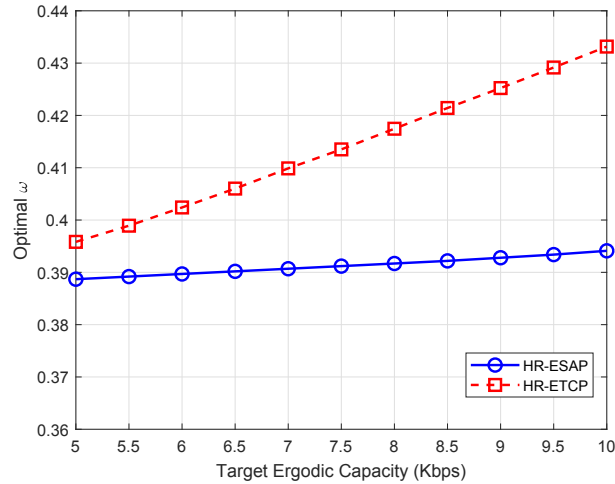
4.6.7 Numerical Solutions of Optimization Problems

Next, we numerically solve the formulated optimization problems. Fig. 4.11(a) and Fig. 4.11(b) illustrates the minimum transmit power allocation and corresponding ω and P_S as functions of the target ergodic capacity, respectively, for **P1**. As expected, the minimum transmit power is an increasing function of the target ergodic capacity. By utilizing the instantaneous CSI of active transmission, the hybrid relaying with ESAP achieves the same target ergodic capacity with much lower transmit power than that with ETCP.

Fig. 4.12(a) and Fig.4.12(b) demonstrate the maximum energy efficiency and the corresponding P_S and ω as functions of the target success probability, respectively, for **P2**. Again, the hybrid relaying with ESAP outperforms that with ETCP in terms of maximum energy efficiency due to higher achieved capacity. It is observed that with the increase of the target success probability the maximum energy efficiency first



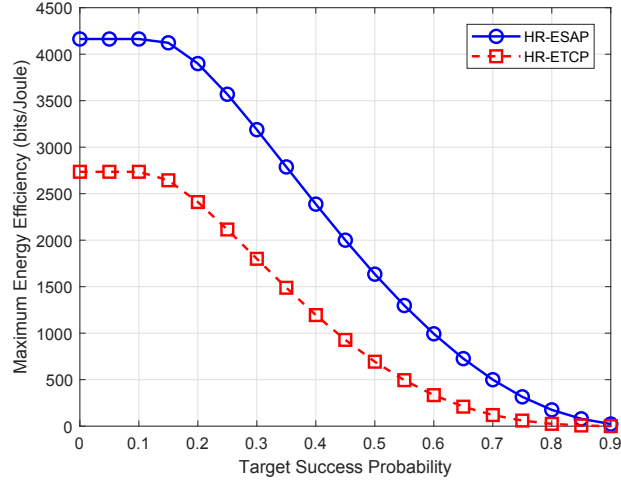
(a) Minimum transmit power as a function of target ergodic capacity.



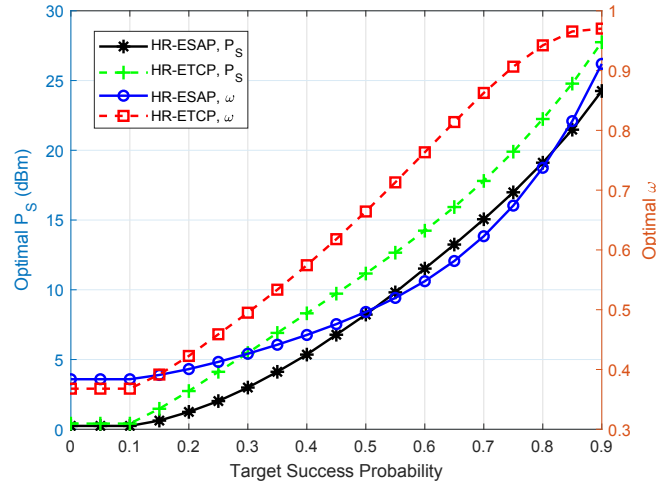
(b) Optimal ω as a function of target ergodic capacity.

Figure 4.11: Minimum transmit power and optimal energy harvesting time fraction with reliability constraints. ($\rho_Q = 2000/\text{km}^2$, $\bar{P} = 30$ dBm)

remains steady and then decreases. The reason is that larger P_S is required to ensure higher reliability, which may sacrifice energy efficiency. Moreover, the optimal ω increases with the reliability requirement. This can be understood straightforwardly that more harvested energy is needed for the hybrid relay to perform WPR to guar-



(a) Maximum energy efficiency as a function of target success probability.



(b) Optimal P_S and optimal ω as functions of target success probability.

Figure 4.12: Maximum energy efficiency and optimal energy harvesting time fraction and with reliability constraints. ($\rho_Q = 2000/\text{km}^2$, $\bar{P} = 30$ dBm)

antee high reliability. The results of the optimal resource allocation problem can be used as guidance for setting the hybrid relaying to balance the tradeoff between energy efficiency and reliability.

4.7 Conclusion

We have proposed a hybrid relaying paradigm that is capable of operating in either ambient backscatter relaying mode or wireless-powered relaying mode. Both relaying modes are based on but have different ways of, utilizing ambient RF signals. Therefore, how to switch between the two relaying modes under different network environment largely determines the performance of the hybrid relaying. To address this issue, we have devised two protocols for the hybrid relaying to perform operational mode selection with and without instantaneous CSI of active transmission. Considering the use of the hybrid relaying in a dual-hop relay system with spatially randomly located ambient emitters and interferers, we have derived the end-to-end success probabilities and ergodic capacity of the system under different mode selection protocols based on stochastic geometry analysis. We have demonstrated analytically and numerically the superiority of the hybrid relaying over the pure wireless-powered relaying and the pure ambient backscatter relaying, as the proposed mode selection protocols effectively select the proper operation to adapt to the system environment. The analytical results reveal the impacts of different system parameters on the studied performance metrics and allow us to optimize the system parameters based on the objective.

4.8 Appendix

4.8.1 Proof of Theorem 1

Proof. According to the criterion of ESAP described in Section 4.3, we have the probability that the hybrid relay is in the WPR mode and the ABR mode, respec-

tively, expressed as

$$\mathbb{P}[M_{\text{ESAP}} = \text{W}] = \mathbb{P}[\nu_{\text{R}} > \tau_{\text{W}}, E_{\text{R}} > E_{\text{W}}, \nu_{\text{D}}^{\text{W}} > \tau_{\text{W}}], \quad (4.29)$$

$$\begin{aligned} \text{and } \mathbb{P}[M_{\text{ESAP}} = \text{A}] &= \mathbb{P}[\nu_{\text{R}} > \tau_{\text{W}}, E_{\text{R}} > E_{\text{W}}, \nu_{\text{D}}^{\text{W}} \leq \tau_{\text{W}}] \\ &\quad + \mathbb{P}[\nu_{\text{R}} > \tau_{\text{W}}, E_{\text{W}} \geq E_{\text{R}} > E_{\text{A}}]. \end{aligned} \quad (4.30)$$

By inserting (4.29) and (4.30) into (4.6), we have

$$\begin{aligned} \mathcal{S}_{\text{HR}}^{\text{ESAP}} &= \mathbb{P}[\underbrace{\nu_{\text{R}} > \tau_{\text{W}}, \nu_{\text{D}}^{\text{W}} > \tau_{\text{W}}, E_{\text{R}} > E_{\text{W}}}_{\mathcal{S}_{\text{W}}^{\text{ESAP}}}] \\ &\quad + \underbrace{\mathbb{P}[\nu_{\text{R}} > \tau_{\text{W}}, \nu_{\text{D}}^{\text{A}} > \tau_{\text{A}}, \nu_{\text{D}}^{\text{W}} \leq \tau_{\text{W}}, E_{\text{R}} > E_{\text{W}}] + \mathbb{P}[\nu_{\text{R}} > \tau_{\text{W}}, \nu_{\text{D}}^{\text{A}} > \tau_{\text{A}}, E_{\text{W}} \geq E_{\text{R}} > E_{\text{A}}]}_{\mathcal{S}_{\text{A}}^{\text{ESAP}}}, \end{aligned} \quad (4.31)$$

where $\mathcal{S}_{\text{W}}^{\text{ESAP}}$ ($\mathcal{S}_{\text{A}}^{\text{ESAP}}$) represents the joint probability that the transmission is successful and the hybrid relay is in the WPR (ABR) mode under ESAP. We first obtain $\mathcal{S}_{\text{W}}^{\text{ESAP}}$ as follows:

$$\begin{aligned} \mathcal{S}_{\text{W}}^{\text{ESAP}} &= \mathbb{P}\left[h_{\text{S,R}} > \frac{d_{\text{S,R}}^{\mu} \tau_{\text{W}} (I_{\text{R}} + \sigma^2)}{P_{\text{S}}}, h_{\text{R,D}} > \frac{d_{\text{R,D}}^{\mu} \tau_{\text{W}} (I_{\text{D}} + \sigma^2)}{P_{\text{R}}^{\text{W}}}, \omega \beta T Q_{\text{R}} > E_{\text{W}}\right] \\ &\stackrel{\text{(a)}}{=} \mathbb{E}\left[\exp\left(-\frac{d_{\text{S,R}}^{\mu} \tau_{\text{W}} (I_{\text{R}} + \sigma^2)}{P_{\text{S}}}\right) \exp\left(-\frac{d_{\text{R,D}}^{\mu} \tau_{\text{W}} (I_{\text{R}} + \sigma^2)}{P_{\text{R}}^{\text{W}}}\right) \mathbf{1}_{\{Q_{\text{R}} > e_{\text{W}}\}}\right], \end{aligned} \quad (4.32)$$

where (a) follows the complementary CDF of the exponential random variable, i.e., $\mathbb{P}[h > x] = \exp(-x)$ for $h \sim \exp(1)$

With quasi-static interference, the relay and the destination nodes are affected

by spatially and temporally correlated interference imposed by the same ambient interferers Φ within the same time slot. Therefore, I_R and I_D are correlated. Let $\mathcal{L}_{I_R, I_D}(s_1, s_2) = \mathbb{E}[\exp(-s_1 I_R - s_2 I_D)]$ denote the Laplace transform of joint PDF of I_R and I_D . We can express $\mathcal{S}_W^{\text{ESAP}}$ as follows

$$\mathcal{S}_W^{\text{ESAP}} = \mathbb{E} \left[\exp \left(-\frac{d_{S,R}^\mu \tau_W \sigma^2}{P_S} - \frac{d_{R,D}^\mu \tau_W \sigma^2}{P_R^W} \right) \mathcal{L}_{I_R, I_D} \left(\frac{d_{S,R}^\mu \tau_W}{P_S}, \frac{d_{R,D}^\mu \tau_W}{P_R^W} \right) \mathbf{1}_{\{Q_R > \varrho_W\}} \right], \quad (4.33)$$

where the Laplace transform can be calculated as

$$\begin{aligned} & \mathcal{L}_{I_R, I_D} \left(\frac{d_{S,R}^\mu \tau_W}{P_S}, \frac{d_{R,D}^\mu \tau_W}{P_R^W} \right) \\ &= \mathbb{E}_{\Phi, h_{j,R}, h_{j,D}} \left[\exp \left(-\frac{d_{S,R}^\mu \tau_W}{P_S} \sum_{j \in \Phi} \frac{P_T h_{j,R}}{d_{j,R}^\mu} - \frac{d_{R,D}^\mu \tau_W}{P_R^W} \sum_{j \in \Phi} \frac{P_T h_{j,D}}{d_{j,D}^\mu} \right) \right] \\ &\stackrel{(b)}{=} \mathbb{E}_{\Phi} \left[\prod_{j \in \Phi} \left(1 + \frac{P_T d_{S,R}^\mu \tau_W}{P_S d_{j,R}^\mu} \right)^{-1} \left(1 + \frac{P_T d_{R,D}^\mu \tau_W}{P_R^W d_{j,D}^\mu} \right)^{-1} \right] \\ &\stackrel{(c)}{=} \text{Det} \left(\text{Id} + \alpha \mathbb{G}_{\Phi}(\mathbf{x}, \mathbf{y}) \varphi_{\mathbf{x}} \left(d_{R,D}^\mu \tau_W (P_R^W)^{-1} \right) \varphi_{\mathbf{y}} \left(d_{R,D}^\mu \tau_W (P_R^W)^{-1} \right) \right)^{-\frac{1}{\alpha}}, \quad (4.34) \end{aligned}$$

where (b) follows the Laplace transform of an exponential random variable, i.e., $\mathcal{L}_h(Z) = (1 + Z)^{-1}$ for $h \sim \mathcal{E}(1)$, and (c) takes the average over the α -GPP Φ by applying Proposition 1.

By inserting (4.34) into (4.33) we have the following expression after some math-

ematical manipulations.

$$\begin{aligned}
& \mathcal{S}_W^{\text{ESAP}} \\
&= \exp(-\kappa(\tau_W)\sigma^2) \left(\text{Det} \left(\text{Id} + \alpha \mathbb{G}_\Phi(\mathbf{x}, \mathbf{y}) \varphi_{\mathbf{x}}(\ell(\tau_W, \rho_C - \rho_W)) \varphi_{\mathbf{y}}(\ell(\tau_W, \rho_C - \rho_W)) \right) \right)^{-\frac{1}{\alpha}} \\
&\times \exp\left(-\ell(\tau_W, \rho_C - \rho_W)\sigma^2\right) \left(1 - F_{Q_R}(\varrho_C)\right) + \int_{\varrho_W}^{\varrho_C} \exp\left(-\ell(\tau_W, \omega\beta q - \rho_W)\sigma^2\right) \\
&\times \text{Det} \left(\text{Id} + \alpha \mathbb{G}_\Phi(\mathbf{x}, \mathbf{y}) \varphi_{\mathbf{x}}(\ell(\tau_W, \omega\beta q - \rho_W)) \varphi_{\mathbf{y}}(\ell(\tau_W, \omega\beta q - \rho_W)) \right)^{-\frac{1}{\alpha}} f_{Q_R}(q) dq. \quad (4.35)
\end{aligned}$$

Subsequently, we continue to derive $\mathcal{S}_A^{\text{ESAP}}$ as follows:

$$\begin{aligned}
\mathcal{S}_A^{\text{ESAP}} &= \mathbb{P} \left[h_{S,R} > \frac{\tau_W d_{S,R}^\mu (I_R + \sigma^2)}{P_S}, \tilde{h}_{R,D} > \frac{d_{R,D}^\mu \tilde{\sigma}^2 \tau_A}{\eta \xi Q_R}, E_W \geq \omega \beta T Q_R > E_A \right] \\
&+ \mathbb{P} \left[h_{S,R} > \frac{d_{S,R}^\mu \tau_W (I_R + \sigma^2)}{P_S}, \tilde{h}_{R,D} > \frac{d_{R,D}^\mu \tilde{\sigma}^2 \tau_A}{\eta \xi Q_R}, h_{R,D} \leq \frac{d_{R,D}^\mu \tau_W (I_D + \sigma^2)}{P_R^W}, \omega \beta T Q_R > E_W \right]. \\
&\stackrel{(e)}{=} \exp(-\kappa(\tau_W)\sigma^2) \left(\text{Det} \left(\text{Id} + \alpha \mathbb{G}_\Phi(\mathbf{x}, \mathbf{y}) \psi_{\mathbf{x}}(\kappa(\tau_W)) \psi_{\mathbf{y}}(\kappa(\tau_W)) \right) \right)^{-\frac{1}{\alpha}} \int_{\varrho_A}^{\infty} \delta(q) f_{Q_R}(q) dq \\
&- \chi_A(\tau_W, \rho_C - \rho_W) \int_{\varrho_C}^{\infty} \delta(q) f_{Q_R}(q) dq - \int_{\varrho_W}^{\varrho_C} \chi_A(\tau_W, \omega\beta q - \rho_W) \delta(q) f_{Q_R}(q) dq, \quad (4.36)
\end{aligned}$$

where (e) follows similar derivation steps of $\mathcal{S}_W^{\text{ESAP}}$ in (4.35) and $\chi_A(v, p)$ has been defined in (4.8).

Finally, by plugging (4.35) and (4.36) into (4.31), we have $\mathcal{S}_{\text{HR}}^{\text{ESAP}}$ expressed in (4.7). ■

4.8.2 Proof of Corollary 2

Proof. The case when the ambient emitters and interferers are distributed following PPPs can be modeled as a special case of our adopted α -GPP when $\alpha \rightarrow \infty$. In

particular, by using the expansion [57]

$$\text{Det}(\text{Id} + \alpha \mathbb{B}_\Phi(s))^{-\frac{1}{\alpha}} \xrightarrow{\alpha \rightarrow 0} \exp\left(-\int_{\mathbb{O}} \mathbb{B}_\Phi(\mathbf{x}, \mathbf{x}) d\mathbf{x}\right), \quad (4.37)$$

we can simplify the Fredholm determinant in (4.9) as follows when $\alpha \rightarrow \infty$, $\tilde{\alpha} \rightarrow \infty$, and $\mu = 4$:

$$\begin{aligned} \text{Det}\left(\text{Id} + \alpha \mathbb{B}_\Phi(\kappa(\tau_W))\right)^{-\frac{1}{\alpha}} &= \exp\left(-2\pi\zeta \int_0^{R \rightarrow \infty} \left(1 - \left(1 + \frac{d_{S,R}^4 \tau_W P_T}{P_S r^4}\right)^{-1}\right) r dr\right) \\ &= \exp\left(-\frac{\pi^2 \zeta}{2} \sqrt{\frac{d_{S,R}^4 \tau_W P_T}{P_S}}\right). \end{aligned} \quad (4.38)$$

Similarly, following the expansion in (4.37), $f_{Q_R}(q)$ can be simplified as follows:

$$\begin{aligned} f_{Q_R}(q) &= \mathcal{L}^{-1}\left\{\exp\left[-2\pi\tilde{\zeta} \int_0^{R \rightarrow \infty} \frac{r}{1+r^4(s\tilde{P}_T)^{-1}} dr\right]\right\}(q) \\ &= \mathcal{L}^{-1}\left\{\exp\left(-\frac{\pi^2}{2}\tilde{\zeta}\sqrt{s\tilde{P}_T}\right)\right\}(q) \\ &\stackrel{(f)}{=} \frac{1}{2\pi i} \lim_{L \rightarrow \infty} \int_{N-iL}^{N+iL} \exp(qs) \exp\left(-\frac{\pi^2}{2}\tilde{\zeta}\sqrt{s\tilde{P}_T}\right) ds \\ &\stackrel{(g)}{=} \frac{1}{\pi} \int_0^\infty \exp(-qt) \left[\frac{\exp\left(\frac{i}{2}\pi^2\tilde{\zeta}\sqrt{t\tilde{P}_T}\right) - \exp\left(-\frac{i}{2}\pi^2\tilde{\zeta}\sqrt{t\tilde{P}_T}\right)}{2i}\right] dt \\ &\stackrel{(h)}{=} \frac{1}{\pi} \int_0^\infty \exp(-qt) \sin\left(\frac{1}{2}\pi^2\tilde{\zeta}\sqrt{t\tilde{P}_T}\right) du = \frac{1}{4} \left(\frac{\pi}{q}\right)^{\frac{3}{2}} \tilde{\zeta}\sqrt{\tilde{P}_T} \exp\left(-\frac{\pi^4\tilde{\zeta}^2\tilde{P}_T}{16q}\right), \end{aligned} \quad (4.39)$$

where the inverse Laplace transform is converted in step (f) into a complex plane according to Mellin's inverse formula, and N is a fixed constant greater than the real parts of the singularities of $\exp\left(-\frac{\pi^2}{2}\tilde{\zeta}\sqrt{s\tilde{P}_T}\right)$, (g) uses the Bromwich inversion theorem with a modified contour, and (h) holds as $\frac{\exp(ix) - \exp(-ix)}{2i} = \sin(x)$.

Finally, by plugging (4.38) and (4.39) into (4.9), we have \mathcal{S}_{ABR} in (4.14) after some mathematical manipulations. ■

4.8.3 Proof of Theorem 2

Proof. With ETCP, the mode selection of R is based on achieved performance in the initial $2n$ time slots instead of the current one. Therefore, the steady-state success probability of the hybrid relaying in a particular mode is independent of the mode selection probability. Recall that the hybrid relay under ETCP eventually selects the ABR mode when the number of successful transmissions in the ABR mode is higher than that in the WPR mode during the exploration period. According to this mode selection criterion, the corresponding success probability can be expressed as

$$\begin{aligned}
\mathcal{S}_{\text{HR}}^{\text{ETCP}} &= \mathbb{P}\left[\nu_{\text{R}} > \tau_{\text{W}}, \nu_{\text{D}}^{\text{W}} > \tau_{\text{W}}, E_{\text{R}} > E_{\text{W}}\right] \mathbb{P}\left[\text{M}_{\text{ETCP}} = \text{W}\right] \\
&\quad + \mathbb{P}\left[\nu_{\text{R}} > \tau_{\text{W}}, \nu_{\text{D}}^{\text{A}} > \tau_{\text{A}}, E_{\text{R}} > E_{\text{A}}\right] \mathbb{P}\left[\text{M}_{\text{ETCP}} = \text{A}\right] \\
&\quad + \frac{1}{2} \left(\mathbb{P}\left[\nu_{\text{R}} > \tau_{\text{W}}, \nu_{\text{D}}^{\text{W}} > \tau_{\text{W}}, E_{\text{R}} > E_{\text{W}}\right] + \mathbb{P}\left[\nu_{\text{R}} > \tau_{\text{W}}, \nu_{\text{D}}^{\text{A}} > \tau_{\text{A}}, E_{\text{R}} > E_{\text{A}}\right] \right) \\
&\quad \times \left(1 - \mathbb{P}\left[\text{M}_{\text{ETCP}} = \text{W}\right] - \mathbb{P}\left[\text{M}_{\text{ETCP}} = \text{A}\right] \right) \\
&= \frac{1}{2} (\mathcal{S}_{\text{WPR}} + \mathcal{S}_{\text{ABR}}) + \frac{1}{2} \left(\mathbb{P}\left[N_{\text{WPR}} > N_{\text{ABR}}\right] - \mathbb{P}\left[N_{\text{ABR}} > N_{\text{WPR}}\right] \right) \\
&\quad \times (\mathcal{S}_{\text{WPR}} - \mathcal{S}_{\text{ABR}}). \tag{4.40}
\end{aligned}$$

The number of successful transmissions in the ABR mode and that in the WPR mode are dependent on \mathcal{S}_{ABR} and \mathcal{S}_{WPR} , obtained in (4.9) and (4.15), respectively.

Based on these results, we have

$$\begin{aligned}
\mathbb{P}[N_{\text{ABR}} > N_{\text{WPR}}] &= \sum_{i=1}^n \binom{n}{i} \mathbb{P}[N_{\text{ABR}} = i] \sum_{j=1}^i \binom{n}{i-j} \mathbb{P}[N_{\text{WPR}} = i-j] \\
&= \sum_{i=1}^n \binom{n}{i} \mathcal{S}_{\text{ABR}}^i (1 - \mathcal{S}_{\text{ABR}})^{n-i} \sum_{j=1}^i \binom{n}{i-j} \mathcal{S}_{\text{WPR}}^{i-j} (1 - \mathcal{S}_{\text{WPR}})^{n-i+j}.
\end{aligned} \tag{4.41}$$

Similarly, we have

$$\mathbb{P}[N_{\text{WPR}} > N_{\text{ABR}}] = \sum_{i=1}^n \binom{n}{i} \mathcal{S}_{\text{WPR}}^i (1 - \mathcal{S}_{\text{WPR}})^{n-i} \sum_{j=1}^i \binom{n}{i-j} \mathcal{S}_{\text{ABR}}^{i-j} (1 - \mathcal{S}_{\text{ABR}})^{n-i+j}. \tag{4.42}$$

Then, by inserting (4.41) and (4.42) into (4.40), we have the expression of $\mathcal{S}_{\text{HR}}^{\text{ETCP}}$ in (4.18). ■

4.8.4 Proof of Theorem 3

Proof. Recall that, with ESAP, the probabilities of the hybrid relaying working in the WPR mode (i.e., $\mathbb{P}[\text{M} = \text{W}]$) and ambient backscatter mode (i.e., $\mathbb{P}[\text{M} = \text{A}]$) have been obtained in (4.29) and (4.30), respectively. By inserting (4.29) and (4.30) into the definition in (4.19), we have the ergodic capacity of the hybrid relaying with

ESAP as follows:

$$\begin{aligned}
\mathcal{C}_{\text{HR}}^{\text{ESAP}} &= \frac{1-\omega}{2} \left(\mathbb{E} \left[W \log_2(1+\nu) \mathbf{1}_{\{\nu_{\text{R}} > \tau_{\text{W}}, \nu_{\text{D}}^{\text{W}} > \tau_{\text{W}}, E_{\text{R}} > E_{\text{W}}\}} \right] \right. \\
&\quad + C_{\text{A}} \left(\mathbb{P} \left[\nu_{\text{R}} > \tau_{\text{W}}, \nu_{\text{D}}^{\text{A}} > \tau_{\text{A}}, \nu_{\text{D}}^{\text{W}} \leq \tau_{\text{W}}, E_{\text{R}} > E_{\text{W}} \right] \right. \\
&\quad \left. \left. + \mathbb{P} \left[\nu_{\text{R}} > \tau_{\text{W}}, \nu_{\text{D}}^{\text{A}} > \tau_{\text{A}}, E_{\text{W}} \geq E_{\text{R}} > E_{\text{A}} \right] \right) \right) \\
&= \frac{1-\omega}{2} \left(\mathbb{E} \left[W \log_2(1+\nu) \mathbf{1}_{\{\nu_{\text{R}} > \tau_{\text{W}}, \nu_{\text{D}}^{\text{W}} > \tau_{\text{W}}, E_{\text{R}} > E_{\text{W}}\}} \right] + C_{\text{A}} \mathcal{S}_{\text{A}}^{\text{ESAP}} \right), \quad (4.43)
\end{aligned}$$

where $\mathcal{S}_{\text{A}}^{\text{ESAP}}$ has been obtained in (4.36).

The first term in the brackets of (4.43) can be calculated as

$$\begin{aligned}
&\mathbb{E} \left[W \log_2(1+\nu) \mathbf{1}_{\{\nu_{\text{R}} > \tau_{\text{W}}, \nu_{\text{D}}^{\text{W}} > \tau_{\text{W}}, E_{\text{R}} > E_{\text{W}}\}} \right] \\
&\stackrel{\text{(h)}}{=} W \int_0^\infty \mathbb{P} \left[\log_2(1+\nu) \mathbf{1}_{\{\nu_{\text{R}} > \tau_{\text{W}}, \nu_{\text{D}}^{\text{W}} > \tau_{\text{W}}, E_{\text{R}} > E_{\text{W}}\}} > t \right] dt \\
&\stackrel{\text{(i)}}{=} \frac{W}{\ln(2)} \int_{\tau_{\text{W}}}^\infty \mathbb{P} \left[\nu > v, \omega T \beta Q_{\text{R}} > E_{\text{W}} \right] \frac{1}{1+v} dv \\
&= \frac{W}{\ln(2)} \int_{\tau_{\text{W}}}^\infty \mathbb{P} \left[\min(\nu_{\text{R}}, \nu_{\text{D}}^{\text{W}}) > v, Q_{\text{R}} > \varrho_{\text{W}} \right] \frac{1}{1+v} dv \\
&= \frac{W}{\ln(2)} \int_{\tau_{\text{W}}}^\infty \mathbb{P} \left[\nu_{\text{R}} > v, \nu_{\text{D}}^{\text{W}} > v, Q_{\text{R}} > \varrho_{\text{W}} \right] \frac{1}{1+v} dv \\
&\stackrel{\text{(j)}}{=} \frac{W}{\ln(2)} \int_{\tau_{\text{W}}}^\infty \exp(-\kappa(v)\sigma^2) \left(\chi_{\text{A}}(v, \rho_{\text{C}} - \rho_{\text{W}}) (1 - F_{Q_{\text{R}}}(\varrho_{\text{C}})) \right. \\
&\quad \left. + \int_{\varrho_{\text{W}}}^{\varrho_{\text{C}}} \chi_{\text{A}}(v, \omega\beta q - \rho_{\text{W}}) f_{Q_{\text{R}}}(q) dq \right) \frac{1}{1+v} dv, \quad (4.44)
\end{aligned}$$

where (h) follows $\mathbb{E}[A] = \int_0^\infty \mathbb{P}[A > t] dt$ [52], (i) replaces t with $\log_2(1+v)$, and (j) follows the derivation of $\mathcal{S}_{\text{W}}^{\text{ESAP}}$ in (4.35) with τ_{W} replaced by v .

Finally, plugging (4.36) and (4.44) into (4.43) yields $\mathcal{C}_{\text{HR}}^{\text{ESAP}}$ in (4.20). ■

Chapter 5

On Coverage Probability With Type-II HARQ in Large-Scale Uplink IoT Networks

This Chapter¹ aims to study the performance of practical IoT networks with massive access.

5.1 Related Works

Analysis of retransmission schemes in large-scale networks is fundamental to the understanding of retransmission performance in practical communication systems. Only a few prior works have investigated HARQ schemes in large-scale cellular networks. Retransmission SIR loss in static networks is a key observation reported in the existing literature [46, 121, 122]. The SIR loss is due to temporal interference

¹A version of this chapter has been published in IEEE Wireless Communications Letter [120].

correlation because the initial transmission and the corresponding retransmission are affected by the same interferers. References [46] and [123] study both Type-I and Type-II HARQ-CC in downlink heterogeneous networks with and without BS cooperation, respectively. The focus of [122] is a unified analysis of Type-I HARQ in downlink cellular networks with different multiple-antenna configurations. These works highlight the presence of retransmission SIR loss, however, do not quantify its effect. The authors in [124] characterize the interference correlation in terms of Pearson's correlation coefficient [125] in a cluster Poisson network with Type-I HARQ and find that interferer clustering increases the interference correlation. Different from the above literature that target downlink transmissions without power control, reference [126] studies Type-I HARQ in uplink cellular networks under FPC. To the best of our knowledge, none of the existing literature has investigated Type-II HARQ-CC in uplink cellular networks.

5.2 System Model and Assumptions

We consider an uplink IoT network, where the APs (i.e., MTC gateways) Φ_A are distributed as a homogeneous PPP with spatial density ζ_A . We focus on the heavy load scenario with universal frequency reuse due to massive access and each AP is associated with a device uniformly distributed within the Voronoi cell of the AP on each resource block. This device distribution model is referred to as the user point process of type I in [127]. As the shape and area of the Voronoi cells of APs are dependent on their neighbouring cells, the resulted device point process Φ_D on each resource block conditioned on the Voronoi cells is not a PPP. Without loss of generality, we analyze the uplink transmission performance of a typical device,

denoted as d . The serving AP of the typical device, named tagged AP, is located at the origin. We employ the power-law path-loss model with path-loss exponent $\alpha > 2$ and small-scale fading. The small-scale fading gain, denoted as h_i , between a device $i \in \Phi_D$ and the tagged AP, is assumed to be an independent and identically distributed (i.i.d.) exponential random variable with unit mean. Moreover, $\mathbf{h} = \{h_i | i \in \Phi_D\}$ are assumed to be i.i.d. and vary across different transmission attempts.

A generalized fractional power control (GFPC) scheme [128] is adopted for uplink transmission, which sets the transmit power of any device as

$$P_i = \begin{cases} \varrho l_i^{\alpha\epsilon} & \text{if } \varrho l_i^{\alpha\epsilon} \leq \widehat{P}, \\ \bar{P} & \text{Otherwise,} \end{cases} \quad (5.1)$$

where ϱ is the baseline transmit power, l_i denotes the link distance between device i and its associated AP, $\epsilon \in [0, 1]$ is the path-loss compensation exponent (PCE), \widehat{P} and \bar{P} , respectively, denote the maximum transmit power and the enforced transmit power if P_i exceeds \widehat{P} . Note that the considered power control generalizes several power control schemes of interest. Specifically, the GFPC is equivalent to i) FPC [129] when $\widehat{P} = \infty$; ii) truncated fractional power control (TFPC) [129] when $\widehat{P} < \infty$ and $\bar{P} = 0$; iii) full channel inversion power control (FCIPC) [130] when $\epsilon = 1$ and $\widehat{P} = \infty$; and iv) no power control (NPC) when $\epsilon = 0$.

Due to the spatial correlation of the uplink devices, the exact characterization of the device distribution is not available. For tractability, we adopt the inhomogeneous PPP-based approximation introduced in [127] to approximate the distribution of the interfering devices $\Phi_I = \Phi_D \setminus \{d\}$. Specifically, Φ_I are modeled by an inhomogeneous PPP with density ζ_I . The functions of the density ζ_I , the PDF of l_0 , i.e., $f_{l_0}(r)$, and

that of $l_j, \forall j \in \Phi_I$, i.e., $f_{l_j}(l)$, are given, respectively, as $\zeta_I(d_j) = \zeta_A(1 - \exp(-C_1\zeta_A\pi d_j^2))$, $f_{l_0}(r) = 2C_2\pi\zeta_A r \exp(-C_2\zeta_A\pi r^2)$, and $f_{l_j|d_j}(r) = \frac{f_{l_0}(r)}{1 - \exp(-C_2\pi\zeta_A d_j^2)}$, $0 \leq r \leq d_j$, where $C_1 = \frac{12}{5}$, $C_2 = \frac{13}{10}$, and d_j denotes the distance between device j and the tagged AP.

The IoT network uses a Type-II HARQ-CC as the retransmission scheme. Specifically, the tagged AP requests one retransmission, denoted as R, if the receive signal-to-interference ratio (SIR)² of the initial transmission, denoted as T, is below a pre-defined threshold τ . Upon receiving the retransmission, the tagged AP performs decoding from the combined signals of the two transmissions based on MRC. This work focuses on studying the case with one retransmission round. The results with multiple retransmission round can be obtained by following the analytical approach adopted in this work straightforwardly. With the GFPC, the uplink SIR at the tagged AP either for an initial transmission or for the corresponding retransmission (if occurs) is calculated as

$$\eta^{(t)} = \frac{P_d h_d d_d^{-\alpha}}{\sum_{j \in \Phi_I} P_j h_j d_j^{-\alpha}} \stackrel{(a)}{=} \frac{h_d l_d^{\alpha(1-\epsilon)}}{\sum_{j \in \Phi_I} l_j^{\alpha\epsilon} h_j d_j^{-\alpha}}, \quad t \in \{T, R\}, \quad (5.2)$$

where (a) follows as $l_d = d_d$.

Let $\Phi_B^{(t)}, \Phi_D^{(t)}$ represent the realizations of the AP and the device point processes, respectively, during a transmission attempt $t \in \{T, R\}$ of the typical device. Note that $\Phi_A^{(T)}$ ($\Phi_U^{(T)}$) is identical to and different from $\Phi_A^{(R)}$ ($\Phi_U^{(R)}$), in the scenarios quasi-static interference (QSI) and fast-varying interference (FVI) [105], denoted as Q and F, respectively. In the following, the superscript (t) is dropped for the scenario with QSI and kept for the scenario with FVI to indicate the identity and difference of the

²We focus on the interference-limited regime, i.e., the noise power is ignored, as interference power dominates noise power in large-scale wireless networks.

Table 5.1: NOTATIONS.

Symbol	Definition
Φ_D, Φ_I	The point processes representing the uplink devices and the interfering devices, respectively
ϵ	Path-loss compensation exponent
ϱ	Baseline transmit power
\hat{P}	Maximum transmit power
\bar{P}	Enforced transmit power adopted when \hat{P} cannot be reached
ζ_I	Intensity of interfering devices
τ	SIR threshold

network realizations, respectively. Given the type of interference experienced, i.e., either Q or F, the coverage probability is defined as

$$\mathbf{C}^A := \underbrace{\mathbb{P}[\eta^{(T)} > \tau]}_{:=\mathbf{C}^{(T)}} + \mathbb{P}[\eta^{(R)} > \tau - \eta^{(T)}, \eta^{(T)} \leq \tau | \Xi^A], \quad (5.3)$$

where $A \in \{Q, F\}$ denotes the interference type indicator, $\mathbb{P}[\cdot]$ represents event probability, $\mathbf{C}^{(T)}$ represents the coverage probability of the initial transmission, $\Xi^Q := \{\Phi_A, \Phi_U\}$ and $\Xi^F := \{\Phi_A^{(T)}, \Phi_U^{(T)}, \Phi_A^{(R)}, \Phi_U^{(R)}\}$ are the sets of network realizations in the scenarios with QSI and FVI, respectively.

The main notations used in this chapter are summarized in Table 5.1.

5.3 Analysis of Uplink Coverage Probability

This section characterizes the expectation of the coverage probability of a typical uplink device considering different settings of the power control parameters for scenarios with QSI and FVI. We start with the general results as follows.

Theorem 5.3.1 *In uplink IoT networks, the coverage probability with GFPC under*

Rayleigh fading can be approximated by

$$\begin{aligned} \tilde{\mathbf{C}}_{\text{GFPC}}^{\text{Q}} = \tilde{\mathbf{C}}_{\text{GFPC}}^{(\text{T})} + \int_0^\tau \left(\int_0^{B_{\hat{P}}} \xi_{\tau,\eta,t} \left(\frac{u^{\frac{\alpha\epsilon}{2}}}{v^{\frac{\alpha}{2}}}, \frac{B_{\hat{P}}^{\frac{\alpha\epsilon}{2}}}{t^{\frac{\alpha\epsilon}{2}} v^{\frac{\alpha}{2}}} \right) dt \right. \\ \left. + \int_{B_{\hat{P}}}^\infty \xi_{\tau,\eta,t} \left(\frac{u^{\frac{\alpha\epsilon}{2}} t^{\frac{\alpha\epsilon}{2}}}{B_{\hat{P}}^{\frac{\alpha\epsilon}{2}} v^{\frac{\alpha}{2}}}, v^{-\frac{\alpha}{2}} \right) dt \right) d\eta, \end{aligned} \quad (5.4)$$

$$\begin{aligned} \tilde{\mathbf{C}}_{\text{GFPC}}^{(\text{F})} = \tilde{\mathbf{C}}_{\text{GFPC}}^{(\text{T})} + \int_0^\tau \left(\int_0^{B_{\hat{P}}} \exp \left(-t - \omega_{\tau-\eta,0,t} \left(\frac{u^{\frac{\alpha\epsilon}{2}}}{v^{\frac{\alpha}{2}}}, \frac{B_{\hat{P}}^{\frac{\alpha\epsilon}{2}}}{t^{\frac{\alpha\epsilon}{2}} v^{\frac{\alpha}{2}}} \right) \right) dt \right. \\ \times \int_0^{B_{\hat{P}}} \xi_{\eta,\eta,t} \left(\frac{u^{\frac{\alpha\epsilon}{2}}}{v^{\frac{\alpha}{2}}}, \frac{B_{\hat{P}}^{\frac{\alpha\epsilon}{2}}}{t^{\frac{\alpha\epsilon}{2}} v^{\frac{\alpha}{2}}} \right) dt + \int_{B_{\hat{P}}}^\infty \xi_{\eta,\eta,t} \left(\frac{u^{\frac{\alpha\epsilon}{2}} t^{\frac{\alpha\epsilon}{2}}}{B_{\hat{P}}^{\frac{\alpha\epsilon}{2}} v^{\frac{\alpha}{2}}}, v^{-\frac{\alpha}{2}} \right) dt \\ \left. \times \int_{B_{\hat{P}}}^\infty \exp \left(-t - \omega_{\tau-\eta,0,t} \left(\frac{u^{\frac{\alpha\epsilon}{2}} t^{\frac{\alpha\epsilon}{2}}}{B_{\hat{P}}^{\frac{\alpha\epsilon}{2}} v^{\frac{\alpha}{2}}}, v^{-\frac{\alpha}{2}} \right) \right) dt \right) d\eta, \end{aligned} \quad (5.5)$$

where $\tilde{\mathbf{C}}_{\text{GFPC}}^{(\text{T})}$ is

$$\begin{aligned} \tilde{\mathbf{C}}_{\text{GFPC}}^{(\text{T})} = \int_0^{B_{\hat{P}}} \exp \left(-t - \omega_{\tau,0,t} \left(\frac{u^{\frac{\alpha\epsilon}{2}}}{v^{\frac{\alpha}{2}}}, \frac{B_{\hat{P}}^{\frac{\alpha\epsilon}{2}}}{v^{\frac{\alpha}{2}} t^{\frac{\alpha\epsilon}{2}}} \right) \right) dt \\ + \int_{B_{\hat{P}}}^\infty \exp \left(-t - \omega_{\tau,0,t} \left(\frac{u^{\frac{\alpha\epsilon}{2}} t^{\frac{\alpha\epsilon}{2}}}{B_{\hat{P}}^{\frac{\alpha\epsilon}{2}} v^{\frac{\alpha}{2}}}, v^{-\frac{\alpha}{2}} \right) \right) dt, \end{aligned} \quad (5.6)$$

and $B_a = C_2 \pi \zeta_A \left(\frac{a}{\rho} \right)^{\frac{2}{\alpha\epsilon}}$, $\omega_{a,b,c}(x, y) = \mathcal{U}_{0,c}(Q_{a,b}(0, x)) + \mathcal{U}_{\frac{B_P}{c},c}(Q_{a,b}(x, y))$ and $\xi_{a,b,c}(x, y) = (\mathcal{U}_{0,c}(G_{a,b}(x, 0)) + \mathcal{U}_{\frac{B_P}{c},c}(G_{a,b}(y, x))) \exp(-t - \omega_{a,b,c}(x, y))$, $G_{a,b}(x, y) := x s_{a-b}(x) s_b(x)^2 - y s_{a-b}(y) s_b(y)^2$, $Q_{a,b}(x, y) := s_{a-b}(x) s_b(x) - s_{a-b}(y) s_b(y)$, $s_a(x) := \frac{1}{1+ax}$, $\mathcal{U}_{a,b}(x) := \frac{b^2}{C_2} \int_a^\infty \int_a^v x \varepsilon_b(u, v) du dv$, therein $\varepsilon_b(u, v) := e^{-ub} (1 - e^{-\frac{C_1}{C_2} vb}) (1 - e^{-vb})^{-1}$.

The proof of Theorem 5.3.1 is shown in Appendix 5.6.1.

We notice from (5.4) and (5.5) that in the case when $\hat{P} = \bar{P}$, $\mathbf{C}_{\text{GFPC}}^{\text{A}}$ is only affected by the product $\zeta_A \hat{P}^{\frac{2}{\alpha\epsilon}}$ for given α , ϵ and τ . This indicates that to guarantee a certain target coverage probability, \hat{P} can be set inversely proportional to ζ_A ensuring

a fixed value of $\zeta_A \widehat{P}^{\frac{2}{\alpha\epsilon}}$.

Next, we investigate the uplink coverage probability in some special cases of the GFPC. We present the analytical results in the following corollaries.

Corollary 7 *In uplink IoT networks, the coverage probability with FPC under Rayleigh fading can be approximated by*

$$\begin{aligned} \widetilde{\mathbf{C}}_{\text{FPC}}^{\text{Q}} = \widetilde{\mathbf{C}}_{\text{FPC}}^{(\text{T})} + \int_0^\tau \int_0^\infty \mathcal{U}_{0,t} \left(G_{\tau,\eta} \left(\frac{u^{\frac{\alpha\epsilon}{2}}}{v^{\frac{\alpha}{2}}}, 0 \right) \right) \\ \times \exp \left(-t - \mathcal{U}_{0,t} \left(Q_{\tau,\eta} \left(0, \frac{u^{\frac{\alpha\epsilon}{2}}}{v^{\frac{\alpha}{2}}} \right) \right) \right) dt d\eta, \end{aligned} \quad (5.7)$$

$$\begin{aligned} \widetilde{\mathbf{C}}_{\text{FPC}}^{\text{F}} = \widetilde{\mathbf{C}}_{\text{FPC}}^{(\text{T})} + \int_0^\tau \int_0^\infty \mathcal{U}_{0,t} \left(G_{\eta,\eta} \left(\frac{u^{\frac{\alpha\epsilon}{2}}}{v^{\frac{\alpha}{2}}}, 0 \right) \right) \exp \left(-t - \mathcal{U}_{0,t} \left(Q_{\eta,\eta} \left(0, \frac{u^{\frac{\alpha\epsilon}{2}}}{v^{\frac{\alpha}{2}}} \right) \right) \right) dt \\ \times \int_0^\infty \exp \left(-t - \mathcal{U}_{0,t} \left(Q_{\tau-\eta,0} \left(0, \frac{u^{\frac{\alpha\epsilon}{2}}}{v^{\frac{\alpha}{2}}} \right) \right) \right) dt d\eta, \end{aligned} \quad (5.8)$$

where $\widetilde{\mathbf{C}}_{\text{FPC}}^{(\text{T})} = \int_0^\infty \exp \left(-t - \mathcal{U}_{0,t} \left(Q_{\tau,0} \left(0, u^{\frac{\alpha\epsilon}{2}} v^{-\frac{\alpha}{2}} \right) \right) \right) dt$.

Moreover, in the special case of FCIPC, $\widetilde{\mathbf{C}}_{\text{FPC}}^{\text{A}}$ can be further simplified as

$$\widetilde{\mathbf{C}}_{\text{FCIPC}}^{\text{Q}} = \widetilde{\mathbf{C}}_{\text{FCIPC}}^{(\text{T})} + \int_0^\tau \mathcal{U}_{0,1} \left(G_{\tau,\eta} \left(\frac{u^{\frac{\alpha}{2}}}{v^{\frac{\alpha}{2}}}, 0 \right) \right) \exp \left(-\mathcal{U}_{0,1} \left(Q_{\tau,\eta} \left(0, \frac{u^{\frac{\alpha}{2}}}{v^{\frac{\alpha}{2}}} \right) \right) \right) d\eta, \quad (5.9)$$

$$\begin{aligned} \widetilde{\mathbf{C}}_{\text{FCIPC}}^{\text{S}} = \widetilde{\mathbf{C}}_{\text{FCIPC}}^{(\text{T})} + \int_0^\tau \mathcal{U}_{0,1} \left(G_{\eta,\eta} \left(\frac{u^{\frac{\alpha}{2}}}{v^{\frac{\alpha}{2}}}, 0 \right) \right) \\ \times \exp \left(-\mathcal{U}_{0,1} \left(Q_{\eta,\eta} \left(0, \frac{u^{\frac{\alpha}{2}}}{v^{\frac{\alpha}{2}}} \right) \right) - \mathcal{U}_{0,1} \left(Q_{\tau-\eta,0} \left(0, \frac{u^{\frac{\alpha}{2}}}{v^{\frac{\alpha}{2}}} \right) \right) \right) d\eta, \end{aligned} \quad (5.10)$$

where $\widetilde{\mathbf{C}}_{\text{FCIPC}}^{(\text{T})} = \exp \left(-\mathcal{U}_{0,1} \left(Q_{\tau,0} \left(0, \left(\frac{u}{v} \right)^{\frac{\alpha}{2}} \right) \right) \right)$.

Proof. The coverage probabilities with FPC can be obtained by assigning $\widehat{P} = \infty$ into the analytical expressions in (5.4) and (5.5). The coverage probabilities with FCIPC can be further obtained by letting $\epsilon = 1$ in (5.7) and (5.8). ■

With the analytical results in Theorem 5.3.1 and corollary 7, we have the following

observation.

Remark 1: In an ultra-dense network, i.e., when $\zeta_A \rightarrow \infty$, $\tilde{\mathbf{C}}_{\text{GFPC}}^{\text{A}} \sim \tilde{\mathbf{C}}_{\text{FPC}}^{\text{A}}$, which can be verified by letting $B_{\hat{P}} \rightarrow \infty$ as a direct result of $\zeta_A \rightarrow \infty$.

Corollary 8 *The uplink coverage probability with NPC (i.e., when $\epsilon = 0$) is approximated by*

$$\tilde{\mathbf{C}}_{\text{NPC}}^{\text{Q}} = \tilde{\mathbf{C}}_{\text{NPC}}^{(\text{T})} + \int_0^\tau \int_0^\infty \varphi_t(G_{\tau,\eta}(v^{-\frac{\alpha}{2}}, 0)) \exp\left(-t - \varphi_t(Q_{\tau,\eta}(0, v^{-\frac{\alpha}{2}}))\right) dt d\eta, \quad (5.11)$$

$$\tilde{\mathbf{C}}_{\text{NPC}}^{\text{F}} = \tilde{\mathbf{C}}_{\text{NPC}}^{(\text{T})} + \int_0^\tau \int_0^\infty \varphi_t(G_{\eta,\eta}(v^{-\frac{\alpha}{2}}, 0)) \exp\left(-t - \varphi_t(Q_{\eta,\eta}(0, v^{-\frac{\alpha}{2}}))\right) dt \\ \int_0^\infty \exp\left(-t - \varphi_t(Q_{\tau-\eta,0}(0, v^{-\frac{\alpha}{2}}))\right) dt d\eta, \quad (5.12)$$

where $\tilde{\mathbf{C}}_{\text{NPC}}^{(\text{T})} = \int_0^\infty \exp\left(-t - \varphi_t(Q_{\tau,0}(0, v^{-\frac{\alpha}{2}}))\right) dt$ and $\varphi_t(z) := \frac{t}{c_2} \int_0^\infty z(1 - e^{-\frac{c_1}{c_2}vt}) dv$.

Proof. The coverage probabilities with NPC can be obtained by assigning $\epsilon = 0$ into the analytical expressions in (5.4) and (5.5). ■

With the analytical results in Corollary 8, we have another scaling property of $\tilde{\mathbf{C}}_{\text{GFPC}}^{\text{A}}$ as follows.

Remark 2: Given the SIR threshold τ and ϵ , when $\zeta_A \rightarrow 0$, $\tilde{\mathbf{C}}_{\text{GFPC}} \sim \tilde{\mathbf{C}}_{\text{NPC}}$, which can be verified by letting $B_{\hat{P}} \rightarrow 0$ as a direct result of $\zeta_A \rightarrow 0$.

Moreover, in contrast to $\mathbf{C}_{\text{GFPC}}^{\text{A}}$ which is affected by the product $\zeta_A \hat{P}^{\frac{2}{\alpha\epsilon}}$, it can be observed from Corollary 7 and Corollary 8 that both the coverage probability with FPC and that with NPC are not affected by AP density ζ_A and maximum transmit power \hat{P} .

Corollary 9 *The uplink coverage probability with TFPC (i.e., when $\bar{P} = 0$) is ap-*

proximated by

$$\tilde{\mathbf{C}}_{\text{TFPC}}^{\text{Q}} = \tilde{\mathbf{C}}_{\text{TFPC}}^{(\text{T})} + \int_0^\tau \int_0^{B_{\hat{P}}} \xi_{\tau,\eta,t} \left(\frac{u^{\frac{\alpha\epsilon}{2}}}{v^{\frac{\alpha}{2}}}, 0 \right) dt d\eta, \quad (5.13)$$

and

$$\begin{aligned} \tilde{\mathbf{C}}_{\text{TFPC}}^{\text{F}} = \tilde{\mathbf{C}}_{\text{TFPC}}^{(\text{T})} + \int_0^\tau \int_0^{B_{\hat{P}}} \exp \left(-t - \omega_{\tau-\eta,0,t} \left(\frac{u^{\frac{\alpha\epsilon}{2}}}{v^{\frac{\alpha}{2}}}, 0 \right) \right) dt \\ \times \int_0^{B_{\hat{P}}} \xi_{\eta,\eta,t} \left(\frac{u^{\frac{\alpha\epsilon}{2}}}{v^{\frac{\alpha}{2}}}, 0 \right) dt d\eta, \end{aligned} \quad (5.14)$$

where $\tilde{\mathbf{C}}_{\text{TFPC}}^{(\text{T})} = \int_0^{B_{\hat{P}}} \exp \left(-t - \omega_{\tau,0,t} \left(u^{\frac{\alpha\epsilon}{2}} v^{-\frac{\alpha}{2}}, 0 \right) \right) dt$.

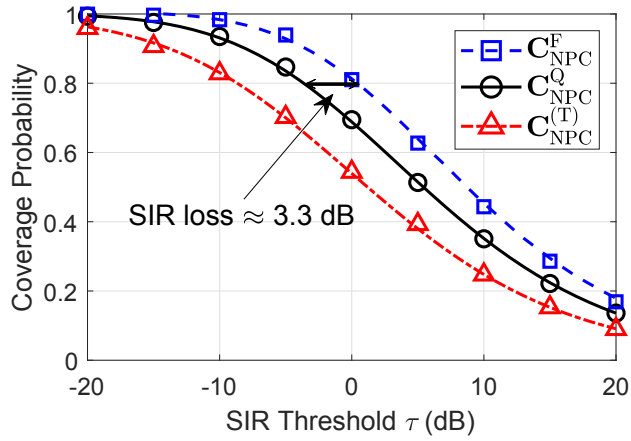
Proof. The coverage probabilities with TFPC can be obtained by assigning $\hat{P} = 0$ into the analytical expressions in (5.4) and (5.5). ■

5.4 Numerical Results

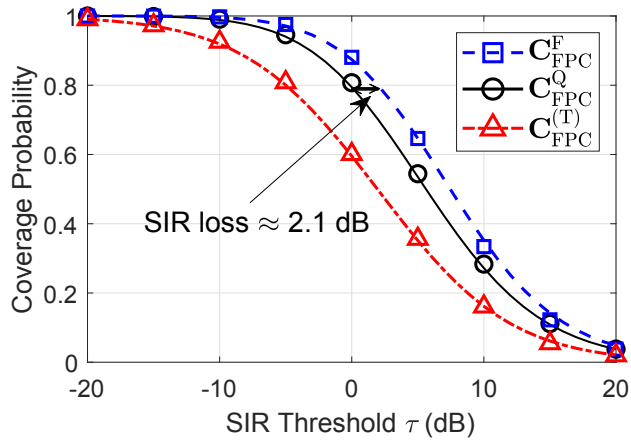
This section validates our analytical expressions through Monte Carlo simulations and evaluates the impact of system parameters. In the simulations, we set the AP density ζ_A as 10 APs/km², path-loss exponent α as 4, and baseline transmit power ϱ as -50 dBm, unless otherwise stated. The curves and the markers are used to represent the analytical results and the simulation results, respectively.

5.4.1 Impact of power control parameters ϵ , \hat{P} and \bar{P}

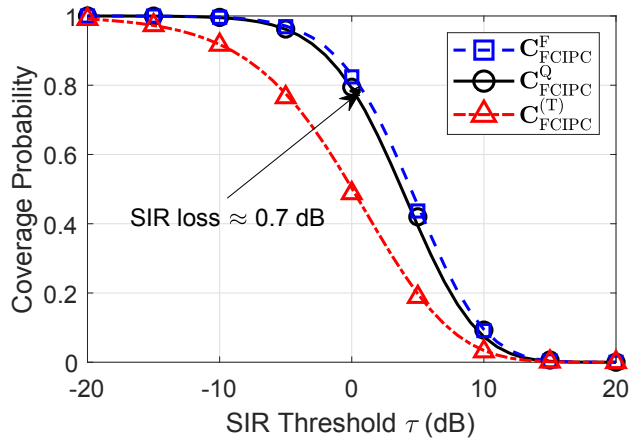
Fig. 5.1 compares the coverage probabilities achieved by the retransmission scheme with FVI and QSI and the initial transmission. The performance degradation of the retransmission scheme with QSI over that with FVI can be observed under



(a) $\epsilon = 0$ (NPC, Corollary 8)



(b) $\epsilon = 0.5$ (FPC, Corollary 7)



(c) $\epsilon = 1$ (FCIPC, Corollary 7)

Figure 5.1: Coverage probability with different values of ϵ ($\hat{P} = \infty$).

different settings of PCE. To quantify such performance degradation, we evaluate the *retransmission SIR loss*, defined as the ratio of the required SIR for achieving a target coverage probability with FVI to that with QSI, i.e., $\frac{f^{-1}(\mathbf{C}_{\text{FPC}}^{\text{F}}(\tau))}{f^{-1}(\mathbf{C}_{\text{QPC}}^{\text{F}}(\tau))}$, where $f^{-1}(\mathbf{C}_{\text{FPC}}^{\text{A}}(\tau))$ represents the inverse function of $\mathbf{C}_{\text{FPC}}^{\text{A}}(\tau)$. When the target coverage probability is 80%, the SIR loss is around 3.3 dB, 2.1 dB and 0.7 dB, when PCE ϵ equals 0, 0.5 and 1, respectively. This reveals that the SIR loss can be effectively mitigated by increasing the path-loss compensation. Another observation is that higher path-loss compensation increases the coverage probability with a low SIR threshold, however, decreases the coverage probability with a large SIR threshold. Thus, it is more beneficial to adopt a smaller path-loss compensation when the target SIR is large.

Fig. 5.2 illustrates the coverage probabilities when the maximum transmit power $\hat{P} = -20$ dBm, -10 dBm, 0 dBm. It can be observed that the coverage probability benefits from larger \hat{P} at high-coverage regime but benefits from smaller \hat{P} at the low-coverage regime. When the target coverage probability is 80%, the SIR loss is 4.3 dB, 3.7 dB and 1.7 dB, respectively. This implies that setting a larger maximum transmit power reduces the SIR loss, which agrees with the findings in Fig. 5.1.

In Fig. 5.3, we examine how the enforced transmit power \bar{P} affects the coverage probabilities when the SIR threshold is relatively small (i.e., $\tau = -5$ dB) and large (i.e., $\tau = 10$ dB). We find that larger \bar{P} increases the coverage probabilities when τ is small but decreases the coverage probabilities when τ is large. This can be understood from the fact that the SIR at the receiver is more dominated by the received signal power and the interference power when τ is small and large, respectively.

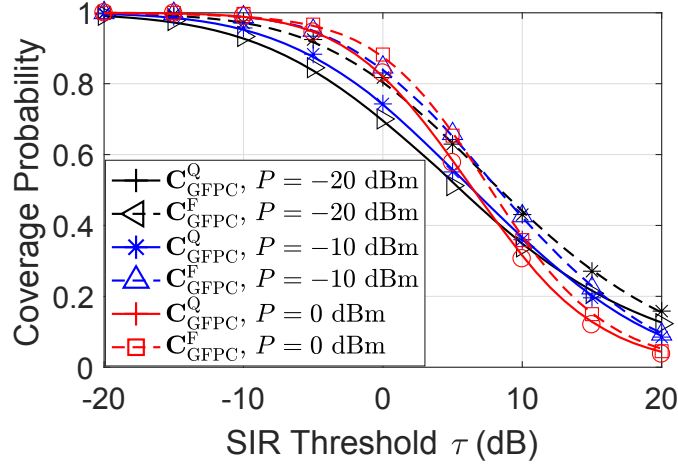


Figure 5.2: Coverage probability with different values of \hat{P} (for $\bar{P} = \hat{P} = P$).

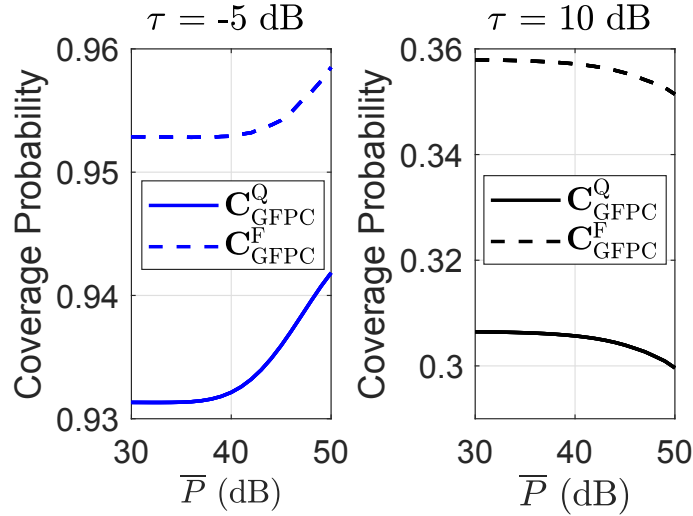


Figure 5.3: Coverage probability with different values of \bar{P} (for $\epsilon = 0.5$).

5.4.2 SIR gain of MRC

Next, we study the effect of MRC under FPC by comparing the coverage probability under retransmissions with and without MRC. The benefit of MRC is quantified in terms of *SIR gain* defined as $G_{MRC}^A := \frac{f^{-1}(\mathbf{C}^A(\tau))}{f^{-1}(\mathbf{T}^A(\tau))}$, where \mathbf{T}^A denotes the coverage probability under retransmission without MRC. Note that the coverage probability of

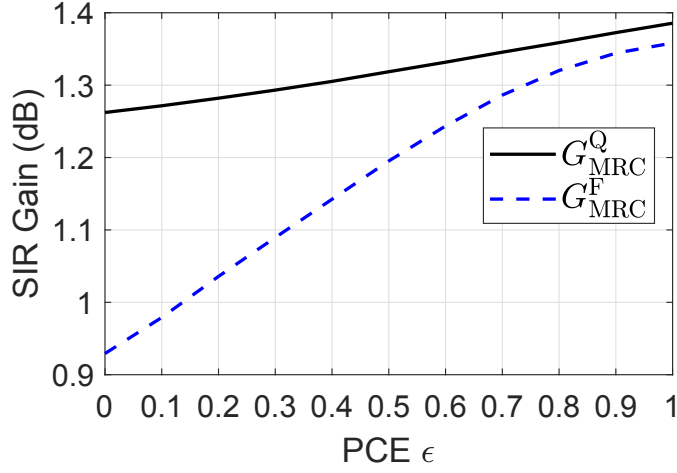


Figure 5.4: SIR gain of MRC with different values of ϵ (for $\tau = 0$ dB, $\hat{P} = \infty$).

retransmission without MRC under FPC can be generated from the analytical results in Corollary 7 with $G_{\tau,\eta}$ and $Q_{\tau,\eta}$ replaced by $G_{\tau+\eta,\eta}$, and $Q_{\tau+\eta,\eta}$, respectively, when $A = \text{Q}$, and with $Q_{\tau-\eta,0}$ replaced by $Q_{\tau,0}$ when $A = \text{F}$, (i.e., Type-I HARQ). Fig. 5.4 demonstrates the SIR gain of MRC under FPC when the target coverage probability is 80%. The results manifest that larger SIR gain of MRC can be achieved by increasing the transmit power. Moreover, the SIR gain of MRC is more pronounced in the scenario with QSI than that with FVI, especially when the transmit power is low.

Fig. 5.5 illustrates the SIR gains of MRC with QSI and FVI over a wide range of base station density. It can be seen that, with the increase of network density, both the SIR gain of MRC with QSI and that with FVI first increase then decrease to a steady regime when the base station density is high. Moreover, the gap between the SIR gains of MRC with QSI and FVI becomes meager in ultra-sparse and ultra-dense networks.

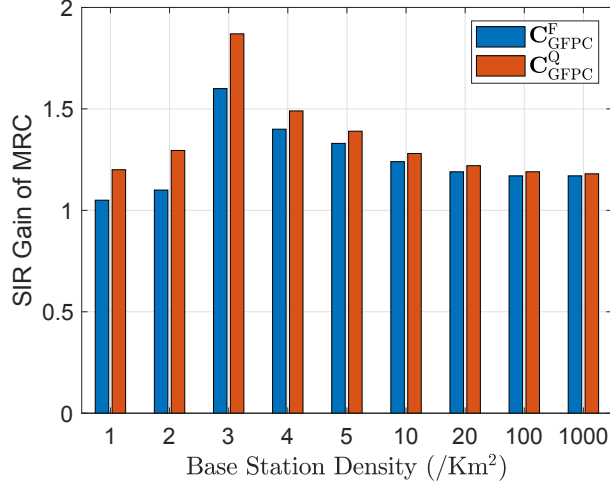


Figure 5.5: SIR gain of MRC with different base station density ($\epsilon = 1$, $\hat{P} = \bar{P} = 0$ dBm).

5.4.3 Extensions

We further evaluate the case with different maximum number of transmission times and the case with multiple antennas at APs by simulations.

Fig. 5.6 shows the coverage probability with different maximum number of transmissions N (including initial transmission and retransmissions). Our analysis can be extended to the case with $N \geq 3$ by utilizing the joint PDF of SIR of multiple transmissions. For example, when $N = 3$, we need to add to (5.3) one more term corresponding to the joint probability that the target SIR threshold τ is not satisfied by the first two transmissions but is satisfied after the third transmission. The derivation of the added term can be done by using the joint PDF of SIR of the first two transmissions. It can be seen that the first two retransmissions (i.e., $N = 2$ and $N = 3$) cause a remarkable increase in coverage probability. By contrast, the coverage probability exhibits a very limited gain when N is increased from 4 to 6, especially when the value of PCE is large (e.g., $\epsilon = 1$). This indicates that adopting an overlarge N is unnecessary. Given the PCE, N can be set as the minimum value

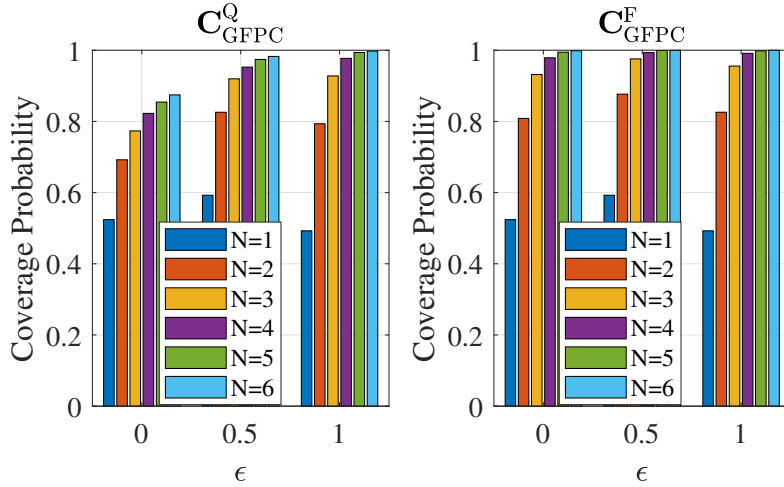


Figure 5.6: Coverage probability with different N ($\tau = 0$ dB).

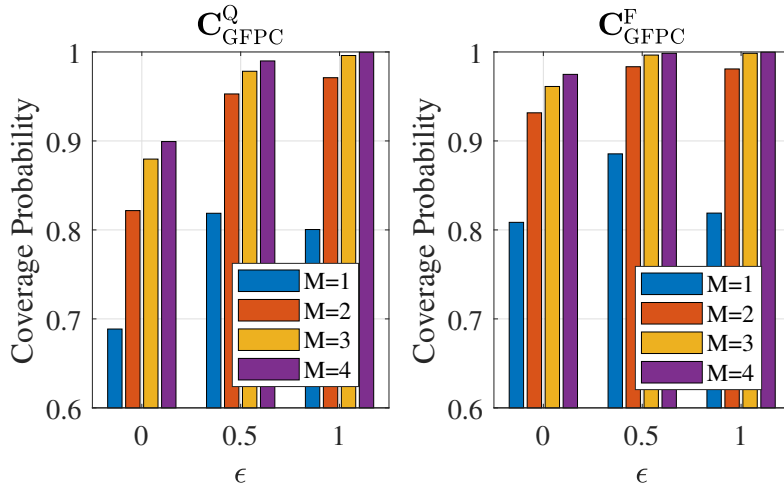


Figure 5.7: Coverage probability with different number of antennas ($\tau = 0$ dB).

to meet a target coverage probability.

Fig. 5.7 demonstrates the impact of the number of antennas per AP, denoted as M . Our analytical results can be extended to the case with $M > 1$. In this case, the exponentially distributed channel gain h_0 should be replaced by the *equivalent channel gain* of a single-input-multiple-output channel. As shown in [122], the equivalent channel gain follows a gamma distribution with shape parameter M and rate parameter 1. The most significant performance improvement can be achieved when

M is increased from 1 to 2. Moreover, adopting multiple antennas also mitigates the performance gap between the cases with QSI and FVI.

5.5 Conclusion

This letter presents a stochastic geometry analysis of a Type-II HARQ-CC retransmission scheme in uplink IoT networks with transmit power control. In particular, the uplink coverage probability in a large-scale IoT network is characterized in the scenarios of both QSI and FVI. Our study reveals the effects of different power control parameters on the retransmission SIR loss and the SIR gain achieved by MRC. In addition, the derived analytical expressions can be utilized to maximize the uplink coverage probability by optimizing the power control parameters.

5.6 Appendix

5.6.1 Proof of Theorem 5.3.1

Proof. From the definition in (5.3), the coverage probability can be expressed as

$$\mathbf{C}_{\text{GFPC}}^{\text{A}} = \mathbf{C}_{\text{GFPC}}^{(\text{T})} + \mathbb{E}[\mathbb{P}[\eta^{(\text{R})} > \tau - \eta^{(\text{T})} | \Xi^{\text{A}}] \mathbb{1}_{\{\eta^{(\text{T})} \leq \tau\}}],$$

where \mathbb{E} denotes the expectation operator, $\mathbb{1}_{\{\cdot\}}$ is the indicator function, $\mathbf{C}_{\text{GFPC}}^{(\text{T})}$ represents the coverage probability of an initial transmission, which is obtained as (5.6) following similar derivations to the proof of **Theorem 1** in [129], and the

second term in the above $\mathbf{C}_{\text{GFPC}}^{\text{A}}$ expression can be derived as

$$\begin{aligned} & \mathbb{E}_{\Xi^{\text{A}}, h^{(\text{R})}} \left[\mathbb{P} \left[\frac{h_0^{(\text{R})} l_0^{\alpha(\epsilon-1)}}{\sum_{j \in \Phi_I^{(\text{R})}} h_j^{(\text{R})} l_j^{\alpha\epsilon} d_j^{-\alpha}} > \tau - \eta^{(\text{T})} | \Xi^{\text{A}} \right] \mathbb{1}_{\{\eta^{(\text{T})} \leq \tau\}} \right] \\ & \stackrel{\text{(b)}}{=} \mathbb{E}_{\Xi^{\text{A}}} \left[\int_0^\tau \prod_{j \in \Phi_I^{(\text{R})}} \left(1 + (\tau - \eta^{(\text{T})}) \frac{l_0^\alpha l_j^{\alpha\epsilon}}{d_j^\alpha l_0^{\alpha\epsilon}} \right)^{-1} f_{\eta^{(\text{T})}}(\eta) d\eta \right], \end{aligned} \quad (5.15)$$

where (b) holds as $h_i, \forall i \in \Phi_D$ is exponentially distributed and $f_{\eta^{(\text{T})}}(\eta)$ represents the PDF of $\eta^{(\text{T})}$ calculated as

$$\begin{aligned} f_{\eta^{(\text{T})}}(\eta) &= \partial F_{\eta^{(\text{T})} | \Xi^{\text{A}}}(\eta) / \partial \eta \\ &= \frac{\partial \mathbb{P}[\eta^{(\text{T})} \leq \eta]}{\partial \eta} \\ &= \partial \left(1 - \prod_{j \in \Phi_I^{(\text{T})}} \left(1 + \eta l_0^{\alpha(1-\epsilon)} l_j^{\alpha\epsilon} d_j^{-\alpha} \right)^{-1} \right) / \partial \eta \\ &= \sum_{j \in \Phi_I^{(\text{T})}} \frac{l_0^{\alpha(1-\epsilon)} l_j^{\alpha\epsilon} d_j^{-\alpha}}{\left(1 + \eta l_0^{\alpha(1-\epsilon)} l_j^{\alpha\epsilon} d_j^{-\alpha} \right)^2} \prod_{j' \in \Phi_I^{(\text{T})} \setminus \{j\}} \left(1 + \eta \frac{l_0^\alpha l_{j'}^{\alpha\epsilon}}{d_{j'}^\alpha l_0^{\alpha\epsilon}} \right)^{-1}. \end{aligned} \quad (5.16)$$

By plugging (5.16) into (5.15), and applying the transformations $u = (\frac{l}{l_0})^2$ and $v = (\frac{x}{l_0})^2$ and the substitution $s_a(x) = (1 + ax)^{-1}$ and $g_a(x) = x(1 + ax)^{-2}$, we have $\mathbf{C}_{\text{GFPC}}^{\text{Q}}$ and $\mathbf{C}_{\text{GFPC}}^{\text{F}}$, respectively, as

$$\begin{aligned} \mathbf{C}_{\text{GFPC}}^{\text{Q}} &= \int_0^\tau \mathbb{E} \left[\sum_{j \in \Phi_I} g_\eta \left(\frac{l_0^\alpha l_j^{\alpha\epsilon}}{d_j^\alpha l_0^{\alpha\epsilon}} \right) s_{\tau-\eta} \left(\frac{l_0^\alpha l_j^{\alpha\epsilon}}{d_j^\alpha l_0^{\alpha\epsilon}} \right) \mathbb{E}_{\Xi^{\text{A}}} \left[\prod_{k \in \Phi_I \setminus \{j\}} s_\eta \left(\frac{l_0^\alpha l_k^{\alpha\epsilon}}{d_k^\alpha l_0^{\alpha\epsilon}} \right) s_{\tau-\eta} \left(\frac{l_0^\alpha l_k^{\alpha\epsilon}}{d_k^\alpha l_0^{\alpha\epsilon}} \right) \right] \right] d\eta, \\ &+ \int_0^\tau \mathbb{E}_{l_0} \left[2\pi \int_0^\infty x \zeta_I(x) \int_x^\infty g_\eta \left(\frac{l_0^\alpha l_k^{\alpha\epsilon}}{x^\alpha l_0^{\alpha\epsilon}} \right) s_{\tau-\eta} \left(\frac{l_0^\alpha l_k^{\alpha\epsilon}}{x^\alpha l_0^{\alpha\epsilon}} \right) f_{l_j}(l) dl dx \right. \\ &\quad \left. \times \underbrace{\mathbb{E}_{\Xi^{\text{A}}} \left[\prod_{k \in \Phi_I^{(\text{T})} \setminus \{j\}} s_\eta \left(\frac{l_0^\alpha l_k^{\alpha\epsilon}}{d_k^\alpha l_0^{\alpha\epsilon}} \right) s_{\tau-\eta} \left(\frac{l_0^\alpha l_k^{\alpha\epsilon}}{d_k^\alpha l_0^{\alpha\epsilon}} \right) \right]}_{:=\mathbf{S}^{\text{Q}}} \right] d\eta, \end{aligned} \quad (5.17)$$

and

$$\begin{aligned}
\mathbf{C}_{\text{GFPC}} = & \int_0^\tau \mathbb{E} \left[\sum_{j \in \Phi_I^{(\text{T})}} g_\eta \left(\frac{l_0^\alpha l_j^{\alpha\epsilon}}{d_j^\alpha l_0^{\alpha\epsilon}} \right) \mathbb{E}_{\Xi^A} \left[\prod_{j' \in \Phi_I^{(\text{T})} \setminus \{j\}} s_\eta \left(\frac{l_0^\alpha l_{j'}^{\alpha\epsilon}}{d_{j'}^\alpha l_0^{\alpha\epsilon}} \right) \prod_{k \in \Phi_I^{(\text{T})}} s_{\tau-\eta} \left(\frac{l_0^\alpha l_k^{\alpha\epsilon}}{d_k^\alpha l_0^{\alpha\epsilon}} \right) \right] \right] d\eta, \\
& \int_0^\tau \mathbb{E}_{l_0} \left[2\pi \int_0^\infty x \zeta_I(x) \int_x^\infty g_\eta \left(\frac{l_0^\alpha l_0^{\alpha\epsilon}}{x^\alpha l_0^{\alpha\epsilon}} \right) f_{l_j}(l) dl dx \right. \\
& \left. \times \underbrace{\mathbb{E}_{\Xi^A} \left[\prod_{\substack{j' \neq j \\ j' \in \Phi_I^{(\text{T})}} s_\eta \left(\frac{l_0^\alpha l_{j'}^{\alpha\epsilon}}{d_{j'}^\alpha l_0^{\alpha\epsilon}} \right) \right] \mathbb{E}_{\Xi^A} \left[\prod_{k \in \Phi_I^{(\text{T})}} s_{\tau-\eta} \left(\frac{l_0^\alpha l_k^{\alpha\epsilon}}{d_k^\alpha l_0^{\alpha\epsilon}} \right) \right]}_{:=\mathbf{S}^F} \right] d\eta, \quad (5.18)
\end{aligned}$$

where (c) applies the Campbell Mecke formula [125]. And by following the probability generating functional for a PPP, \mathbf{S}^Q and \mathbf{S}^F can be derived, respectively, as,

$$\mathbf{S}^Q = \exp \left(- \int_{\mathbb{R}^2} \zeta_I(x) \mathbb{E}_{l_k} \left[1 - s_{\tau-\eta} \left(\frac{l_0^\alpha l_k^{\alpha\epsilon}}{x^\alpha l_0^{\alpha\epsilon}} \right) s_\eta \left(\frac{l_0^\alpha l_k^{\alpha\epsilon}}{x^\alpha l_0^{\alpha\epsilon}} \right) \right] dx \right), \quad (5.19)$$

$$\begin{aligned}
\text{and } \mathbf{S}^F = & \exp \left(- \int_{\mathbb{R}^2} \zeta_I(x) \mathbb{E}_{l_{j'}} \left[1 - s_{\tau-\eta} \left(\frac{l_0^\alpha l_{j'}^{\alpha\epsilon}}{x^\alpha l_0^{\alpha\epsilon}} \right) \right] dx \right) \\
& \times \exp \left(- \int_{\mathbb{R}^2} \zeta_I(x) \mathbb{E}_{l_k} \left[1 - s_\eta \left(\frac{l_0^\alpha l_k^{\alpha\epsilon}}{x^\alpha l_0^{\alpha\epsilon}} \right) \right] dx \right). \quad (5.20)
\end{aligned}$$

Here, the interfering devices for the initial transmission and the retransmission are averaged over the same inhomogeneous PPP and two independent inhomogeneous PPPs for the cases with QSI and FVI, respectively.

Then, by averaging (5.17) and (5.18) based on $f_{l_0}(r)$, the final results in Theorem 5.3.1 can be obtained after some mathematical simplification. ■

Chapter 6

Conclusions and Future Research

6.1 Conclusion

This dissertation aims to design energy-efficient solutions to MTC in IoT and investigate the analytical performance of emerging IoT scenarios. In particular, we have proposed a hybrid communication paradigm and introduced operational protocols to solve the energy bottleneck of MTC devices. We have also devised operational protocols to hybrid cooperative relaying to improve the applicability and extend the limited transmission range of low-power MTC devices. Furthermore, we have analyzed the performance of massive uplink access in large-scale IoT networks with HARQ.

Chapter 3 proposes a hybrid communication paradigm with combined ambient backscattering and wireless-powered communication functions to enable sustainable communications among MTC devices. Since the radio signals for energy harvesting and for backscattering only come from the ambient, the performance of the hybrid M2M communications depends largely on the environment factors, e.g., distribu-

tion, spatial density, and transmission load of ambient energy sources. Two mode selection protocols have been designed for the hybrid transmitter, allowing a more flexible adaptation to the environment. Then, analytical models have been developed to characterize the impacts of the environment factors on the hybrid M2M communication performance. Together with extensive simulations, the analysis shows that the communication performance benefits from larger repulsion, transmission load and density of ambient energy sources. Furthermore, how different mode selection mechanisms affect the communication performance has been investigated.

Chapter 4 studies hybrid relaying strategy based on combined wireless-powered relaying and ambient backscatter relaying. In particular, the hybrid relay can harvest energy from RF signals and use the energy for active transmission. Alternatively, the hybrid relay can choose to perform ambient backscattering of incident RF signals for passive transmission. For the operation of the hybrid relaying, selecting a proper mode based on the network environment is the key to better relaying performance. Two mode selection protocols have been devised to coordinate between the active and passive relaying in the cases with and without instantaneous CSI of active transmission, respectively. In the former case, since the hybrid relay is aware of whether the two relaying modes are applicable for the current time slot based on the CSI, it selects active relaying if applicable due to higher capacity and selects passive relaying otherwise. In the latter case, the hybrid relay first explores the two relaying modes and commits to the mode that achieves more successful transmissions during the exploration period. With different mode selection protocols, the success probability and ergodic capacity of a dual-hop hybrid relaying system have been characterized considering the field of randomly located ambient transmitters. The analytical and the numerical results demonstrate the effectiveness of the mode selection protocols

in adapting the hybrid relaying into the network environment and reveal the impacts of system parameters on the performance of the hybrid relaying. As applications of the analytical framework which is computationally tractable, optimization problems based on the derived expressions have been formulated to optimize the system parameters with different objectives. The optimal solutions exhibit a tradeoff between the maximum energy efficiency and target success probability.

Chapter 5 studies uplink transmission in large-scale IoT networks with a Type-II HARQ-CC retransmission scheme, under which an unsuccessful transmission (if occurs) is combined with the corresponding retransmission through MRC. Based on stochastic geometry analysis, the uplink coverage probabilities are characterized under a generalized power control scheme in the scenarios with QSI and FVI, where the same and different interfering users, respectively, are present during the transmission and retransmission phase. Our analytical expressions reveal some scaling properties of the coverage probabilities and can be used to evaluate the SIR gain of MRC (i.e., the ratio of the required SIR for achieving a target coverage probability with MRC to that without MRC). We show that the SIR gain of MRC is more remarkable in the scenario with QSI compared to that with FVI. Moreover, the SIR gain of MRC can be mostly exploited by adopting full channel-inversion power control.

6.2 Future Direction

6.2.1 Hybrid M2M communications

Our first work studies the performance of the proposed hybrid M2M communications with a single antenna at the hybrid transmitter and receiver. The performance of the hybrid communications can be improved when multiple antennas are adopted.

Multiple antennas are expected to improve both the amount of harvested energy at the hybrid transmitter and channel gain between the hybrid transmitter and receiver. Characterizing the performance of hybrid communications in various cases of multi-antenna channels and study the scaling behavior with the number of antennas is a meaningful future direction.

Another extension is to study the system with multiple hybrid transmitter-receiver pairs. In such a scenario, the coordination among the transmissions plays a pivotal role in the system performance such as the instant success probability and system sum rate. Designing distributed mode selection protocols performed by individual hybrid transmitters based on the local information is a direction that worth exploring.

6.2.2 Hybrid relaying systems

Our second work considers that the hybrid relay adopts the harvest-use architecture, with which the harvested energy is either consumed immediately or lost in the current time slot. In practice, it is possible to accumulate the harvested energy to the subsequent time slots with an energy storage component. In this case, the instant success probability of the current time slot and the long-term success probability are different as the initial energy reserve at the beginning of each time slot may vary. Our analytical framework can be straightforwardly extended to derive the instant success probability by considering a given initial energy reserve. The long-term coverage probability can be obtained by resorting to the Markov chain based approaches [131], i.e., using a Markov chain to model the transition probability matrix of energy storage state and calculate the steady-state probabilities.

In the case with energy accumulation, the mode selection protocols also need to

be revisited by taking into account the initial energy of each time slot. The tradeoff between instant access through passive transmission at a low transmission rate and delayed access through active transmission at a higher transmission rate is a critical issue to be addressed in the design of the mode selection protocols.

Another interesting direction is to study the scenarios with the direct source-to-destination link in addition to the relaying links. In these scenarios, different cooperative combining techniques (e.g., MRC, selection combining, and equal gain combining) can be exploited to increase the diversity gain at the destination node. Our analytical framework can be extended to analyze the diversity gain of the hybrid relay.

6.2.3 Cellular IoT networks with retransmissions

Our third work considers traditional orthogonal multiple access techniques where each frequency band is only assigned to each device at a certain time block. Power-domain non-orthogonal multiple access (NOMA) [132] is a multiplexing technique that allows multiple users to simultaneously transmit on the same frequency band. The spectrum sharing is realized through superposition coding at the transmitter and successive interference cancellation at the receiver based on the power difference. Power-domain NOMA has demonstrated great potential to improve spectrum efficiency and is considered as an enabling technique to mitigate the spectrum deficiency issue of massive access over IoT networks [133]. Uplink IoT performance with NOMA and HARQ retransmission schemes is a future direction that worth exploring.

In addition, our third work considers the same PCE ϵ for the initial transmission and retransmission. Retransmission power ramping can be adopted to provide

flexibility in the uplink power control. In particular, a device can either increase or decrease ϵ upon a transmission failure. It is interesting to derive the analytical expressions of coverage probability with power ramping and optimize the PCEs for the initial transmission and retransmissions.

Bibliography

- [1] M. Agiwal, A. Roy and N. Saxena, "Next generation 5G wireless networks: A comprehensive survey," *IEEE Communications Surveys & Tutorials*, vol. 18, no. 3, pp. 1617 - 1655, Third Quarter 2016.
- [2] I. U. Din, M. Guizani, S. Hassan, B. S. Kim, M. K. Khan, M. Atiquzzaman, and S. H. Ahmed, "The Internet of things: A review of enabled technologies and future challenges," *IEEE Access*, vol. 7, pp. 7606 - 7640, Dec. 2018.
- [3] J. Pan, and J. McElhannon, "Future edge cloud and edge computing for Internet of things applications," *IEEE Internet of Things Journal*, vol. 5, no. 1, pp. 439 - 449, Feb. 2018.
- [4] X. Chen, Q. Shi, L. Yang, and J. Xu, "Thrifty edge: Resource-efficient edge computing for intelligent IoT applications," *IEEE Network*, vol. 32, no. 1, pp. 61 - 65, Feb. 2018.
- [5] D. You, B. S. Seo, E. Jeong, and D. H. Kim, "Internet of things (IoT) for seamless virtual reality space: Challenges and perspectives," *IEEE Access*, vol. 6, pp. 40439 - 40449, April 2018.
- [6] M. Conoscenti, A. Vetrò, and J. C. D. Martin, "Blockchain for the Internet of things: A systematic literature review," in *Proc. of IEEE/ACS 13th International Conference of Computer Systems and Applications (AICCSA)*, Dec. 2016.
- [7] V. Hassija, V. Chamola, V. Saxena, D. Jain, P. Goyal, and B. Sikdar, "A survey on IoT security: Application areas, security threats, and solution architectures," *IEEE Access*, vol. 7, pp. 82721 - 82743, June 2019.
- [8] A Zanella, N. Bui, A. Castellani, L. Vangelista, and M. Zorzi, "Internet of things for smart cities," *IEEE Internet of Things Journal*, vol. 1, no. 1, pp. 22 - 32, Feb. 2014.
- [9] S. Nalbandian, "A survey on Internet of things: Applications and challenges," in *Proc. of International Congress on Technology, Communication and Knowledge (ICTCK)*, Mashhad, Iran, Nov. 2015.
- [10] Y. Shaikh, V. K. Parvati, S. R. Biradar, "Survey of smart healthcare systems using Internet of things (IoT)," in *Proc. of International Conference on Communication, Computing and Internet of Things*, Chennai, India, Feb. 2018.

- [11] S. Bera, S. Misra, and A. V. Vasilakos, “Software-defined networking for Internet of Things: A survey”, *IEEE Internet of Things Journal*, vol. 4, no. 6, Dec. 2017.
- [12] M. Elsaadany, A. Ali, and W. Hamouda, “Cellular LTE-A technologies for the future Internet-of-Things: Physical layer features and challenges,” *IEEE Communications Surveys & Tutorials*, vol. 19, no. 4, FOURTH QUARTER 2017.
- [13] H. Wang, and A. O. Fapojuwo, “A survey of enabling technologies of low power and long range machine-to-machine communications,” *IEEE Communications Surveys & Tutorials*, vol. 19, no. 4, Fourth Quarter 2017.
- [14] C. Anton-Haro and M. Dohler, Machine-to-Machine (M2M) communications: Architectures, performance and applications. Cambridge, U.K.: Woodhead, 2015.
- [15] Mobile and wireless communications enablers for the twenty-twenty information society (METIS), “Final Project Report,” document number ICT-317669-METIS/D8.4, April 2015.
- [16] A. Rico-Alvarino, *et al.*, “An overview of 3GPP enhancements on machine to machine communications,” *IEEE Commun. Mag.*, vol. 54, no. 6, pp. 14–21, Jun. 2016.
- [17] D. Flore, Evolution of LTE in Release 13. [Online]. Available: <http://www.3gpp.org/news-events/3gpp-news/1628-rel13>
- [18] Jeffrey Hill, “Kore Telematics Launches Iridium, Vodafone-Supported M2M Wireless Service”. Satellite Today.
- [19] 3rd Generation Partnership Project (3GPP), Technical Specification Group Radio Access Network, Study on Provision of Low-Cost Machine-Type Communications (MTC) User Equipments (UEs) Based on LTE, Release 12, June 2013.
- [20] 3rd Generation Partnership Project (3GPP), Technical Specification Group GSM/EDGE Radio Access Network, Cellular System Support for Ultra Low Complexity and Low Throughput Internet of Things, Release 13, June 2015.
- [21] S. Chen, R. Ma, H. H. Chen, H. Zhang, W. Meng, and J. Liu, “Machine-to-machine communications in ultra-dense networks—a survey,” *IEEE Communications Surveys & Tutorials*, vol. 19, no. 3, Third Quarter 2017.
- [22] S. K. Sharma, and X. Wang, “Towards massive machine type communications in ultra-dense cellular IoT networks: Current issues and machine learning-assisted solutions,” to appear in *IEEE Communications Surveys & Tutorials*.
- [23] A. N. Parks, A. Liu, S. Gollakota, and J. R. Smith, “Turbocharging ambient backscatter communication,” in *Proc. of the 2014 ACM conference on SIGCOMM*, Chicago, IL, Aug. 2014.
- [24] D. Bharadia, *et al.*, “BackFi: High throughput WiFi backscatter,” in *Proc. of ACM SIGCOMM*, London, United Kingdom, Aug. 2015.

- [25] S. Bi, Y. Zeng, R. Zhang, “Wireless powered communication networks: An overview,” *IEEE Wireless Communications*, vol. 23, no. 2, pp. 10-18, Apr. 2016.
- [26] V. Liu, A. Parks, V. Talla, S. Gollakota, D. Wetherall, and J. R. Smith, “Ambient backscatter: Wireless communication out of thin air,” in *Proc. of the 2013 ACM conference on SIGCOMM*, Hong Kong, China, August 2013.
- [27] Z. Zheng, L. Song, D. Niyato, and Z. Han, “Resource allocation in wireless powered relay networks: A bargaining game approach,” vol. 66, no. 7, pp. 6310-6323, July 2017.
- [28] Z. Chen, L. X. Cai, Y. Cheng, and H. Shan, “Sustainable cooperative communication in wireless powered networks with energy harvesting relay,” *IEEE Transactions on Wireless Communications*, vol. 16, no. 12, pp. 8175-8189, Dec. 2017.
- [29] X. Lu, P. Wang, D. Niyato, D. I. Kim, and Z. Han, “Wireless charger networking for mobile devices: Fundamentals, standards, and applications,” *IEEE Wireless Communications*, vol. 22, no. 2, pp. 126-135, April 2015.
- [30] A. A. Nasir, X. Zhou, S. Durrani, and R. A. Kennedy, “Wireless-powered relays in cooperative communications: Time-switching relaying protocols and throughput analysis,” *IEEE Transactions on Communications*, vol. 63, no. 5, pp. 1607-1622, May 2015.
- [31] H. Chen, Y. Li, J. L. Rebelatto, B. F. Uchôa-Filho, and B. Vucetic, “Harvest-then-cooperate: Wireless-powered cooperative communications,” *IEEE Transactions on Signal Processing*, vol. 63, no. 7, pp. 1700-1711, Apr. 2015.
- [32] N. V. Huynh, D. T. Hoang, X. Lu, D. Niyato, P. Wang, and D. I. Kim, “Ambient backscatter communications: A contemporary survey,” *IEEE Communications Surveys & Tutorials*, vol. 20, no. 4, pp. 2889-2922, Fourth Quarter 2018.
- [33] Z. Ma, C. He, Y. Rao, J. Jiang, S. Ma, F. Gao, and L. Xing, “Time- and power-splitting strategies for ambient backscatter system,” *IEEE Access*, vol. 7, pp. 40068-40077, pp. 40068 -40077. Mar. 2019.
- [34] D. Li, W. Peng, and Y. Liang, “Hybrid ambient backscatter communication systems with harvest-then-transmit protocols,” *IEEE Access*, vol. 6, pp. 45288-45298, Aug. 2018.
- [35] G. Yang, D. Yuan, Y. Liang, R. Zhang, and V. C. M. Leung, “Optimal Resource allocation in full-duplex ambient backscatter communication networks for wireless-powered IoT,” *IEEE Internet of Things Journal*, vol. 6, no. 2, pp. 2612 - 2625, Apr. 2019.
- [36] S. Xiao, H. Guo, and Y. Liang, “Resource allocation for full-duplex-enabled cognitive backscatter networks,” *IEEE Transactions on Wireless Communications*, vol. 18, no. 6, pp. 3222 - 3235, Jun. 2019.

- [37] H. Nishiyama, M. Ito, and N. Kato, "Relay-by-smartphone: Realizing multihop device-to-device communications," *IEEE Commun. Mag.*, vol. 52, no. 4, pp. 56-65, Apr. 2014.
- [38] Y. Zeng and R. Zhang, "Full-duplex wireless-powered relay with self-energy recycling," *IEEE Wireless Communications Letters*, vol. 4, no. 2, pp. 201-204, Apr. 2015.
- [39] X. Lu, P. Wang, D. Niyato, and E. Hossain, "Dynamic spectrum access in cognitive radio networks with RF energy harvesting," *IEEE Wireless Communications*, vol. 21, no. 3, pp. 102-110, June 2014.
- [40] L. Tang, X. Zhang, P. Zhu, and X. Wang "Wireless information and energy transfer in fading relay channels," *IEEE Journal on Selected Areas in Communications*, vol. 34, no. 12, pp. 3632-3645, Dec. 2016.
- [41] B. Lyu, Z. Yang, H. Guo, F. Tian, and G. Gui, "Relay cooperation enhanced backscatter communication for Internet-of-things," *IEEE Internet of Things Journal*, vol. 6, no. 2, pp. 2860 - 2871, April 2019.
- [42] S. Gong, X. Huang, J. Xu, W. Liu, P. Wang, and D. Niyato, "Backscatter relay communications powered by wireless energy beamforming," *IEEE Transactions on Communications*, vol. 66, no. 7, pp. 3187 - 3200, June 2018.
- [43] 3GPP, Evolved Universal Terrestrial Radio Access (E-UTRA): Physical Layer Procedures, document TS 36.213, 3rd Generation Partnership Project (3GPP), Sep. 2010.
- [44] R. Müllner, C. F. Ball, K. Ivanov, J. Lienhart, and P. Hric, "Contrasting open-loop and closed-loop power control performance in UTRAN LTE uplink by UE trace analysis," in *Proc. of IEEE International Conference on Communications*, Dresden, Germany, Jun. 2009.
- [45] P. Baracca, Lorenzo Galati Giordano, Adrian Garcia-Rodriguez, Giovanni Geraci, and David López-Pérez, "Downlink performance of uplink fractional power control in 5G massive MIMO systems," in *Proc. of IEEE Global Communications Conference Workshops*, Abu Dhabi, UAE, Dec. 2018.
- [46] G. Nigam, P. Minero, and M. Haenggi, "Spatiotemporal cooperation in heterogeneous cellular networks," *IEEE J. Sel. Areas Commun.*, vol. 33, no. 6, pp. 1253-1265, Jun. 2015.
- [47] X. Lu, H. Jiang, D. Niyato, D. I. Kim and Z. Han, "Wireless-powered device-to-device communications with ambient backscattering: Performance modeling and analysis," *IEEE Transactions on Wireless Communications*, vol. 17, no. 3, pp. 1528-1544, March 2018.
- [48] X. Lu, H. Jiang, D. Niyato, D. I. Kim, and P. Wang, "Analysis of wireless-powered device-to-device communications with ambient backscattering" in *Proc. of IEEE VTC 2017-Fall*, Toronto, Canada, Sept. 2017.

- [49] H. ElSawy, A. Sultan-Salem, M. S. Alouini, *et al.*, “Modeling and analysis of cellular networks using stochastic geometry: A tutorial,” *IEEE Communications Surveys & Tutorials*, vol. 19, no. 1, pp. 167-203, First Quarter 2017
- [50] H. ElSawy, E. Hossain, and M. Haenggi, “Stochastic geometry for modeling, analysis, and design of multi-tier and cognitive cellular wireless networks: A survey,” *IEEE Communications Surveys & Tutorials*, vol. 15, no. 3, pp. 996-1019, Third Quarter 2013.
- [51] M. Haenggi, J. G. Andrews, F. Baccelli, O. Dousse, and M. Franceschetti, “Stochastic geometry and random graphs for the analysis and design of wireless networks,” vol. 27, no. 7, pp. 1029 - 1046, Sep. 2009.
- [52] J. G. Andrews, F. Baccelli, and R. K. Ganti, “A tractable approach to coverage and rate in cellular networks,” *IEEE Transactions on Communications*, vol. 59, no. 11, pp. 3122-3134, Nov. 2011.
- [53] S. Cho, and W. Choi, “Energy-efficient repulsive cell activation for heterogeneous cellular networks,” *IEEE Journal on Selected Areas in Communications*, vol. 31, no. 5, pp. 870-882, May 2013.
- [54] M. Kountouris, and N. Pappas, “Approximating the interference distribution in large wireless networks,” in *Proc. of International Symposium on Wireless Communications Systems (ISWCS)*, Barcelona, Spain, Aug. 2014.
- [55] T.-Y. Lin, H. Santoso, and K.-R. Wu, “Global sensor deployment and local coverage-aware recovery schemes for smart environments,” *IEEE Trans. Mobile Comput.*, vol. 14, pp. 1382–1396, Jul. 2015.
- [56] L. Decreusefond, I. Flint, and A. Vergne, “A note on the simulation of the Ginibre point process,” *J. Appl. Probab.*, vol. 52, no. 4, pp. 1003-1012, Dec. 2015.
- [57] T. Shirai and Y. Takahashi, “Random point fields associated with certain Fredholm determinants I: Fermion, Poisson and Boson point processes,” *Journal of Functional Analysis*, vol. 205, no. 2, pp. 414-463, Dec. 2003.
- [58] F. Bornemann, “On the numerical evaluation of fredholm determinants,” *Mathematics of Computation*, vol. 79, No. 270, pp. 871-915. Apr. 2010.
- [59] H.-B. Kong, I. Flint, P. Wang, D. Niyato, and N. Privault, “Exact performance analysis of ambient RF energy harvesting wireless sensor networks with Ginibre point process,” *IEEE Journal on Selected Areas in Communications*, vol. 34, no. 12, pp. 3769-3784, Dec. 2016.
- [60] X. Lu, P. Wang, D. Niyato, D. I. Kim, and Z. Han, “Wireless networks with RF energy harvesting: A contemporary survey,” *IEEE Commun. Surveys Tuts.*, vol. 17, no. 2, pp. 757–789, Second Quarter, 2015.
- [61] S. D. Assimonis, S.N. Daskalakis, and A. Bletsas, “Sensitive and efficient RF harvesting supply for batteryless backscatter sensor networks,” *IEEE Transactions on Microwave Theory and Techniques*, vol. 64, no. 4, pp. 1327-1338, Mar. 2016.

- [62] Z. Shen, A. Athalye, and P. Djuric, "Phase cancellation in backscatter-based tag-to-tag communication systems," *IEEE Internet of Things Journal*, vol. 3, no. 6, Dec. 2016.
- [63] R. Correia, and N. B. Carvalho, "Design of high order modulation backscatter wireless sensor for passive IoT solutions," in *Proc. of IEEE Wireless Power Transfer Conference (WPTC)*, Aveiro, Portugal, Jun. 2016.
- [64] D. Dardari, R. D'Errico, C. Roblin, A. Sibille, and Moe Z. Win, "Ultrawide bandwidth RFID: The next generation?," *Proc. of the IEEE*, vol. 98, no. 9, pp. 1570-1582, Jul. 2010.
- [65] J. C. Ikuno, M. Wrulich, and M. Rupp, "Performance and modeling of LTE H-ARQ," in *Proc. of International ITG Workshop on Smart Antennas, WSA*, February 2009.
- [66] A. H. Sakr, and E. Hossain, "Cognitive and energy harvesting-based D2D communication in cellular networks: stochastic geometry modeling and analysis," *IEEE Transactions on Communications*, vol. 63, no. 5, pp. 1867-1880, May 2015.
- [67] H. H. Yang, J. Lee, and T. Q. Quek, "Heterogeneous cellular network with energy harvesting-based D2D communication," *IEEE Transactions on Wireless Communications*, vol. 15, no. 2, pp. 1406-1419, Oct. 2016.
- [68] D. Darsena, G. Gelli, and F. Verde, "Modeling and performance analysis of wireless networks with ambient backscatter devices," *IEEE Transactions on Communications*, vol. 65, no. 4, pp. 1797-1814, Jan. 2017.
- [69] Y. Liu, L. Wang, S. A. R. Zaidi, M. Elkashlan, and T. Q. Duong, "Secure D2D communication in large-scale cognitive cellular networks: A wireless power transfer model," *IEEE Transactions on Communications*, vol. 64, no. 1, pp. 329-342, Nov. 2016.
- [70] K. Han and K. Huang, "Wirelessly powered backscatter communication networks: modeling, coverage and capacity," vol. 16, no. 4, pp. 2548-2561, Apr. 2017.
- [71] D. T. Hoang, D. Niyato, P. Wang, and D. I. Kim, "Optimal time sharing in RF-powered backscatter cognitive radio networks," in *Proc. of IEEE ICC*, Paris, France, May 2017.
- [72] S. H. Kim and D. I. Kim, "Hybrid backscatter communication for wireless-powered heterogeneous networks," vol. 16, no. 10, pp. 6557-6570, *IEEE Transactions on Wireless Communications*, Oct. 2017.
- [73] D. Camps-Mur, A. Garcia-Saavedra, and P. Serrano, "Device-to-device communications with WiFi direct: Overview and experimentation," *IEEE Wireless Communications*, vol. 20, no. 3, pp. 96-104, Jul. 2013.

- [74] X. Lin, J. Andrews, A. Ghosh, and R. Ratasuk, "An overview of 3GPP device-to-device proximity services," *IEEE Communications Magazine*, vol. 52, no. 4, pp. 40-48, Apr. 2014.
- [75] C. Boyer and S. Roy, "Backscatter communication and RFID: Coding, energy, and MIMO Analysis," *IEEE Transactions on Communications*, vol. 62, no. 3, pp. 770-785, Mar. 2014.
- [76] C. Boyer and S. Roy, "Coded QAM backscatter modulation for RFID," *IEEE Transactions on Communications*, vol. 60, pp. 1925-1934, Jul. 2012.
- [77] Y. Ishikawa, S. Lee, S. Yonezawa, S. Ikeda, Y. Fang, T. Hamada, H. Ito, N. Ishihara, and K. Masu "A 0.5-V 1.56-mW 5.5-GHz RF transceiver IC module with J-shaped folded monopole antenna," in *Proc. of IEEE International Symposium on Circuits and Systems (ISCAS)*, Lisbon, Portugal, May 2015.
- [78] X. Lu, P. Wang, D. Niyato, and E. Hossain, "Dynamic spectrum access in cognitive radio networks with RF energy harvesting," *IEEE Wireless Communications*, vol. 21, no. 3, pp. 102-110, June 2014.
- [79] P. V. Nikitin and K. Rao, "Theory and measurement of backscattering from RFID tags," *IEEE Antennas Propagat. Mag.*, vol. 48, no. 6, Dec. 2006.
- [80] N. Miyoshi and T. Shirai, "Downlink coverage probability in a cellular network with ginibre deployed base stations and Nakagami-m fading channels," in *Proc. of International Symposium on Modeling and Optimization in Mobile, Ad Hoc, and Wireless Networks (WiOpt)*, pp. 483-489, Mumbai, India, May 2015.
- [81] I. Flint, X. Lu, N. Privault, D. Niyato, and P. Wang, "Performance analysis of ambient RF energy harvesting with repulsive point process modelling," *IEEE Transactions on Wireless Communications*, vol. 14, no. 10, pp. 5402-5416, May 2015.
- [82] X. Lu, H. Jiang, D. Niyato, D. I. Kim, and P. Wang, "Analysis of wireless-powered device-to-device communications with ambient backscattering" in *Proc. of IEEE VTC 2017-Fall*, Sept. 2017.
- [83] X. Lu, I. Flint, D. Niyato, N. Privault, and P. Wang, "Performance analysis for simultaneously wireless information and power transfer with ambient RF energy harvesting," in *Proc. of IEEE WCNC*, New Orleans, LA, USA, March 2015.
- [84] I. Flint, X. Lu, N. Privault, D. Niyato, and P. Wang, "Performance analysis of ambient RF energy harvesting: A stochastic geometry approach," in *Proc. of IEEE Globecom*, Austin, USA, December 2014.
- [85] N. Deng, W. Zhou, and M. Haenggi, "The ginibre point process as a model for wireless networks with repulsion," *IEEE Transactions on Wireless Communications*, vol. 14, pp. 107-121, Jan. 2015.

- [86] A. Shirane, Y. Fang, H. Tan, T. Ibe, H. Ito, N. Ishihara, and K. Masu, "RF-powered transceiver with an energy- and spectral-efficient IF-based quadrature backscattering transmitter," *IEEE Journal of Solid-State Circuits*, vol. 50, no. 12, pp. 2975-2987, August 2015.
- [87] V. Gazis, "A survey of standards for machine-to-machine (M2M) and the Internet of things (IoT)," *IEEE Communications Surveys & Tutorials*, vol. 19, no. 1, First Quarter 2017.
- [88] D. T. Hoang, D. Niyato, P. Wang, D. I. Kim, and Z. Han, "Ambient backscatter: A new approach to improve network performance for RF-powered cognitive radio networks," *IEEE Transactions on Communications*, vol. 65, no. 9, pp. 3659-3674, Sept. 2017.
- [89] R. B. Ash, *Basic probability theory*, Dover, 2008.
- [90] P. Flajolet, X. Gourdon, and P. Dumas, "Mellin transforms and asymptotics: Harmonic sums," *Theoretical Computer Science*, vol. 144, no. 1-2, pp. 3-58, Jun. 1995.
- [91] A. M. Cohen, *Numerical methods for Laplace transform inversion*. New York, NY, USA: Springer-Verlag, Jun. 2007.
- [92] M. Abramowitz and I. A. Stegun, *Handbook of mathematical functions: with formulas, graphs, and mathematical tables*. Dover Publications, INC., New York, 1964.
- [93] X. Lu, D. Niyato, H. Jiang, E. Hossain, and P. Wang, "Ambient backscatter-assisted wireless-powered relaying," *IEEE Transactions on Green Communications and Networking*, vol. 3, No. 4, pp. 1087-1105, Dec. 2019.
- [94] X. Lu, G. Li, H. Jiang, D. Niyato, and P. Wang, "Analysis of wireless-powered relaying with ambient backscattering," in *Proc. of IEEE ICC*, Kansas city, MO, May 2018.
- [95] B. Lyu, H. Guo, Z. Yang, and G. Gui, "Throughput maximization for hybrid backscatter assisted cognitive wireless powered radio networks," *IEEE Internet of Things Journal*, vol. 5, no. 3, pp. 2015-2024, Jun. 2018.
- [96] L. Xu, K. Zhu, R. Wang, and S. Gong, "Performance analysis of RF-powered cognitive radio networks with integrated ambient backscatter communications," *Wireless Communications and Mobile Computing*, Apr. 2018.
- [97] I. Krikidis, "Relay selection in wireless powered cooperative networks with energy storage," *IEEE Journal on Selected Areas in Communications*, vol. 33, no. 12, pp. 2596-2610, Dec. 2015.
- [98] Y. Huang, and B. Clerckx, "Relaying strategies for wireless-powered MIMO relay networks," *IEEE Transactions on Wireless Communications*, vol. 15, no. 9, pp. 6033-6047, Sept. 2016.

- [99] A. A. Nasir, X. Zhou, S. Durrani, and R. A. Kennedy, "Relaying protocols for wireless energy harvesting and information processing," *IEEE Trans. Wireless Commun.*, vol. 12, no. 7, pp. 3622-3636, Jul. 2013.
- [100] Y. Gu, and S. Aïssa, "RF-based energy harvesting in decode-and-forward relaying systems: Ergodic and outage capacities," *IEEE Transactions on Wireless Communications*, vol. 14, no. 11, pp. 6425-6434, Nov. 2015.
- [101] R. Rajesh, V. Sharma, and P. Viswanath, "Capacity of Gaussian channels with energy harvesting and processing cost," *IEEE Transactions on Information Theory*, vol. 60, no. 5, pp. 2563-2575, May 2014.
- [102] L. Decreusefond *et al.*, "Determinantal point processes," in *Stochastic Analysis for Poisson Point Processes*, Springer, pp. 311-342, Jun. 2016.
- [103] X. Li, Y. Wu, and E. Serpedin, "Timing synchronization in decode-and-forward cooperative communication systems," *IEEE Transactions on Signal Processing*, vol. 57, no. 4, pp. 1444-1455, April 2009.
- [104] Y. Yao, and X. Dong, "Low-complexity timing synchronization for decode-and-forward cooperative communication systems with multiple relays," *IEEE Transactions on Vehicular Technology*, vol. 62, no. 6, pp. 2865-2871, July 2013.
- [105] M. Z. Win, P. C. Pinto, and L. A. Shepp, "A mathematical theory of network interference and its applications," *Proc. of the IEEE*, vol. 97, no. 2, pp. 205-230, Feb. 2009.
- [106] Y. Gu, and S. Aïssa, "RF-based energy harvesting in decode-and-forward relaying systems: Ergodic and outage capacities," *IEEE Transactions on Wireless Communications*, vol. 14, no. 11, pp. 6425-6434, Nov. 2015.
- [107] D.-Y. Kim, H.-G. Yoon, B.-J. Jang, and J.-G. Yook, "Effects of reader-to-reader interference on the UHF RFID interrogation range," *IEEE Transactions on Industrial Electronics*, vol. 56, no. 7, pp. 2337-2346, Jul. 2009.
- [108] P. Zhang, *et al.*, "Enabling practical backscatter communication for on-body sensors," in *Proc. of the ACM SIGCOMM*, August 2016.
- [109] M. Kotaru, P. Zhang, and S. Katti, "Localizing low-power backscatter tags using commodity WiFi," in *Proc. of the 13th International Conference on emerging Networking EXperiments and Technologies*, Incheon, South Korea, Dec. 2017.
- [110] J. K. Devineni and H. S. Dhillon, "Ambient backscatter systems: Exact average bit error rate under fading channels," *IEEE Transactions on Green Communications and Networking*, vol. 3, no. 1, pp. 11 - 25, March 2019.
- [111] J. Kimionis, A. Bletsas, and J. N. Sahalos, "Bistatic backscatter radio for tag read-range extension," in *Proc. of IEEE International Conference on RFID-Technologies and Applications (RFID-TA)*, Nice, France, Nov. 2012.

- [112] X. Lu, H. Jiang, D. Niyato, D. I. Kim and Z. Han, "Wireless-powered device-to-device communications with ambient backscattering: Performance modeling and analysis," *IEEE Transactions on Wireless Communications*, vol. 17, no. 3, pp. 1528-1544, Mar. 2018.
- [113] E. Kofidis, *et al.*, "Preamble-based channel estimation in OFDM/OQAM systems: A review," *Signal Processing*, vol. 93, no. 7, July 2013.
- [114] A. Crismani, S. Toumpis, U. Schilcher, G. Brandner, and C. Bettstetter, "Cooperative relaying under spatially and temporally correlated interference," *IEEE Trans. Veh. Technol.*, vol. 64, no. 10, pp. 4655-4669, Oct. 2015.
- [115] X. Lu, I. Flint, D. Niyato, N. Privault, and P. Wang, "Self-sustainable communications with RF energy harvesting: Ginibre point process modeling and analysis," *Journal on Selected Areas in Communications*, vol. 34, no. 5, pp. 1518-1535, May 2016.
- [116] H.-B. Kong, *et al* "Exact performance analysis of ambient RF energy harvesting wireless sensor networks with Ginibre point process," *IEEE Journal on Selected Areas in Communications*, vol. 34, no. 12, pp. 3769-3784, Dec. 2016.
- [117] M. Abramowitz and I. A. Stegun, *Handbook of mathematical functions with formulas, graphs, mathematical tables*, 9th ed. New York, NY, USA: Dover, 1972.
- [118] B. Kellogg, A. Parks, S. Gollakota, J. R. Smith, and D. Wetherall, "WiFi backscatter: Internet connectivity for RF-powered devices," *ACM SIGCOMM Computer Communication Review*, vol. 44, no. 4, pp. 607-618, August 2014.
- [119] C. Gomez, and J. Paradells, "Wireless home automation networks: A survey of architectures and technologies," *IEEE Communications Magazine*, vol. 48, no. 6, pp. 92-101, June 2010.
- [120] X. Lu, E. Hossain, H. Jiang, and G. Li, "On coverage probability with type-II HARQ in large-scale uplink cellular networks," *IEEE Wireless Communications Letter*, vol. 9, no. 1, Jan. 2020.
- [121] M. Haenggi and R. Smarandache, "Diversity polynomials for the analysis of temporal correlations in wireless networks," *IEEE Trans. Wireless Commun.*, vol. 12, no. 11, pp. 5940-5951, Nov. 2013.
- [122] L. H. Afify, H. ElSawy, T. Y. Al-Naffouri, and M. S. Alouini, "A unified stochastic geometry model for MIMO cellular networks with retransmissions," *IEEE Trans. Wireless Commun.*, vol. 15, no. 12, pp. 8595-8609, Dec. 2016.
- [123] M. Sheng, J. Wen, J. Li, B. Liang, and X. Wang, "Performance analysis of heterogeneous cellular networks with HARQ under correlated interference," *IEEE Trans. Wireless Commun.*, vol. 16, no. 12, pp. 8377-8389, Dec. 2017.
- [124] J. Wen, M. Sheng, K. Huang, and J. Li, "Effects of base-station spatial interdependence on interference correlation and network performance," *IEEE Trans. Commun.*, vol. 66, no. 7, pp. 3092-3107, Jul. 2018.

- [125] M. Haenggi, *Stochastic Geometry for Wireless Networks*. Cambridge, U.K.: Cambridge Univ. Press, 2013.
- [126] R. Arshad, L. H. Afify, H. ElSawy, T. Y. Naffouri, and M. S. Alouini, "On the effect of uplink power control on temporal retransmission diversity," *IEEE Wireless Commun. Lett.*, vol. 8, no. 1, pp. 309-312, Feb. 2019.
- [127] M. Haenggi, "User point processes in cellular networks," *IEEE Wireless Commun. Lett.*, vol. 6, no. 2, pp. 258-261, Apr. 2017.
- [128] M. Di Renzo and P. Guan, "Stochastic geometry modeling and system-level analysis of uplink heterogeneous cellular networks with multi-antenna base stations," *IEEE Trans. Commun.*, no. 64, vol. 6, pp. 2453-2476, Jun. 2016.
- [129] Y. Wang, M. Haenggi, and Z. Tan, "The meta distribution of the SIR for cellular networks with power control," *IEEE Trans. Commun.*, vol. 66, no. 4, pp. 1745-1757, Apr. 2018.
- [130] H. ElSawy and E. Hossain, "On stochastic geometry modeling of cellular uplink transmission with truncated channel inversion power control," *IEEE Trans. Wireless Commun.*, vol. 13, no. 8, pp. 4454-4469, Aug. 2014.
- [131] A. H. Sakr, and E. Hossain, "Analysis of K-tier uplink cellular networks with ambient RF energy harvesting," *IEEE Journal on Selected Areas in Communications*, vol. 33, no. 10, pp. 2226-2238, Oct. 2015.
- [132] S. M. R. Islam, N. Avazov, O. A. Dobre, and K. S. Kwak, "Power-domain non-orthogonal multiple access (NOMA) in 5G systems: Potentials and challenges," *IEEE Communications Surveys & Tutorials*, vol. 19, no. 2, Second Quarter 2017.
- [133] R. Abbas, M. Shirvanimoghaddam, Y. Li, and B. Vucetic, "A novel analytical framework for massive grant-free NOMA," *IEEE Transactions on Communications*, vol. 67, no. 3, pp. 2436 - 2449, March 2019.
- [134] P. Hu, P. Zhang, M. Rostami, and D. Ganesan, "Braidio: An integrated active-passive radio for mobile devices with asymmetric energy budgets," in *Proc. of ACM SIGCOMM*, Florianopolis, Brazil, Aug. 2016.
- [135] X. Lu, D. Niyato, H. Jiang, D. I. Kim, Y. Xiao and Z. Han, "Ambient backscatter assisted wireless powered communications," *IEEE Wireless Communications*, vol. 25, no. 2, pp. 170-177, Apr. 2018.
- [136] D. Niyato, X. Lu, P. Wang, D. I. Kim and Z. Han, "Economics of Internet of things (IoT): An information market approach," *IEEE Wireless Communications*, vol. 23, no. 4, pp. 136-145, August 2016.
- [137] D. Niyato, X. Lu, and P. Wang, "Machine-to-machine communications for home energy management system in smart grid," *IEEE Communications*, vol. 49, no. 4, pp. 53-59, April 2011.

- [138] D. Niyato, X. Lu, P. Wang, D. I. Kim and Z. Han “Distributed wireless energy scheduling for wireless powered sensor networks,” in *Proc. of IEEE ICC*, Kuala Lumpur, Malaysia, 23-27, May 2016.
- [139] J. Liu, N. Kato, J. Ma, and N. Kadowaki, “Device-to-device communication in LTE-advanced networks: A survey,” *IEEE Communications Surveys & Tutorials*, vol. 17, no. 4, 1923-1940, Dec. 2015.
- [140] X. Lu, P. Wang, and D. Niyato, “Hierarchical cooperation for operator-controlled device-to-device communications: A layered coalitional game approach,” in *Proc. of IEEE WCNC*, New Orleans, LA, USA, March 2015.
- [141] D. Niyato, P. Wang, D. I. Kim, Z. Han, and X. Lu, “Game theoretic modeling of jamming attack in wireless powered networks,” in *Proc. of IEEE ICC*, London, UK, June 2015.
- [142] D. Niyato, X. Lu, P. Wang, D. I. Kim and Z. Han, “Performance analysis of delay-constrained wireless energy harvesting communication networks under jamming attacks,” in *Proc. of IEEE WCNC*, New Orleans, LA, USA, March 2015.
- [143] G. Wang, F. Gao, R. Fan, and C. Tellambura, “Ambient backscatter communication systems: Detection and performance analysis,” *IEEE Transactions on Communications*, vol. 64, no. 11, pp. 4836-4846, Aug. 2016.
- [144] K. Huang and V. K. N. Lau, “Enabling wireless power transfer in cellular networks: Architecture, modeling and deployment,” *IEEE Transactions on Wireless Communications*, vol. 13, no. 2, pp. 902-912, Feb. 2014.
- [145] B. Kellogg, A. Parks, S. Gollakota, J. R. Smith, and D. Wetherall, “Wi-Fi backscatter: Internet connectivity for RF-powered devices,” in *Proc. of the 2014 ACM conference on SIGCOMM*, Chicago, IL, Aug. 2014.
- [146] J. Kimionis, A. Bletsas, and J. N. Sahalos, “Increased range bistatic scatter radio,” *IEEE Trans. Commun.*, vol. 62, pp. 1091-1104, Mar. 2014.
- [147] S. Bi, C. K. Ho, and R. Zhang, “Wireless powered communication: Opportunities and challenges,” *IEEE Communications Magazine*, vol. 53, no. 4, pp. 117-125, Apr. 2015.
- [148] R. Correia and N. B. Carvalho, “Design of high order modulation backscatter wireless sensor for passive IoT solutions,” in *Proc. of IEEE Wireless Power Transfer Conference (WPTC)*, Aveiro, Portugal, Jun. 2016.
- [149] D. Dardari, R. D’Errico, C. Roblin, A. Sibille, and M. Z. Win, “Ultrawide bandwidth RFID: The next generation?,” *Proc. of the IEEE*, vol. 98, no. 9, pp. 1570-1582, Jul. 2010.
- [150] X. Lu, D. Niyato, H. Jiang, D. I. Kim, Y. Xiao, and Z. Han, “Ambient backscatter assisted wireless powered communications,” vol. 25, no. 2, pp. 170 - 177, *IEEE Wireless Communications*, April 2018.

- [151] Z. Dawy, W. Saad, A. Ghosh, J. G. Andrew, and E. Yaacoub, "Toward massive machine type cellular communications," *IEEE Wireless Communications*, vol. 24, no. 1, pp. 120 - 128, Feb. 2017.
- [152] X. Lu, G. Li, H. Jiang, D. Niyato, and P. Wang, "Performance analysis of wireless-powered relaying with ambient backscattering," in *Proc. of IEEE ICC*, Kansas City, MO, USA, May 2018.
- [153] H. Lee, K.-J. Lee, H. Kim, B. Clerckx, and I. Lee, "Resource allocation techniques for wireless powered communication networks with capacitor constraint," *IEEE Transactions on Wireless Communications*, vol. 15, no. 4, pp. 2619-2628, Apr. 2016.
- [154] Q. Wu, W. Chen, Derrick Wing Kwan Ng, and R. Schober, "User-centric energy efficiency maximization for wireless powered communications," *IEEE Trans. Wireless Commun.*, vol. 15, no. 10, pp. 6898-6912, Jul. 2016.
- [155] E. Boshkovska, *et al.*, "Robust resource allocation for MIMO wireless powered communication networks based on a non-linear EH model," *IEEE Transactions on Communications*, vol. 65, no. 5, pp. 1984-1999, May 2017.
- [156] X. Lu, P. Wang, D. Niyato, D. I. Kim and Z. Han, "Wireless charging technologies: Fundamentals, standards, and network applications," *IEEE Communications Surveys and Tutorials*, vol. 18, no. 2, pp. 1413-1452, Second Quarter, 2016.
- [157] P. Hu, P. Zhang, M. Rostami, and D. Ganesan, "Braidio: An integrated active-passive radio for mobile devices with asymmetric energy budgets," in *Proc. of ACM SIGCOMM*, Florianopolis, Brazil, Aug. 2016.
- [158] A. Salem, K. A. Hamdi, K. M. Rabie, "Physical layer security with RF energy harvesting in AF multi-antenna relaying networks," *IEEE Transactions on Communications*, vol. 64, no. 7, pp. 3025-3038, July 2016.
- [159] T. Weiss, P. Ferrari, H. Spohn, "Determinantal point processes." In: *Reflected Brownian Motions in the KPZ Universality Class*, SpringerBriefs in Mathematical Physics, vol. 18, Springer, Cham, Dec. 2016.
- [160] C. K. Ho, P. H. W. Fung, and S. Sun, "Carrier frequency offset estimation for two-way relaying: Optimal preamble and estimator design," *IEEE Transactions on Wireless Communications*, vol. 12, no. 4, pp. 1898-1909, April 2013.
- [161] S. Ma, *et al.*, "Blind channel estimation for ambient backscatter communication systems," *IEEE Communications Letters*, vol. 22, no. 6, pp. 1296 - 1299, June 2018.
- [162] B. Makki and T. Eriksson, "On the performance of MIMO-ARQ systems with channel state information at the receiver," *IEEE Transactions on Communications*, vol. 62, no. 5, pp. 1588 - 1603, May 2014.
- [163] G. Nigam, P. Minero, and M. Haenggi, "Coordinated multipoint joint transmission in heterogeneous networks," *IEEE Trans. Commun.*, vol. 62, no. 11, pp. 4134-4146, Nov. 2014.

- [164] X. Lu, P. Wang, D. Niyato, and Z. Han, "Resource allocation in wireless networks with RF energy harvesting and transfer," *IEEE Network*, vol. 29, no. 6, pp. 68-75, December 2015.
- [165] X. Lu, P. Wang, D. Niyato, and Z. Han, "Resource allocation in wireless networks with RF energy harvesting and transfer," *IEEE Network*, vol. 29, no. 6, pp. 68-75, Dec. 2015.
- [166] W. Y. Toh, Y. K. Tan, W. S. Koh, and L. Siek, "Autonomous wearable sensor nodes with flexible energy harvesting," *IEEE Sensors Journal*, vol. 14, no. 7, pp. 2299-2306, Jul. 2014.
- [167] A. Al-Fuqaha, M. Guizani, M. Mohammadi, M. Aledhari, and M. Ayyash, "Internet of things: A survey on enabling technologies, protocols, and applications," *IEEE Communications Surveys & Tutorials*, vol. 17, no. 4, pp. 2347-2376, Jun. 2015.
- [168] G. Wang, F. Gao, R. Fan, and C. Tellambura, "Ambient backscatter communication systems: Detection and performance analysis," *IEEE Transactions on Communications*, vol. 64, no. 11, pp. 4836-4846, Aug. 2016.